11-15-2019

Measurements of the 16C + 12C and 16C + 13C Fusion Cross Sections with Implications for Astrophysics

Ashley Ann Hood

MEASUREMENTS OF THE ^{16}C + ^{12}C AND ^{16}C + ^{13}C FUSION CROSS SECTIONS WITH IMPLICATIONS FOR ASTROPHYSICS

A Dissertation

Submitted to the Graduate Faculty of the
Louisiana State University and
Agricultural and Mechanical College
in partial fulfillment of the
requirements for the degree of
Doctor of Philosophy

in

The Department of Physics and Astronomy

by
Ashley Ann Hood
B. S., Carnegie Mellon University, 2014
December 2019

This work is dedicated to my parents Ann Disbrow and Paul Disbrow
and to my husband Donald Hood,
who have loved and supported me immeasurably through graduate school.

Acknowledgments

This work was supported by the U.S. Department of Energy Office of Science, Office of Nuclear Physics by Award DE-FG02-96ER40978 and by Contract Number DE-AC02-06CH11357. This research used resources of Argonne National Laboratory's ATLAS Facility, which is a DOE Office of Science User Facility.

"What do you have that you did not receive? And if you did receive it, why do you boast as though you did not?" 1 Corinthians 4:7b

First and foremost, all thanks belongs to God, who has given me everything I have. He has created the Universe and sparked in me the desire to study its amazing complexity and underlying order.

Jeff Blackmon and Catherine Deibel, thank you for your guidance through my graduate studies. It has been absolutely crucial to my professional development. Thank you for the opportunities that you have made for me to participate in a variety of experiments, to pursue my interests, and to travel. I appreciate that you both have always made time to teach me and make sure that I understand things, your patience makes you great mentors.

Daniel Santiago-Gonzalez, thank you for taking the time to mentor me and for your help making this experiment a success. Thank you to the ANL staff at the laboratories who made the experiments possible. Thank you to my friends and fellow students who sat shifts for my experiments. Thank you to my committee who have listened to my research and given me helpful feedback.

Donald Hood, thank you for your constant support and encouragement as we have walked through life as graduate students together. You have kept me grounded and kept me fed with absolutely delicious food. The most amazing thing is that you did that while working hard through graduate school yourself. You are very smart and hard working and I aspire to emulate those qualities myself.

Ann Disbrow and Paul Disbrow, thank you for always encouraging me to follow my dreams, and thank you for the sacrifices you've made to give me an excellent education. Your support is the reason I have made it to this point and I can't thank you enough.

Tim Disbrow, thank you for encouraging me to pursue my interest in space by buying me my first telescope and sending me to Space Camp. That camp experience is what really solidified for me that I wanted to do collaborative, interesting science.

Jane and Todd Keller, Nancy Kiley, Sheila Albright, and Grant Disbrow, thank you for your support, encouragement, and prayers.

Jill Hood, thank you for your support and love. You are both a personal and scientific role model to me.

Contents

Abstract

The fusion of neutron-rich nuclei is of interest to nuclear astrophysics and nuclear structure. X-ray superbursts are powered by runaway thermonuclear burning deep inside of a neutron star, where heating from the pycnonuclear fusion of neutron-rich isotopes is an important heat source. Experimental measurements of fusion cross sections of neutron-rich isotopes have provided insights regarding nucleon transfer and nuclear structure properties affecting fusion. Recently, the ^{15}C + ^{12}C total fusion cross section was measured using a ^{15}C beam produced by the in-flight beam production facility, which is part of the Argonne Tandem LINAC Accelerator System (ATLAS) at Argonne National Laboratory (ANL). As an extension of that study to more neutron-rich systems, the ^{16}C + ^{12}C and ^{16}C + ^{13}C total fusion cross sections were measured. This dissertation presents the first fusion cross section measurements made with a ^{16}C radioactive beam. The beam was produced using the newly upgraded RAdioactive Ion SeparatOR (RAISOR) facility at ANL. The total fusion cross sections were measured with ^{12}C and ^{13}C targets in the active target MUlti-Sampling Ionization Chamber (MUSIC) detector filled with natural methane gas and 99.9% enriched ^{13}C methane gas, respectively. This is the most neutron-rich carbon fusion system that has been studied experimentally to date. The ^{16}C + ^{12}C and ^{16}C + ^{13}C cross sections were measured for $E_{C.M.}$ = 8 - 22 MeV. The measured cross sections show good agreement with theoretical models developed using the barrier-penetration formalism with the São Paulo potential and theoretical models using the selective resonant tunneling model and a complex square-well nuclear potential. Despite the significantly larger RMS radius of ^{16}C, the ^{16}C + ^{12,13}C cross sections are measured to be smaller than the ^{15}C + ^{12}C cross section. This indicates that an enhanced s-wave ^{15}C wave function might be increasing the ^{15}C fusion cross section or that neutron pairing effects in ^{16}C may reduce the ^{16}C cross sections.

Chapter 1. Introduction

A beautiful relationship exists between astronomical observations and measurements that can be made in the laboratory. There are few physical quantities that can be observed from astronomical objects, limited mainly to photons of different wavelengths, and in less common cases, neutrinos, cosmic rays, presolar grains, and gravitational waves. To understand how the internal workings of stars give rise to observations requires astrophysical models based on the knowledge of physics gained here on Earth. The scientists who study nuclear astrophysics strive to make these connections using combinations of experiment, theory, and computational models. The publication of the famous paper titled "Synthesis of the Elements in Stars" by Burbidge, Burbidge, Fowler, and Hoyle (commonly referred to as B^2FH) drew important connections between the then current knowledge of nuclear physics, the abundances of elements observed in the solar system, and observed stellar properties [1]. This paper proposed the basic idea that stars are the origin of the elements and then supported this idea with the knowledge of the time.

Since the publication of B^2FH, it has been a goal to better understand both why certain elements are more common than others and the specific relative isotopic abundances of each element. Figure 1.1 shows a recent compilation of the abundances of the isotopes relative to 10^6 Si atoms as a function of atomic mass number, A, for our solar system specifically. This plot is taken from Ref. [2] and includes elemental abundances determined using absorption lines observed in the solar photosphere as well as meteoritic compositions of CI chondrites, which are believed to contain pre-solar grains. Nuclear astrophysics strives to understand the astrophysical processes that were involved in creating this specific pattern of relative elemental abundances.

There is no one answer to this question because there are many contributing processes that have worked together to make the elements present in our Solar System. It has long been believed that supernovae and Asymptotic Giant Branch stars are dominant contributors. However, recent models of Neutron Star Mergers have predicted that they could contribute

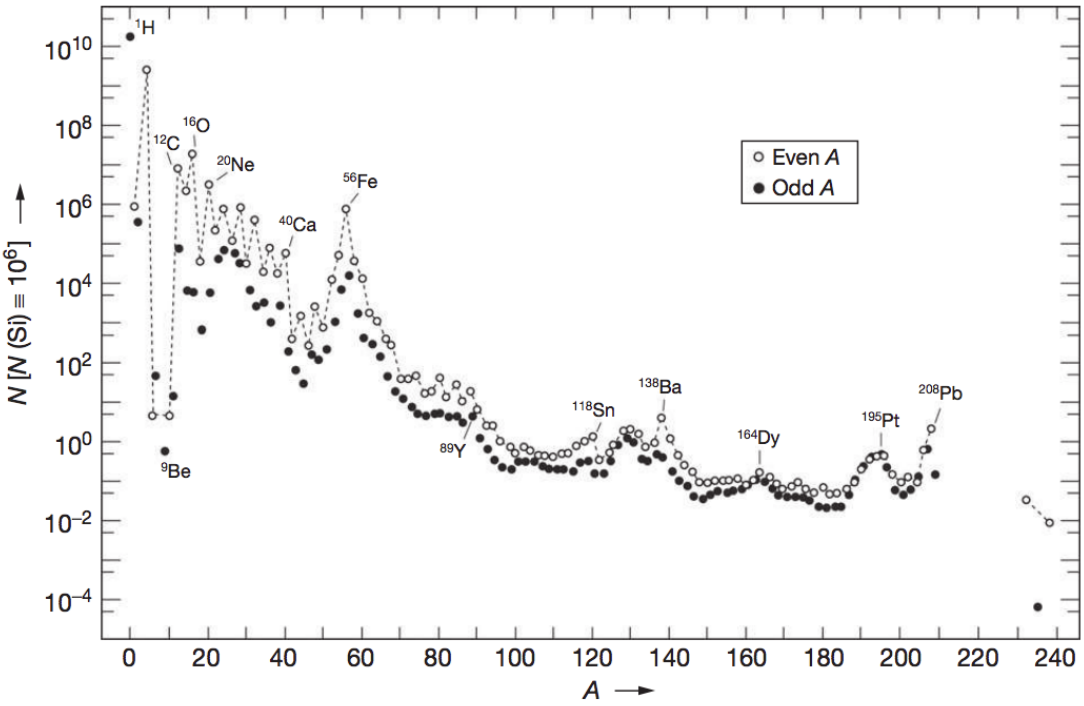

Figure 1.1. The abundance of the elements in the solar system by mass number. The quantity on the y-axis is the number of atoms of each mass number present in the sample per 10^6 Si atoms. Atoms with even mass are shown in open circles and atoms with odd mass are plotted with filled circles. These abundances are taken from solar photospheric absorption lines, CI chondritic meteorites, and other meteorites. This image is reproduced from Ref. [2].

to some of the major peaks in the abundance pattern of the heavier isotopes. In 2017, the first ever observation of a neutron star merger event was made by the LIGO/VIRGO collaboration. They detected the gravitational waves from the inspiral of two neutron stars in the event labeled GW170817 [3]. Optical followup to the event also observed the remnant optical transient resulting from the merger. The light curve decay and color changes of this transient have been determined to be consistent with the presence of lanthanide elements, which are produced in the rapid neutron capture process (r-process), a nucleosynthetic process that forms some of the heaviest elements. From the light curves, Drout *et al.* (2107) estimates that at least ~ 0.05 $M_\odot$ of r-process material is generated from the event [4]. Kasen *et al.* (2017) used optical and infrared observations to estimate the mass of r-process elements that were ejected in this event. They found that there were two different ejection processes asso-

ciated with blue and red light emissions that ejected $\approx 0.025 M_{\odot}$ and $\approx 0.04 M_{\odot}$, respectively [5]. The information we have learned from this event indicates that neutron star mergers produce and eject a substantial amount of r-process materials, underpinning the importance of understanding these events.

In order to accurately describe what elements are produced via r-process nucleosynthesis during a neutron star merger, the composition of both neutron stars must be well understood. Some of the most useful information regarding neutron stars comes from interacting binary systems where interactions of the neutron star with a companion star produce a wide range of observations that can constrain neutron star properties. The most common stellar explosions in our galaxy are Type-I X-ray bursts, which occur in such systems. These X-ray bursts are produced by thermonuclear explosions where nucleosynthesis is occurring via a large number of nuclear processes. From these bursts and models of the conditions within a neutron star, we have learned that neutron stars are extremely neutron-rich environments that are active with nucleosynthetic processes such as electron capture reactions, proton-rich heavy element formation, and even carbon fusion. Figure 1.2 shows the outer layers of a neutron star that are relevant in these processes. Deeper in the layers of a neutron star, the electron capture potential becomes so high that nuclides become extremely neutron rich. In the deeper layers of neutron stars, it is expected that these very neutron-rich nuclei will fuse due to pycnonuclear, or density-driven, nuclear reactions. These reactions may provide an important heat source for the ignition of runaway carbon fusion in the shallower layers of the neutron star, which is thought to trigger rare X-ray superbursts.

More generally, the fusion of neutron-rich nuclei has recently become an area of interest to experimental nuclear physics due to enhancements observed in fusion cross sections likely catalyzed by neutron transfer. In the past, heavy ion fusion has been well studied using stable beams and many properties of nuclei have been shown to have strong impacts on the cross sections of fusion in different systems. These include the collective properties of nuclei, such as the Q values [7] and strengths of neutron transfer reactions [8]. The availability of

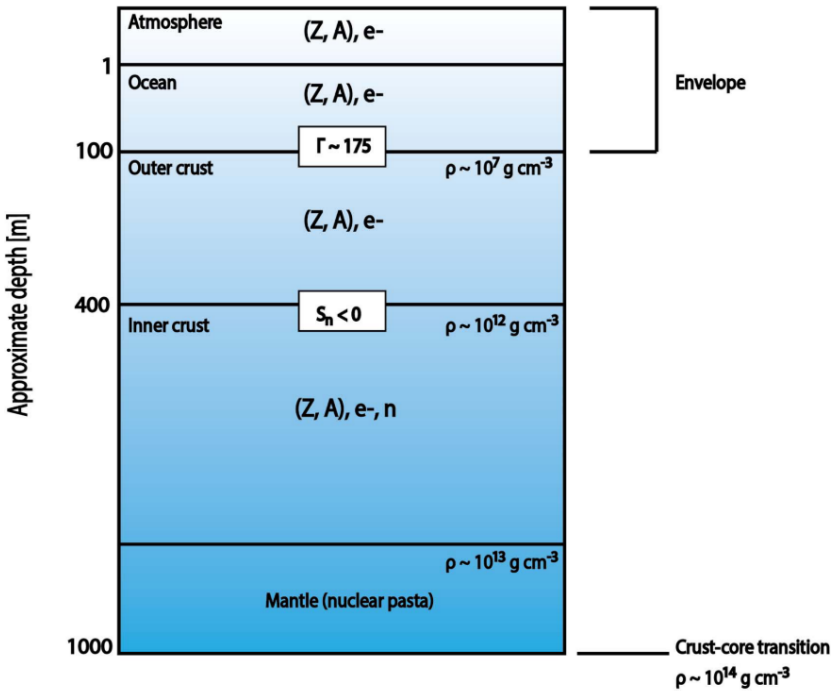

Figure 1.2. This schematic of the outer layers of a neutron star is reproduced from Ref. [6]. Γ is the plasma coupling parameter, which equals about 175 at the depth at which the ocean solidifies into a crystal lattice. S_n is the neutron separation energy and delineates the difference between the outer and inner crusts. The properties of the different layers and their compositions are discussed in the text in section 2.2.

weakly bound particles in colliding nuclei has also been shown to have a significant impact on fusion cross sections [9]. The latter effect can be investigated more easily using radioactive heavy ion beams because this makes available different isotopes of the same element.

In addition, fusion reactions are an extremely important tool for synthesizing new elements and extending the periodic table towards potential new superheavy elements. There is a theorized "island of stability" where new elements are expected to be long-lived or stable that are far more neutron-rich and proton-rich compared to all known elements. The isotopes of these elements are predicted to be extremely neutron-rich and the creation of these elements will require the use of heavy, neutron-rich beams. Before the 1970s, only stable-isotope ion beams were available for nuclear physics studies. Today, the technology for producing radioactive ion beams is under constant development, allowing access to beams further from stability at higher intensities. These beams have been used to synthesize new

isotopes and study reactions on radioactive elements that are important in astrophysical environments.

Extremely neutron-rich carbon isotopes are likely present in the deeper layers of the neutron star crust. Fusion between these carbon isotopes can therefore provide an important heat source for the ignition of superbursts. In the study by Carnelli *et al.* (2014), they measured the carbon-carbon fusion cross sections of heavy ion beams of ^{10}C, ^{13}C, and ^{15}C on a ^{12}C target [10]. As a natural extension of this study, this dissertation presents an experimental measurement of two carbon-carbon fusion reaction cross sections that were made using a neutron-rich ^{16}C beam incident upon stable ^{12}C and ^{13}C targets. Comparing the ^{15}C+^{12}C fusion cross section to ^{16}C+^{12}C allows us to investigate the difference between the one loosely bound valence neutron and two paired valence neutrons. The system ^{16}C+^{13}C, will also allows us to look at the effects of even-even and even-odd fusion reactions. In chapter 2, astrophysical motivation for this study is presented, focusing on the potential importance of these reactions in X-ray superbursts and neutron star energetics. Other motivations from previous studies of fusion are presented in chapter 3. In chapter 4, the experimental procedures and detectors are detailed. The analysis of the data is discussed in detail in chapter 5. The final results are presented in chapter 6, where future work to build upon this study is discussed.

Chapter 2. Astrophysical Motivation

2.1. Binary Star Systems and Accretion

To understand accretion in binary star systems, one must consider not only the gravitational potential around each star but also the effects of the centrifugal force due to the co-rotating frame of reference. The Roche potential defines the potential at each point in space for a two-star system and takes both of these effects into account. Figure 2.1a shows a 3D surface representing the Roche potential for a binary system with the mass ratio $M_2/M_1 = 0.25$. The dips in the center correspond to the gravitational potential wells around each star, the larger dip corresponding to the more massive star. The figure-8 shaped region around the top of the potential wells contains an equipotential line called the Roche lobe, which encloses the region in which material is gravitationaly bound to each individual star. A 2D projection of the Roche lobe around the same binary system is shown in Fig. 2.1b, indicated by the bolded equipotential line numbered 3. Each line shown in this figure corresponds to points of equal potential, with the lines labeled from 1-7 indicating the smallest to greatest potential values. The points labeled L_x correspond to the different Lagrange points, indicating maximum, minimum, or saddle points of the potential. When matter moves from the potential well of one star and reaches the Roche lobe, it is transferred onto the other star via the L_1 point.

Mass transfer proceeds through two possible processes: binary system evolution and stellar winds. The first case, called Roche lobe overflow, occurs in two different scenarios. When one of the stars in a binary system reaches a point in its evolution where its radius expands (for example in the giant phases), its radius can become greater than the Roche lobe equipotential. The matter from the outer layers of this star will be transferred onto the companion star through the first Lagrange point between the stars. In other scenarios, the binary system can evolve such that the Roche lobe shrinks and becomes smaller than the radius of one of the stars. This has the same effect as overflow. An artist's conception of Roche lobe overflow for the binary star system WZ Sagittae is shown in Fig. 2.2. The second

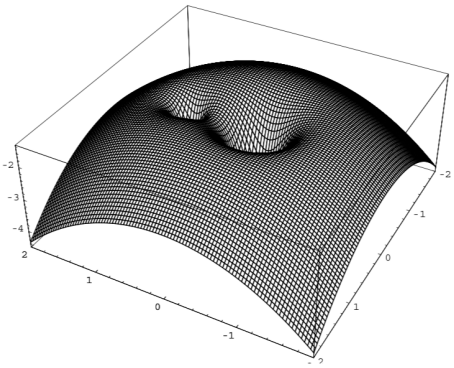

(a)

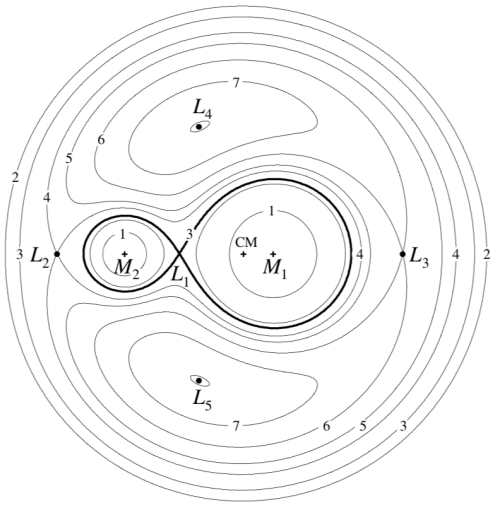

(b)

Figure 2.1. Figure (a) shows a 3D plot of the Roche potential for a binary star system with the mass ratio $M_2/M_1 = 0.25$. The two wells in the center are gravitational potential wells from the two stars. The downward curvature in the Roche potential at the edges is due to the centrifugal term. Figure (b) shows a 2D projection of Fig. (a). The lines represent points of equipotential, increasing in the value of the potential as the numbers of the lines increase from 1-7. The Lagrange points are marked by L_x. L_1 is the saddle point through which Roche lobe overflow transfers mass. L_2 and L_3 are local minima and L_4 and L_5 are local maxima of potential. These images are reproduced from Ref. [11]

possible mass transfer process is caused by stellar winds, which can blow off a significant amount of material that is then transferred onto the companion star. Roche lobe overflow is believed to be far more common than stellar wind driven mass transfer [11].

The accreted material does not fall directly onto the surface of the companion star. Due to its angular momentum, the material spirals in toward the surface, forming a structure called an accretion disk. This transferred material is typically H or He rich, depending on the composition of the companion star, but can also have a higher than solar metal content.

2.2. Neutron Stars

A neutron star is the remnant of a core-collapse supernova where the remnant mass was insufficient to form a black hole. The composition of a neutron star on its own, with no binary companion is assumed to be settled into sedimentary layers and non-dynamic. Neutron stars contain extremely dense nuclear matter and are supported against gravitational collapse by

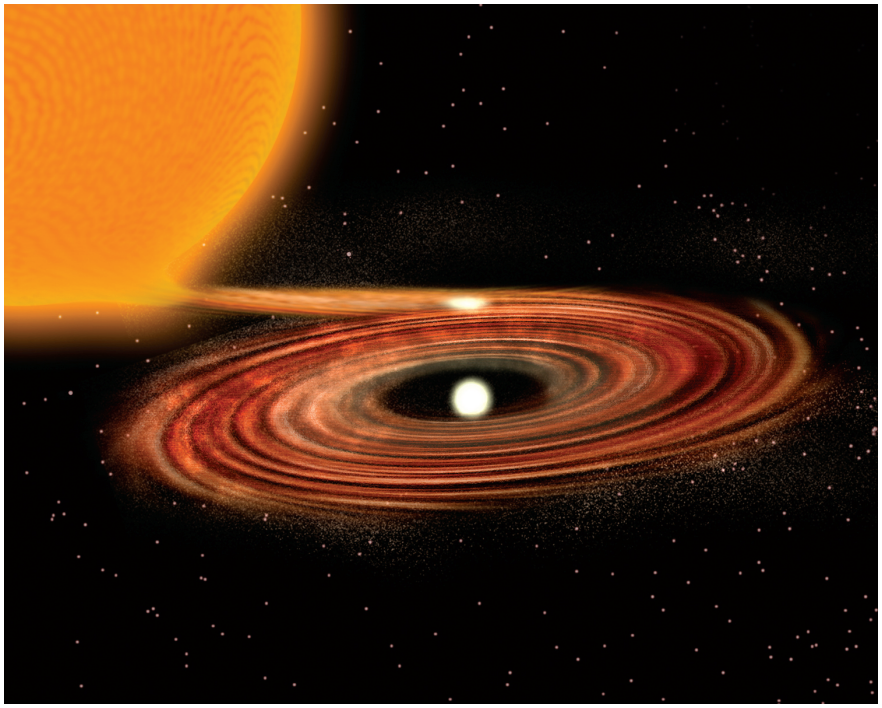

Figure 2.2. An artists conception of the binary star system WZ Sagittae. This image is reproduced from Ref. [12].

neutron degeneracy pressure. Many forms of matter exist within the star, ranging from the typical stellar composition of ionized matter at the surface to possible exotic nuclear pasta states in the mantle. Figure 1.2 shows a diagram of the various outer layers of a neutron star that has been reproduced from Meisel *et al.* (2018) [6]. All of the astronomical observables originate within the outer layers of the neutron star shown in this figure.

In a binary star system with a companion star donating its mass onto the neutron star, the composition of each of these layers is dynamic. To understand the impact of this mass exchange on the neutron star, consider a particular layer of matter as it moves deeper into the star. First, accreted mass is deposited onto the neutron star's atmosphere. Once enough matter has been accreted, an X-ray burst ignites, burning the hydrogen and helium into heavier elements. The ashes of this burning are deposited into the ocean and buried by the continued accretion of new material. As this layer is compacted into the star, it experiences a rising electron capture potential, which means that it becomes likely for a proton in the nucleus to capture an electron and become a neutron. This changes the composition of the

layer to be more and more neutron-rich. Thus, the average Z is lowered and the average N rises as this layer moves through the ocean and outer crust. The transition to the inner crust happens when the neutron-separation energy becomes less than zero. This means that it is energetically disallowed for additional neutrons to be captured onto the nuclei. The elements in the layer are now so neutron rich that they are at the neutron drip line and there are free neutrons in this area. Finally, when densities become high enough, the matter begins to exhibit group properties called nuclear pasta.

In the deep crust of a neutron star, pycnonuclear (density-driven) fusion provides an internal heat source for the star. When there is no accretion, this powers thermal surface X-ray emission of the neutron star. Due to the location in the neutron star, these pycnonuclear fusions are happening between extremely neutron-rich nuclei, near the neutron drip line. To understand the inner workings of a neutron star, it is thus important that nuclear reactions between very neutron-rich nuclei be well understood. The nuclear reaction rates depend directly on the reaction cross sections, which can be measured in the laboratory.

2.3. Type-I X-ray Bursts and Nucleosynthesis

A binary system of particular interest is one in which Type-I X-Ray Bursts (XRB) occur. Type-I XRBs are the most common type of stellar explosion in our Galaxy. These XRBs occur in binary star systems that comprise a compact neutron star and a companion star that donates its material to the neutron star. This accretion mostly happens via Roche lobe overflow, but can be stellar wind driven as well. When the accreted material on the neutron star becomes hot and dense enough, runaway thermonuclear burning is triggered. The resulting XRB lasts 10-100 s and releases about 10^{39-40} ergs. They have typical recurrence times on the order of a few hours to days.

Figure 2.3 shows the bolometric luminosity over time of three different X-ray bursts from different sources. The sources 4U 1820-303, SAX J1808.4-3658, and GS 1826-24 are thought to have accretion compositions that are pure-He, He-rich, and H-rich, respectively. The shape of the X-ray burst light curve is determined by the type of fuel (the accreted material

composition), the energetics of the nuclear reactions, the temperature profile of the burning, and the ignition depth. The uncertainties in the energetics of the nuclear reactions dominate the uncertainties in XRB models. The models require a complex sequence of over a thousand reactions on over three hundred nuclei. Fortunately, not all of these reactions have an equal effect on the characteristics of the burst, and the most important reactions can be identified via sensitivity studies, like those in Refs. [13] and [14].

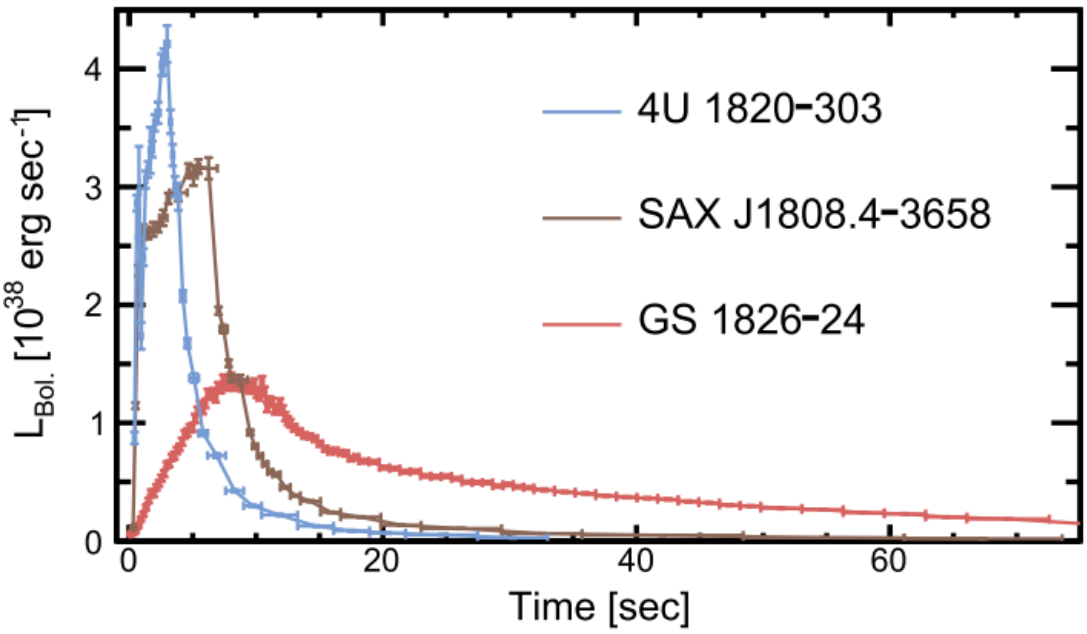

Figure 2.3. These Bolometric luminosity light curves were observed with the Proportional Counter Array (PCA) on-board the satellite-based Rossi X-ray Timing Explorer (RXTE). There are three different sources for each of these bursts: 4U 1820-303, SAX J1808.4-3658, and GS 1826-24. These bursts are thought to have accretion compositions that are pure-He, He-rich, and H-rich, respectively. This image is reproduced from Ref. [6].

Before an XRB, on the surface of the neutron star, the hot CNO cycle is occurring under quasi-stable conditions. When the temperature becomes high enough, the triple-α process is ignited, raising temperatures further and igniting helium burning. The helium burning reactions [e.g. (α,p) and (α,γ)] break out of the hot CNO cycle and begin the αp-process. In Fig. 2.4, a typical reaction path in an XRB is shown on a chart of nuclides configuration, with isotopes plotted along horizontal lines and different elements plotted

along vertical lines. The stable isotopes are represented as grey boxes, and the white boxes represent radioactive isotopes that are proton-rich relative to stability. In the αp-process, an α particle fuses with an even-Z, even-N nucleus, followed by the immediate emission of a proton. The product quickly captures another proton and emits a γ-ray, resulting in a proton-rich even-even nucleus. The product nuclei are then in (p,γ) - (γ,p) equilibrium awaiting β^+ decay. The β^+ decay half life is sometimes so long that a subsequent (α,p) reaction takes place, which causes the burning to create even more proton-rich radioactive nuclides. As heavier nuclei are created, the helium fuel is consumed and the Coulomb barrier inhibits further (α,p) reactions. The dominant process becomes hydrogen burning, or the rapid-capture proton process (rp-process). In this process, protons are captured onto the proton-rich radioactive nuclides, which then de-excite through γ-ray emission. This proton capture process now competes with the β^+ decay of the nuclides. The rp-process must end when the (p,α) reaction channel begins competing with the (p,γ) reaction channel in the SnSbTe cycle, identified by the study in Ref. [15].

The colored lines in Fig. 2.4 show which nuclear reaction sequences are mainly responsible for the shape of the XRB light curve. The αp-process is responsible for the bulk of the rise in X-ray flux while the rp-process is responsible for the peak flux and the shape of the decay of the light curve. It is interesting to note that the peak X-ray flux occurs near the formation of the most tightly bound nuclei (A = 60) near iron. The reason for this will be discussed in section 3.1.

X-ray bursts result in the production of many heavy nuclides in relative abundances that are unique to this specific astrophysical environment. An example abundance pattern of the product nuclides, or ashes, resulting from an XRB is shown in Fig. 2.5. This abundance pattern was calculated by Schatz *et al.* (2001) using an XRB model that assumed an accretion rate of 10% of the Eddington limit with a composition of hydrogen and helium in solar proportions and a metallicity of Z = 10^{-3} [15]. The XRB event is not energetic enough to release much of the burst ashes from the gravitational pull of the neutron star. Thus,

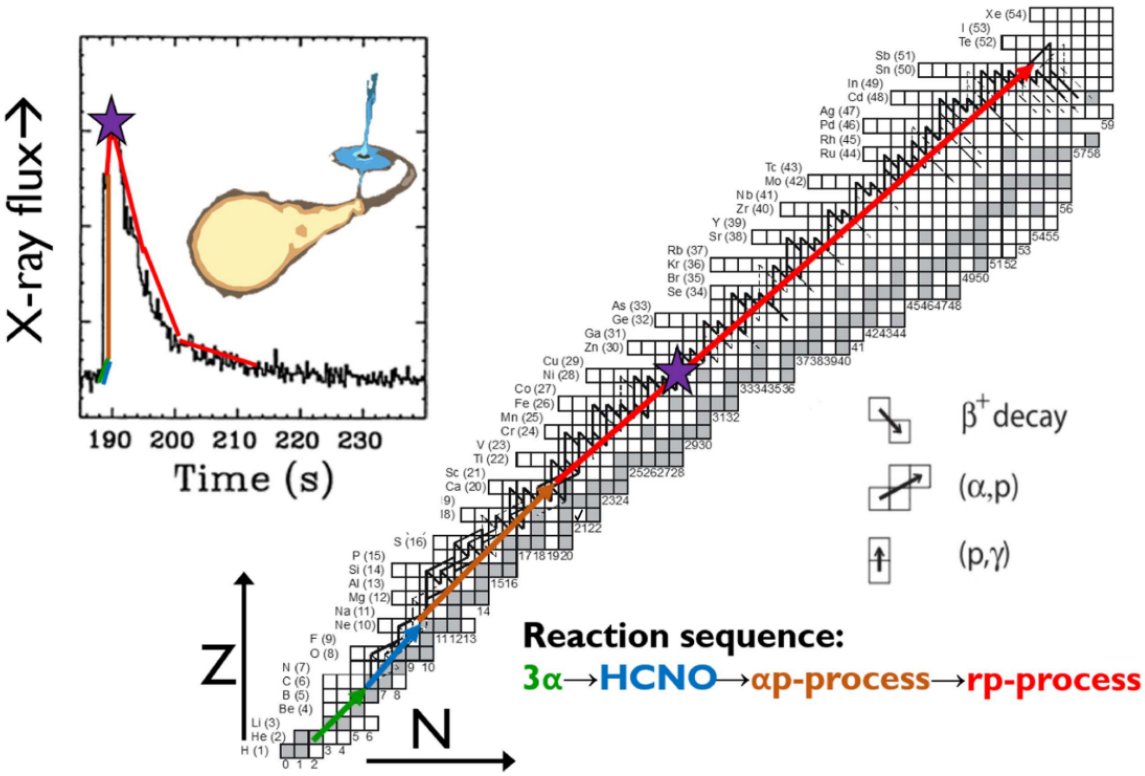

Figure 2.4. The reaction sequence of a representative Type-I XRB as modeled in Ref. [15] is shown as the black lines on the chart of nuclides. Reaction pathways that occur less than 10% of the time have dashed lines and solid lines are pathways that occur greater than 10% of the time. This is shown alongside a representative XRB light curve with each of the reaction sequence processes highlighted with different colored lines relating them between where they happen on the chart of nuclides and the part of the light curve they have the greatest effect on. This image is reproduced from Ref. [6].

the majority of these XRB ashes are deposited onto the surface of the neutron star after the burst occurs and become a part of the composition of the neutron star. This may be important for influencing later bursts and the future evolution of the system.

2.4. X-Ray Superbursts

Occasionally, X-ray bursts that have a duration on the order of hours, 2-3 orders of magnitude longer than normal Type-I XRBs, have been observed in binary systems that also undergo regular Type-I XRBs. Because these bursts last so much longer than regular ones, their energy output is also 2-3 orders of magnitude larger. These extra-long bursts have been called superbursts, and a representative light curve from a superburst observed from

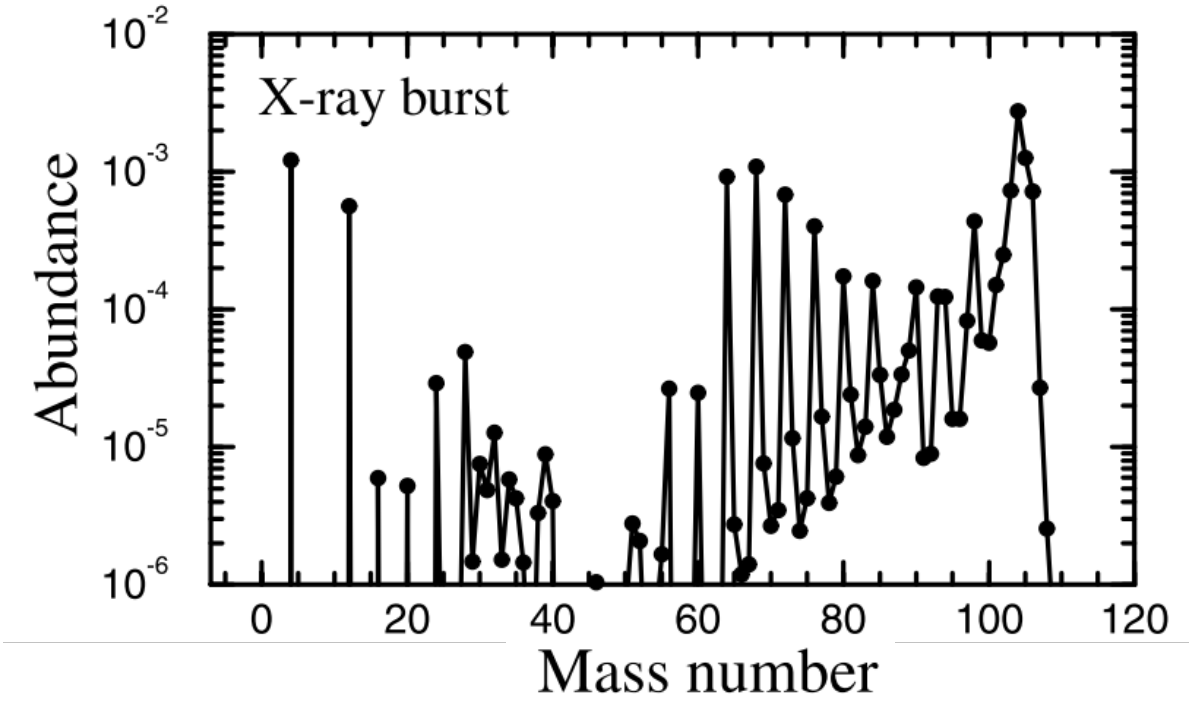

Figure 2.5. The final abundance distribution of the XRB ashes is shown as a function of mass number for the XRB model used in Ref. [15] and described in the text. This image is reproduced from Ref. [15].

the object 4U 1636-536 is shown in Fig. 2.6. The peak Bolometric luminosity of this burst is lower than the bursts in Fig. 2.3. It is also much slower to rise (about 10 minutes) and much longer burning (a few hours). These events are very rare. As of 2018, only 26 superbursts had been detected from 15 different neutron stars [6]. Despite their infrequency, these events offer an important peek inside of the deep layers of neutron stars, where conditions are extremely dense and neutron-rich.

The differences between superbursts and regular XRBs suggest that a different nucleosynthetic process is at work, despite the fact that they both have qualitatively similar light curves. Figure 2.7 shows that this is indeed the case. The abundance verses mass number, A, for the ashes from an X-ray superburst are shown in the gray-filled histogram and consist primarily of ^{56}Fe and elements of similar mass. The filled red histogram and red-lined histogram show alternate ash compositions for regular Type-1 XRBs, which are drastically

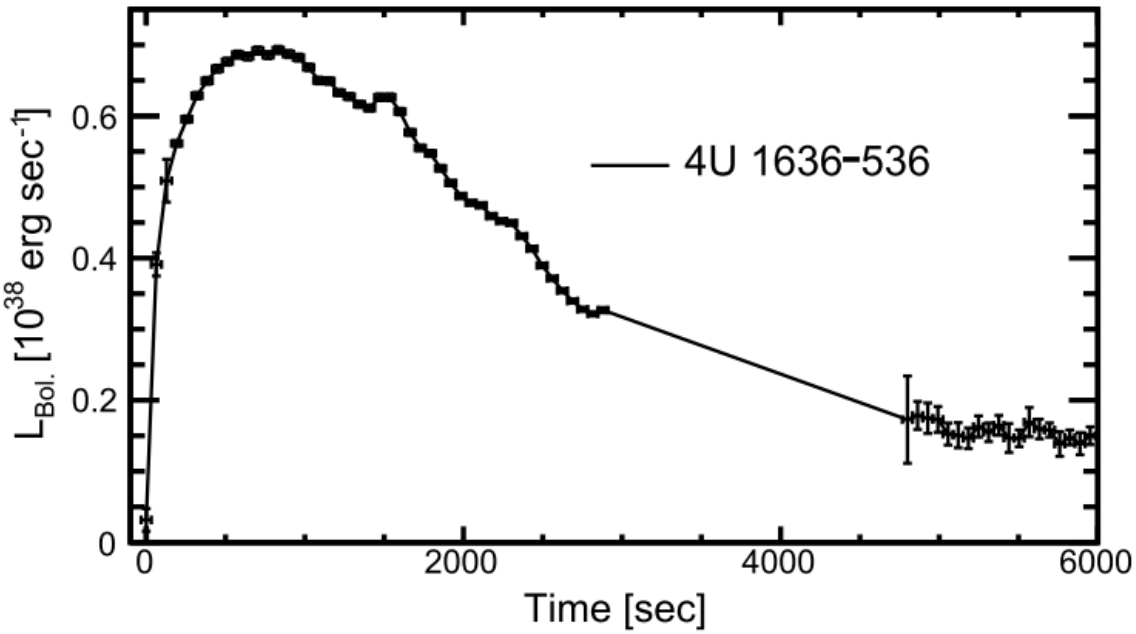

Figure 2.6. This Bolometric luminosity light curve was observed with the PCA on-board the satellite-based RXTE. This is a superburst that lasts much longer and releases much more energy than a typical XRB. The gap in the data is due to occultation by the Earth. This image is reproduced from Ref. [6].

different. It is inferred from models of the superburst X-ray spectra that a superburst is triggered by runaway $^{12}C + {}^{12}C$ burning within a layer of carbon in the ocean, in contrast to regular XRBs which burn on the surface of the neutron star.

This carbon burning dominantly proceeds through the channel $^{12}C(^{12}C,\alpha)^{20}Ne$. Some of the released α particles are captured onto ^{12}C, producing ^{16}O. The ^{16}O reacts with ^{12}C and ^{16}O, producing ashes that are rich in ^{28}Si. The ^{28}Si photodisintegrates when temperatures become high enough, creating free α's. These are quickly captured to form ^{56}Ni, which transforms into ^{56}Fe by electron capture when the burst ends and the environment begins to cool. The precise composition of the ashes shown in Fig. 2.7 depends on the nuclear capture reaction rates and the probability of photodisintegration.

In order for the carbon layer to be ignited, enough heat needs to be supplied to it by some mechanism. The amount of heat supplied to the carbon layer has been studied but is fairly uncertain because it depends on many factors such as which heat sources are present

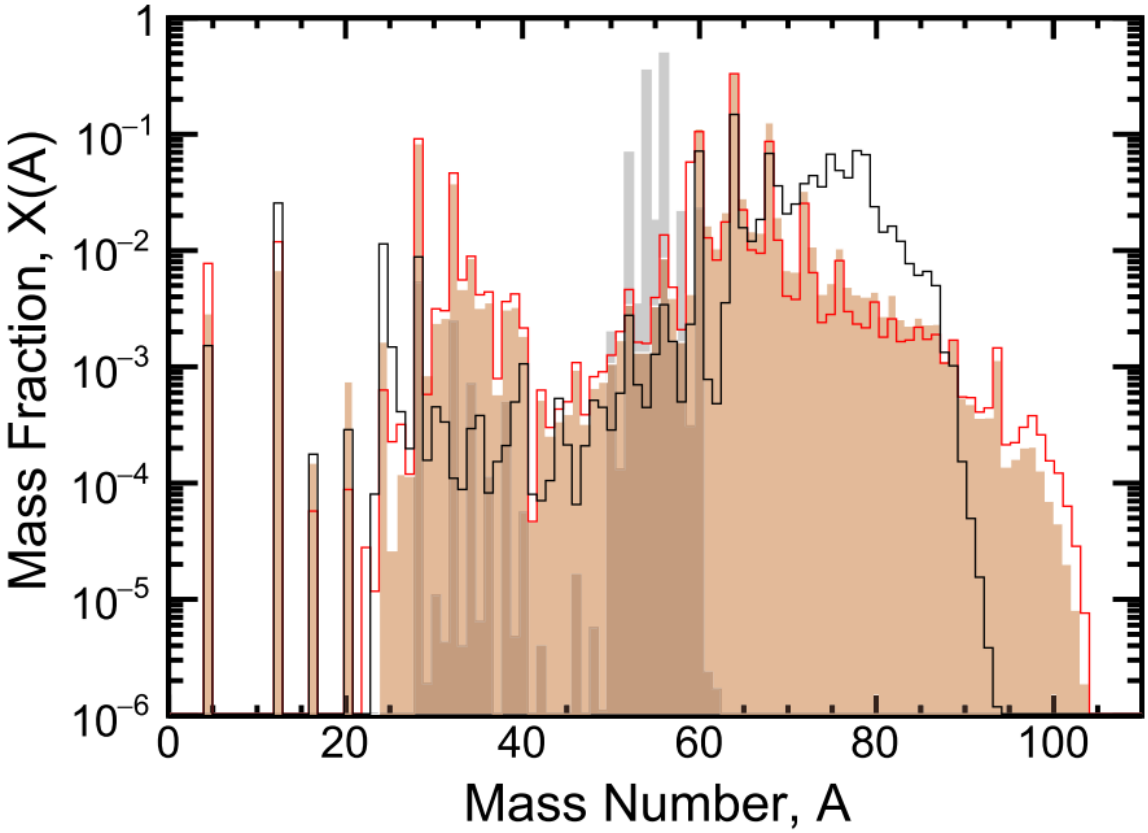

Figure 2.7. The predicted ash abundances are shown versus mass number for different nucleosynthetic processes occurring in neutron star binary systems. The black-lined unfilled histogram represents the ashes from stable surface burning. The gray-filled histogram shows the ashes from a superburst. The red-filled translucent histogram and red-lined unfilled histogram represent two different Type-I XRBs with the nuclear reaction rate of ^{59}Cu(p,γ) varied. This image is reproduced from Ref. [6].

and how well heat is transferred or trapped. The inferred column depth for carbon burning ignition has been determined to be $\sim 10^{12}$ g/cm^2 for most superbursting sources. The work done by Keek *et al.* (2008) showed that heating in the crust of the neutron star from electron captures, neutron emissions, and pycnonuclear (density-driven) fusion reactions is insufficient to raise the crust temperature enough to ignite ^{12}C burning at that column depth for the specific superburst source they studied [16]. However, the work by Gupta et al. (2007) showed that electron captures to excited states in heavy elements in the neutron star crust can supply the right amount of heat for superburst ignition in the ^{12}C layer [17]. Additionally, the pycnonuclear fusion reaction rates are subject to huge uncertainties that,

when reduced, could show that this source of heating is more or less significant than it is currently thought to be.

Superbursts are extremely interesting to study because of these open questions. With this probe into the deeper layers of the neutron star, a better understanding of the intensely neutron-rich environment can be developed, which can in turn affect how the nucleosynthesis of neutron star mergers is understood. Considering that pycnonuclear fusion in the deep neutron star crust is a possible contributor of heat for the ignition of a superburst, reducing the nuclear physics uncertainties on the reaction rates of neutron-rich isotopes of various elements present in that environment is necessary. The fusion reaction rates of neutron-rich carbon isotopes have been identified by Ref. [18] to be important in this environment. This is part of the motivation of this work to study fusion in the most neutron-rich carbon-carbon systems to date.

Chapter 3. Nuclear Physics Motivation

3.1. Nuclear Fusion

Nuclear fusion reactions are a large area of focus in the field of nuclear physics. Fusion has been one of the most utilized tools for producing and studying nuclei at the extremes of spin and isospin and for the creation of superheavy elements. Fusion has large cross sections at energies above the Coulomb barrier. It is the main mechanism by which most of the elements lighter than iron have been created, and it produces most of the nuclear energy in quiescent stellar environments. This is because fusion is mainly an exothermic process for elements lighter than iron and results in elements reaching their most tightly bound energetic states.

Fusion is an exothermic process for light nuclei because it produces more tightly bound products. The binding energy of a nucleus is defined as

$$BE = (m_A - Zm_H - Nm_n) \times c^2 \tag{3.1}$$

where m_A, m_H, and m_n are the masses of the atom, an ^{1}H atom, and a neutron, respectively, in units of MeV/c^2, Z is the proton number, and N is the neutron number. The binding energy of a nucleus represents the amount of energy released in assembling its constituent nucleons. Figure 3.1 shows a plot of the average binding energy per nucleon for each total nucleon number, A. The most tightly bound nuclei have masses around $A = 60$ and include the nuclides near in mass to iron as well as iron itself. Lighter nuclei ($A < 60$) release energy as they fuse and heavier nuclei ($A > 60$) release energy as they fission.

Fusion is the formation of a compound nucleus which has a total charge, Z_c, and mass number, A, equal to the sum of the target and projectile system [20]. The compound nucleus formed by fusion must also live long enough that the details of the entrance channel diagram are lost, though this is an extremely short amount of time $\sim 10^{-22}$ s. The compound nucleus is in a highly excited state just after fusion and will therefore decay (or de-excite) via a

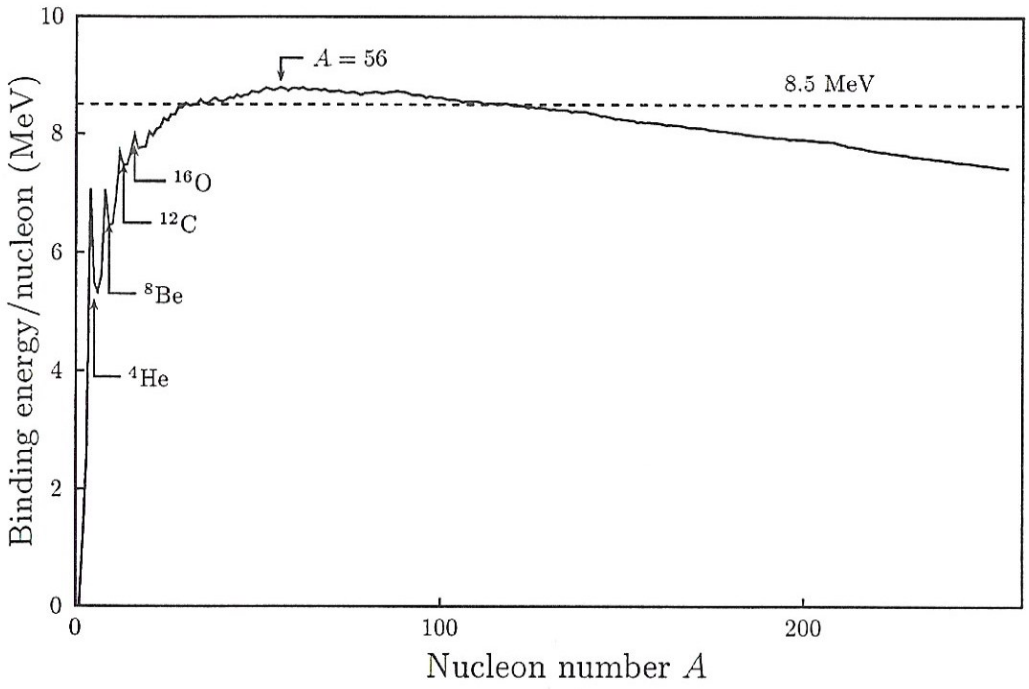

Figure 3.1. The average binding energy per nucleon is shown as a function of mass number A for the most stable nucleus of each nucleon number. The most tightly bound, or stable, nuclei are those with similar mass number to iron (A $\approx$ 56) where the binding energy per nucleon maximum value of about 8.5 MeV. This image is reproduced from Ref. [19].

statistical process of particle and γ-ray emission. (In nuclei with $Z_c < 60$, the probability for fission to occur is negligibly small and is therefore not of concern in this work, which only considers $Z_c = 12$ [20].) The de-excitation of the compound nucleus proceeds through the emission, or evaporation, of neutrons, protons, alphas, and high-energy γ-rays resulting in an evaporation residue (i.e. a final ground-state nucleus). In this work, the evaporation residue is interchangeably referred to as the residual ion, residual nucleus, and residual nuclide.

The nuclear cross section is a quantity used to characterize how likely it is for a reaction to occur. In the case of fusion, the cross section can be given as

$$\sigma_{CN} = \pi\lambda^2 \sum_{L=0}^{\infty} (2L+1) T(L) P_{CN}(L) \tag{3.2}$$

where L is the angular momentum quantum number, $T(L)$ is the normal L-dependent transmission coefficient for the interaction potential, and $P_{CN}(L)$ is the probability that a com-

pound nucleus (CN) is formed, which can be assumed to be unity for the purposes of this work because $Z_c < 60$. For systems that are very unlikely to undergo fission, Eq. 3.2 represents the total fusion cross section.

Which evaporation residue is ultimately produced by fusion is determined by the conservation of 4-momentum, or energy and momentum. The reaction Q value is the amount of energy created (positive Q value) by a reaction or required (negative Q value) for the reaction to take place. It is calculated using the equation

$$Q = (m_{reactants} - m_{products}) \times c^2 \tag{3.3}$$

where $m_{reactants}$ is the total mass of all reactants in the units MeV/c^2, $m_{products}$ is the total mass of all products in the same units, Q is the Q value in MeV, and c is the speed of light. As an example, consider one of the projectile-target pairs studied in this work, ^{16}C+^{12}C, which produces the compound nucleus ^{28}Mg* in a highly-excited state. This reaction is exothermic and therefore produces energy that causes the excitation of the compound nucleus with Q = 28.71 MeV. This, plus the center-of-mass energy before fusion, is the excitation energy of the nucleus that will be used to evaporate particles (in the center-of-mass frame). If the first evaporation is a neutron, then the next reaction to occur is ^{28}Mg* $\rightarrow$ n + ^{27}Mg*, with a Q value of Q = -8.50 MeV. The evaporation takes away 8.50 MeV of the excitation energy of ^{28}Mg* plus some kinetic energy which is distributed between the neutron and ^{27}Mg* according to momentum conservation. Therefore the excitation energy of ^{27}Mg* is determined by the Q value of the neutron separation and its kinetic energy. Further particle evaporations continue until the excitation energy of the residual nuclide is not high enough to evaporate a proton, neutron, or α particle. If the residual nuclide is in an excited state, it will emit a γ-ray to its ground state and will β^--decay according to its half-life if it is radioactive.

3.2. Previous Studies of Fusion

Both theoretically and experimentally, fusion cross sections have been shown to depend on the collective properties of nuclei, on the Q values and the strength of neutron transfer reactions, and/or on the availability of weakly bound nucleons in the colliding nuclei [21]. Fusion reactions are useful for studying nuclear collective properties, the equation of state, and for producing new isotopes. Heavy-ion fusion experiments have been used to extend the periodic table beyond elements that can be synthesized with light-ion beams or neutrons. There is a theorized island of stability for superheavy isotopes that lies in a region of the chart of nuclides with a higher atomic number than any known element and is far more neutron rich. The theoretical superheavy elements in this island are expected to be long-lived enough to be observable once created. Creating these in the lab presents very interesting challenges because, at these masses, fission now competes strongly with evaporation for the de-excitation of the compound nucleus. In order to reach these new superheavy elements, a better understanding of the processes involved in their formation via fusion is essential. For example, fusion hindrance has been observed at energies far below the Coulomb barrier, but also at high energies. Thus, knowing the energy at which the fusions are most likely to occur will guide experiments towards discovery.

This work focuses on the study of fusion reactions involving different isotopes of carbon. The occupation of different energy levels in the nuclear shell model by the neutrons in different isotopes of carbon is expected to have an effect on the size of the nucleus and fusion cross section. Figure 3.2 shows the low-energy states of the nuclear shell model with the closed shells indicated by the numbers in red circles. Each line in the spin-orbit coupling split states can hold two nucleons, one spin-up and one spin-down. Thus, a filled 1s shell will have two nucleons in it. ^{4}He is an example of a nucleus with a closed shell of protons and a closed shell of neutrons because the s shell is filled for both. As seen in Fig 3.1, this is one of the most tightly bound nuclei. As another example, consider ^{14}C that has 6 protons and 8 neutrons. The neutrons fill both the s and p shells completely, making ^{14}C a neutron

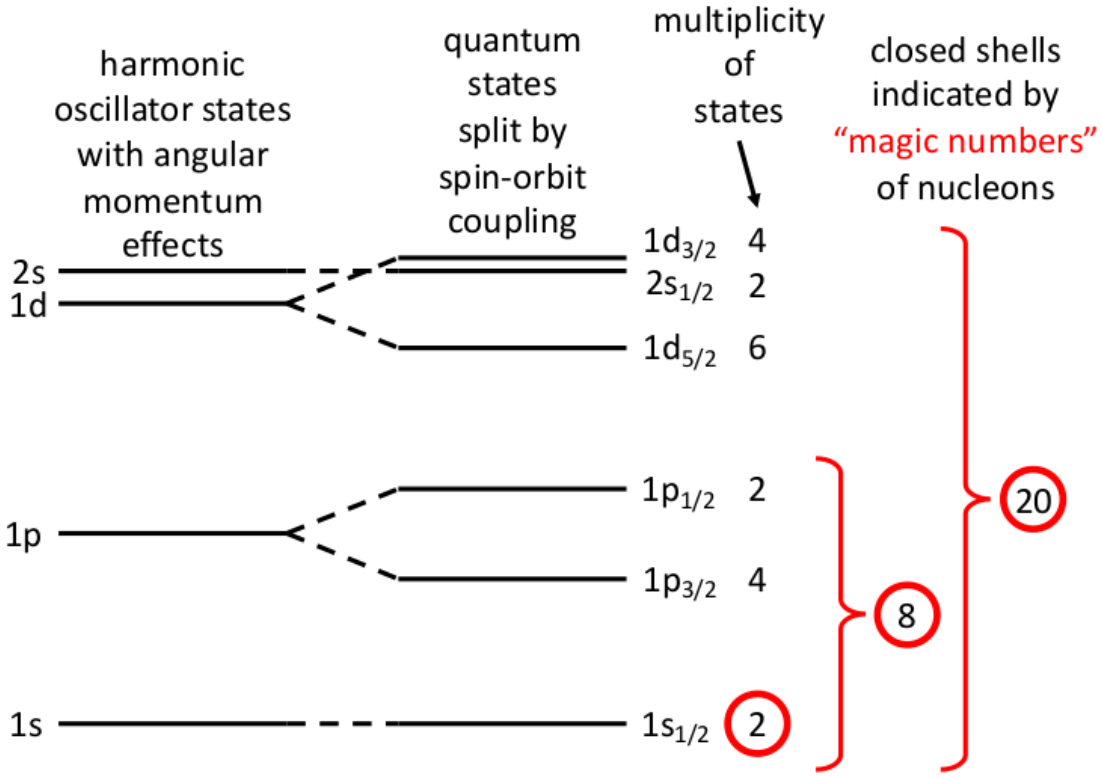

Figure 3.2. The nuclear shell model is shown with the different angular momentum states of the harmonic oscillator levels. These levels are split by spin-orbit coupling effects. The number of nucleons that may occupy each state is indicated next to its label. The magic numbers for closed shells are indicated by the numbers inside the red circles.

closed-shell, or magic, nucleus. ^{14}C is a radioactive isotope, but it is extremely long-lived and considered to be a spherical nucleus because of its tightly-bound closed shell of neutrons and its large negative Q value for neutron transfer. The trend generally holds for all nuclides that when there is a closed shell of either protons or neutrons, or both, the nucleus tends to be longer lived than its neighbors, or stable, and has smaller reaction cross sections.

The ^{15}C nucleus has one additional neutron occupying the sd shell, outside of the closed shell. It occupies the $2s_{1/2}$ orbital and enhances ^{15}C's interaction cross section compared to that of ^{14}C [21]. To determine the effect that the one weakly-bound neutron in ^{15}C has on the fusion cross section, an experiment was conducted with beams of ^{14}C and ^{15}C impinged on a ^{232}Th target by Alcorta *et al.* (2013) [9]. The results of this study showed that at low energies the fusion cross section of ^{15}C with ^{232}Th was far enhanced over that of ^{14}C. These

are the types of effects that must be well understood for the production of heavier fusion systems. For a thorough review of the most recent studies of fusion systems, refer to Ref. [21]. It would be interesting to investigate fusion using ^{16}C, which has two paired neutrons in the sd shell.

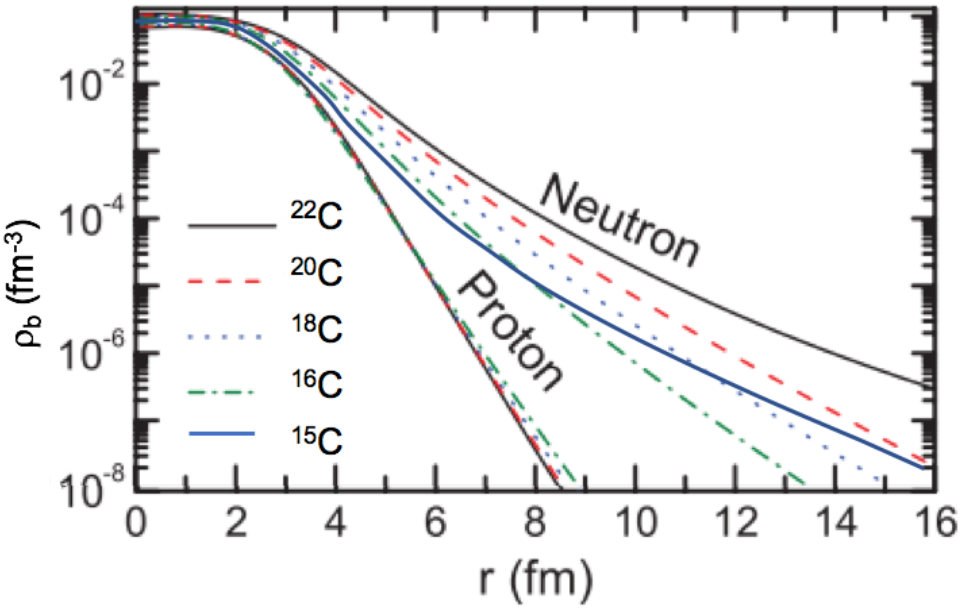

Figure 3.3. Neutron and proton density distributions for various isotopes of carbon. This plot has been adapted from Lu *et al.* (2013) to show the difference between the ^{15}C and ^{16}C radii [22].

Past studies of the structure and radius of the ^{16}C nucleus have produced contrasting results. A study performed by Imai *et al.* (2004) found that anomalous nuclear structure may be required to describe the ^{16}C nucleus [23]. However, a later experimental study by Wuosmaa *et al.* (2010) showed that the ^{16}C nucleus was well described as having the two sd-shell neutrons occupying a mixture of the $1d_{5/2}$ and $2s_{1/2}$ orbital [24]. Results from Ozawa *et al.* [25] and Ahmad *et al.* [26] disagree with this, though. These studies have determined the Root-Mean-Square (RMS) radii for different carbon isotopes based on their interaction cross sections at energies far above the Coulomb barrier. Both of these studies find that the RMS radius of ^{16}C is enhanced over that of ^{15}C by greater than 12%, far more than the $\sim$

2% increase expected from scaling by $r = r_0 A^{1/3}$. This is an even larger enhancement than the 10% enhancement in radius these studies found for the radius of ^{15}C compared with ^{14}C.

The RMS radii only tell part of the story about the differences between nuclei. To better understand how different nuclei compare, it is helpful to look at their wavefunctions. The density distributions of different carbon isotopes calculated using the Relativistic Hartree-Fock-Bogoliubov (RHFB) theory have been adapted from Ref. [22] and are shown in Fig. 3.3. The neutron density distribution of ^{16}C is predicted to be larger than ^{15}C until large (> 7 fm) distances. However, the wavefunction of ^{15}C extends to larger radii than ^{16}C, showing an enhancement in the tail of the density distribution at larger radii. (The RMS radius of ^{16}C is between 2.70 - 3.04 fm according to Refs. [25] and [26].) A comparison between the fusion cross sections of ^{15}C and ^{16}C, fusing with the same nuclide species, is of interest to test whether the larger RMS radius of ^{16}C or the extended tail of the ^{15}C wavefunction enhances the cross section.

In addition, accurate astrophysical models of the neutron star crust require accurate neutron-rich fusion cross sections. Carbon fusion has been previously studied both theoretically and experimentally. The theoretical study by M. Beard *et al.* (2010) calculates the cross section for 36 combinations of carbon isotopes fusing [18]. The cross section is expressed in terms of the astrophysical S-factor that factors out the exponential dependence of the cross section on energy due to transmission through the Coulomb barrier, simplifying extrapolations to sub-Coulomb barrier energies [27]. To do this, fusion was modeled using the São Paulo potential and the barrier penetration formalism [28]. Figure 3.4 shows the results for a few of these fusion systems, ranging in nucleon number from ^{10}C+^{10}C fusion to ^{24}C+^{24}C fusion, and including ^{16}C+^{12}C. The plot's y-axis is the log of the S-factor, showing the dramatic increase by orders of magnitude of the S-factor as the carbon fusion system becomes neutron rich. Similar predictions of the S-factor have been made more recently by Singh *et al.* (2019) and are discussed in Ref. [29]. Due to limited intensities of radioactive ion beams, these systems can not be experimentally well characterized below the Coulomb bar-

rier, but calculations such as these extrapolate S-factor values to energies below the Coulomb barrier. To ensure the accuracy of these models, they need to be tested experimentally with available systems at energies that can be well characterized.

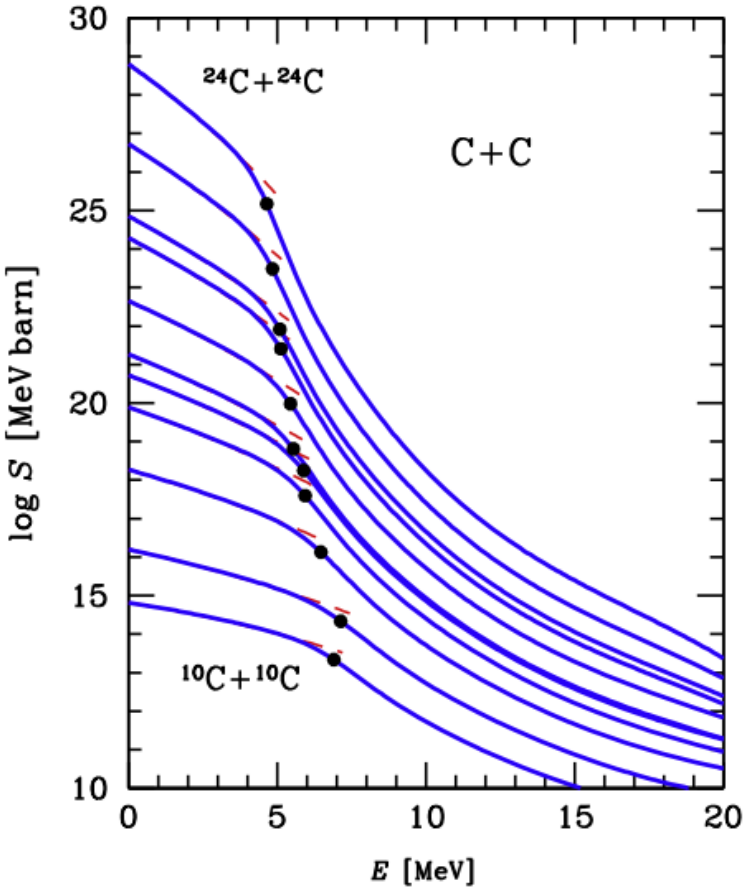

Figure 3.4. This plot is reproduced from Ref. [18]. It shows the log of analytic approximations for S(E) is plotted versus center-of-mass energy for different isotope combinations of ^{x}C+^{y}C fusion. From bottom to top, the carbon isotopes fusing are (x,y) = (10,10), (12,12), (12,16), (12,20), (16,16), (12,24), (16,20), (16,24), (20,20), (20,24), and (24,24). The solid blue curves show a 9 parameter approximation to of the S-factor, the dashed red curves show a 3 parameter approximation, and the filled dots are plotted where the center-of-mass energy equals the Coulomb barrier energy.

A previous study conducted by Carnelli *et al.* [10] used a very similar experimental approach to the one we have utilized, which is discussed in chapter 4. This study was an experimental investigation of the total fusion cross-section of various carbon isotopes fusing with one another. They used radioactive and stable beams including ^{10}C (proton-rich), ^{13}C

(stable), and ^{15}C (neutron rich) with a stable ^{12}C target. Figure 3.5 shows the measured fusion cross sections for each of these three isotopes. The stable fusion system, ^{13}C+^{12}C in panel b), shows good agreement with a previous study by Kovar *et al.* (1979) and is a nice benchmark to show that the experimental setup used produces results consistent with those previously obtained. This system also shows decent agreement with the two theoretical predictions of the cross section. One of these models uses a coupled-channels approach to approximate the cross section (black solid line). The blue dashed line is a São Paulo Optical Potential model.

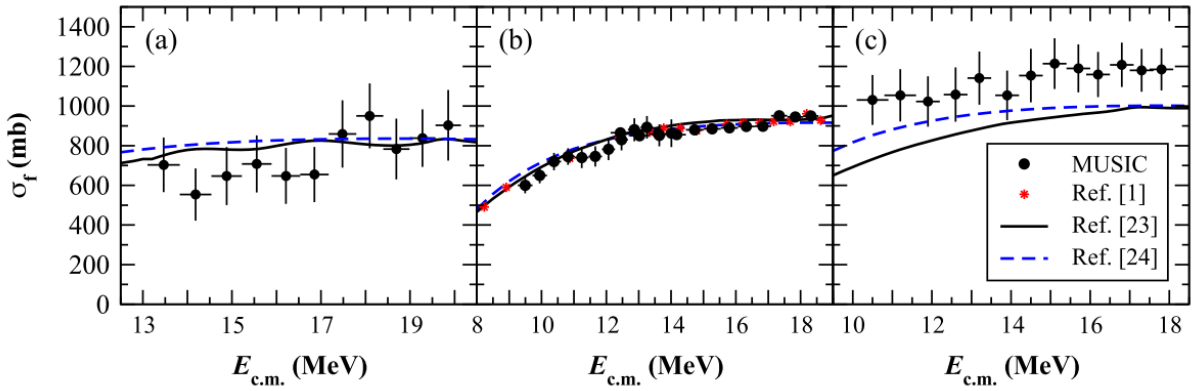

Figure 3.5. The total fusion cross sections measured by Carnelli *et al.* are shown for the fusion systems ^{10}C+^{12}C (a), ^{13}C+^{12}C (b), and ^{15}C+^{12}C (c). The data for the ^{13}C+^{12}C fusion system are compared to previous data from Kovar *et al.* (1979) [30]. The solid black lines are theoretical cross sections from coupled-channels calculations [31]. The dashed blue lines are predictions from a barrier penetration model using the São Paulo potential [32]. Reproduced from Ref. [10]

Panel a) in Fig. 3.5 shows the cross section of the proton-rich ^{10}C fusing with ^{12}C. This agrees poorly with the theoretical cross-sections. The ^{10}C nucleus is a short-lived radioactive isotope and is therefore not as well studied or modeled as the ^{12}C or ^{13}C nuclei. Additionally, this study was the first study conducted on this system. This highlights why it is important to conduct experimental studies that push to new fusion systems. As theory becomes better at matching measured cross-sections, it can become more accurate when predicting systems that can't be studied in the lab due to our limited capacity to produce highly exotic isotopes.

Panel c) in Fig. 3.5 shows the total fusion cross section of ^{15}C+^{12}C fusion, studied with the neutron-rich radioactive isotope. The agreement between the measured and theoretical cross-sections is poor. It is informative to see all three of these systems plotted on the same axis to understand how these systems differ from one another. Figure 3.6 illuminates the differences between these different fusion systems due to the addition or removal of neutrons from the stable ^{12}C nucleus. Removing two neutrons lowers the cross section of the fusion reaction while adding three neutrons increases the fusion cross-section. This trend is seen in theoretical predictions of these cross sections and extends up to the extremely neutron-rich isotopes of carbon we expect to be present in the deeper layers of a neutron star. The work presented in this dissertation naturally builds upon this work using similar experimental techniques. The ^{16}C+^{12}C and ^{16}C+^{13}C total fusion cross sections have been measured and will be compared to the results obtained by Carnelli *et al.* as well as the theoretical cross sections calculated by Beard *et al.* (2007) and Singh *et al.* (2019).

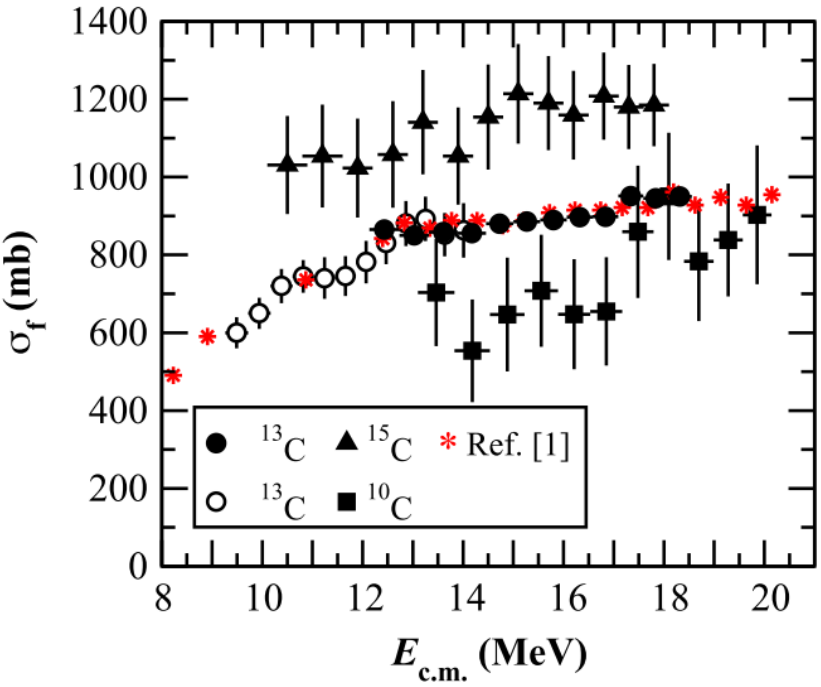

Figure 3.6. The total fusion cross sections measured by Carnelli *et al.* are shown for the fusion systems ^{10,13,15}C+^{12}C. The ^{13}C beam was produced at two different energies, indicated by the open and filled circles. The data for the ^{13}C+^{12}C fusion system are compared to previous data from Kovar *et al.* (1979) [30]. Reproduced from Ref. [10]

Chapter 4. Experimental Procedures

4.1. Overview of Experimental Runs

The goal of this experiment was to measure the total fusion cross sections of the neutron-rich radioactive isotope ^{16}C with two different stable carbon targets, ^{12}C and ^{13}C. The experiment was conducted at Argonne National Laboratory using the Argonne Tandem LINAC Accelerator System (ATLAS) to produce the ^{16}C radioactive ion beam (RIB), as described in section 4.2, note: LINAC is short for LINear ACcelerator. Data were collected during three separate experimental campaigns under different conditions, but the results presented here primarily consider the third campaign, when the bulk of the data were collected.

During the first experimental campaign, the ^{16}C+^{12}C fusion cross section was measured for the center-of-mass energy range $E_{C.M.}$ = 16 - 32 MeV. With an incident rate of ^{16}C that was only about 50 particles per second (pps), about 17 hours of data were collected. For the second experimental campaign, in Dec. 2018, the beam rate was much higher with 1,200 particles per second of ^{16}C incident on the detector. The ^{16}C+^{12}C fusion cross section was again measured for center-of-mass energies $E_{C.M.}$ = 8 - 26 MeV. However, due to a campus-wide chilled water system failure, only 10 hours of data were collected during Dec. 2018. For the third experimental campaign, conducted in Feb. 2019, conditions were similar to those in 2018. The ^{16}C+^{12}C fusion cross section was measured with 25 hours of beam-on-target at a rate of 1,200 ^{16}C pps. Additionally, the ^{16}C+^{13}C system was measured for 46 hours with the same incident beam rate.

4.2. Radioactive Ion Beam Production and Identification

ATLAS uses the in-flight production method (described in Ref. [33]) to create Radioactive Ion Beams (RIBs) for experiments requiring the use of short-lived radioactive isotopes, typically with neutron numbers that are only 1-2 neutrons different from a stable isotope. This experiment required a facility such as ATLAS because ^{16}C has a half-life of 0.747 seconds and therefore is only accessible for study as a RIB. Figure 4.1 shows the floor plan of ATLAS, where beam production begins upstream at the left of the schematic and flows

downstream to the experimental halls on the right side. For experiments like this one, the Electron Cyclotron Resonance (ECR) II ion source is where production of the beams begins. The ion source produces low-energy stable ions, which are then accelerated using the linear accelerators, or LINACs. The LINAC modules use radio-frequency (RF) alternating voltages to create the accelerating potential the ions encounter. After acceleration, the primary beam impinges on a target, creating a variety of nuclides. These nuclides are then separated in the RAdioactive Ion SeparatOR (RAISOR), and the desired radioactive species is selected. From there, the radioactive ion beam is directed to the location of the experiment, where it interacts with the experimental target. Our experimental setup was installed in the split-pole spectrograph hall, just in front of the Split-Pole Spectrograph (SPS).

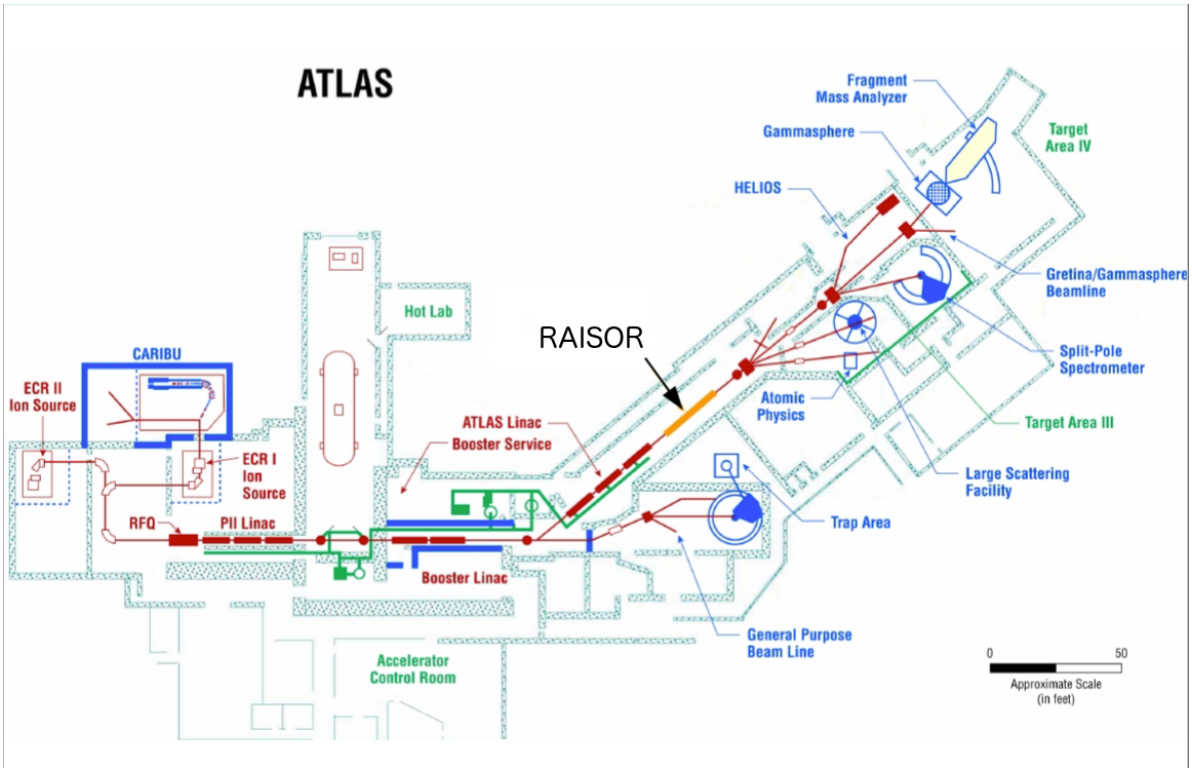

Figure 4.1. The Argonne Tandem Linac Accelerator System (ATLAS) floor plan. Our experiment was conducted in the split-sole spectrometer hall. Image taken from Ref. [34].

To create the ^{16}C beam, a primary beam of ^{18}O was produced by the ECR II ion source and accelerated to an energy of 243 MeV. The ^{18}O beam bombarded a primary target of ^{9}Be with a thickness of 15 mg/cm^2. This target thickness and energy were chosen because

preliminary beam development tests produced the highest intensity of ^{16}C using these parameters. The ^{16}C intensity produced is sufficient to obtain good statistics for fusion at energies above the Coulomb barrier. To produce the ^{16}C, the target induced two-proton removal from the ^{18}O nucleus via the ^{9}Be(^{18}O,^{16}C)2p reaction. Because this is not the only reaction that can occur when ^{18}O is impinged on ^{9}Be, RAISOR was tuned to select for the desired ^{16}C ions.

RAISOR is a magnetic chicane, which is a series of magnets aligned along the beamline that is designed to select specific radioactive species based on their magnetic rigidity. Magnetic rigidity is the product of the magnetic field B and the radius of the circular motion of the particle in that field ρ and is defined as

$$B\rho = \frac{p}{q}. \tag{4.1}$$

It is thus equivalent to the ratio of the momentum p of the particle to its charge q. Figure 4.2 shows a schematic of the layout of RAISOR. The magnets labeled with a Q are quadrupole magnets and are used to spatially focus the ions. The magnets labeled with a M are dipole magnets used to separate different ion species according to their magnetic rigidity. For a given magnetic field, different nuclides have different path radii. There are metal slits positioned at the M and O focal points indicated in Fig. 4.2, which are used to stop the unreacted primary beam and beam contaminants from continuing on to the experimental setup.

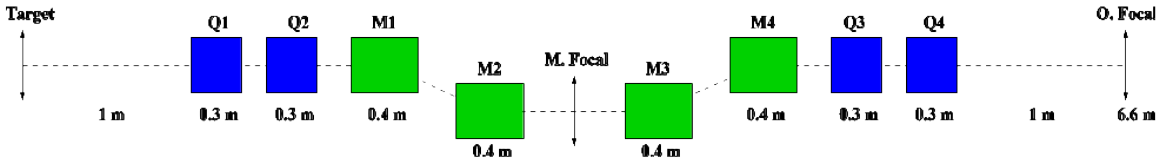

Figure 4.2. Schematic of the RAISOR magnetic chicane taken from Ref. [35]. Q1, Q2, Q3 and Q4 are quadrupole magnets installed surrounding the beamline and are used to spatially focus the beam. M1 and M2 are dipole magnets used to bend the ions around two curves and separate them by magnetic rigidity. There are slits located at the M focal point. M3 and M4 are also dipole magnets used to send the beam back to its original course and there is another group of slits at the O focal point.

A diagnostic tool was placed between the RAISOR exit and the MUSIC detector to assist with beam tuning by identification of the different beam components. This diagnostic comprises two round Silicon Surface Barrier (SSB) detectors placed in the path of the beam. The first detector is thin enough that the ions can pass through it and the energy loss (ΔE) is measured. The second SSB, placed behind the first, is thicker and stops the particles, measuring the residual energy. This detector is a sensitive diagnostic tool because it uses the energy loss of ions in matter to identify nuclides. The stopping power ($S = -\frac{dE}{dx}$) describes the energy loss of an ion as a function of distance traveled. Its value depends on the properties of the penetrating particle and the medium it is moving through. The *Bethe formula* describes the stopping power in terms of these properties and is given by

$$-\frac{dE}{dx} \propto \frac{z_i^2 Z_{medium}}{v^2} NB, \tag{4.2}$$

where z_i is the charge of the incoming particle, Z_{medium} is the proton number of the detector medium, v is the velocity of the incident particle, N is the number density of target particles and B is a factor that depends on velocity. At the energies relevant to this work, any nuclide in the beam will become fully stripped of its electrons once it enters matter, thus z_i can be considered to be proton number, or charge. The silicon telescope differentiates different nuclides by their proton number. It also separates different charge states of the

same nuclide by the difference in energy of the incoming beam. This difference in energy is due to the magnetic rigidity selection in RAISOR, which will accept different charge states with different energy, if their momentum-to-charge ratios are within the accepted range.

A calculation of the spectra expected to be measured by the silicon telescope from the ^{16}C beam production is shown in the top two plots of Fig. 4.3. The top plot shows the energy deposited in the first detector versus the total energy of the ion (i.e. the sum of the energy deposited in both detectors). This shows a clear separation of the RIB of interest, ^{16}C, from other contaminant species that may be present. The middle plot shows a similar diagnostic where the energy deposited in the first detector is plotted against the time-of-flight of the ions. The time-of-flight is generated from the time difference between the RF frequency of the LINAC and the timing signal from the SSB. Finally, the bottom plot shows the predicted magnetic rigidity of the different species that helped determine how to tune the dipole magnets.

Using the relative spacing of the simulated values of magnetic rigidity, the magnetic settings of the dipoles were slowly varied until each nuclide was identified using the silicon telescope. The ^{16}C beam was located and RAISOR was optimized for its transmission. Figure 4.4 shows the ΔE vs. total energy measurement taken after optimization for ^{16}C using the silicon telescope. The most intense group on the plot is that of ^{16}C in the 6^+ charge state. Throughout the experiment, the beam quality was periodically checked using the silicon telescope. A consistent rate of about 1,200 ^{16}C particles per second was observed, with a beam purity of 50%-80% for a current of about 150 pnA primary beam on target. The ^{16}C beam exited RAISOR with a mean energy of about 220 MeV, as measured by the Split-Pole Spectrograph, with corrections for the energy loss in the windows of MUSIC.

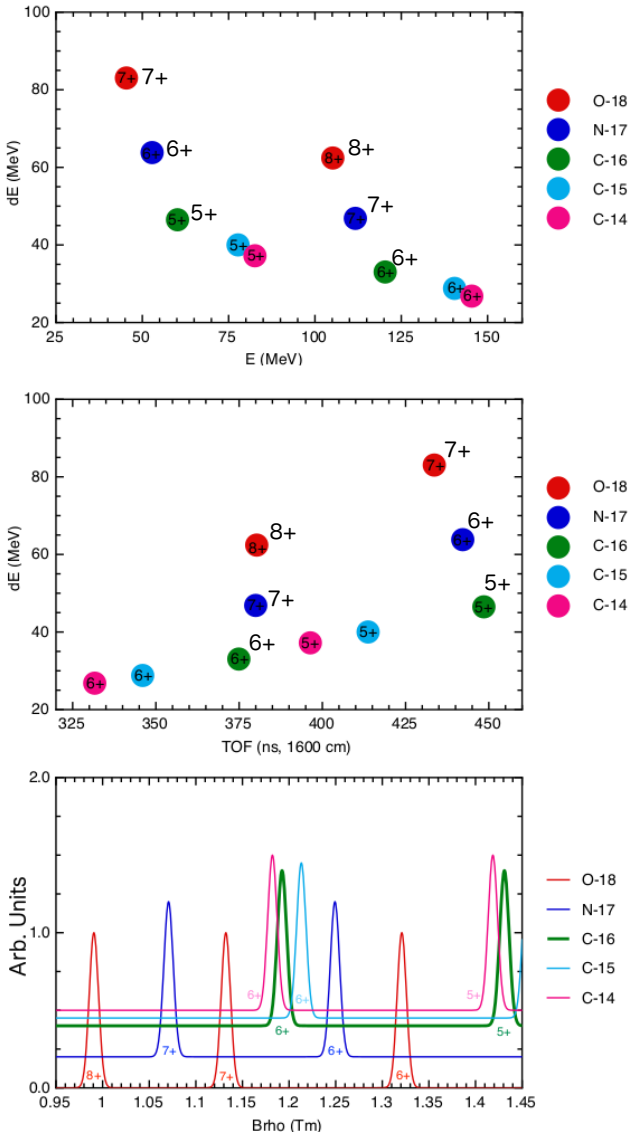

Figure 4.3. The top plot shows the predicted energy deposited in a silicon telescope by different ions exiting the RIB production site. Each isotope is represented by a different color circle and the charge state of each ion is written on its dot. (The charge states have been labeled twice for some points for legibility.) The middle plot shows the ΔE from the thin SSB in the silicon telescope versus the time-of-flight. The bottom plot shows the predicted magnetic rigidities for the different species.

4.3. Experimental Setup Overview

The ^{16}C radioactive ion beam was delivered to the Split-Pole Spectrometer hall of the ATLAS experimental facility. We used four different types of detectors to measure the beam composition, the fusion reactions, and the energy of the incoming beam. As shown in Fig.

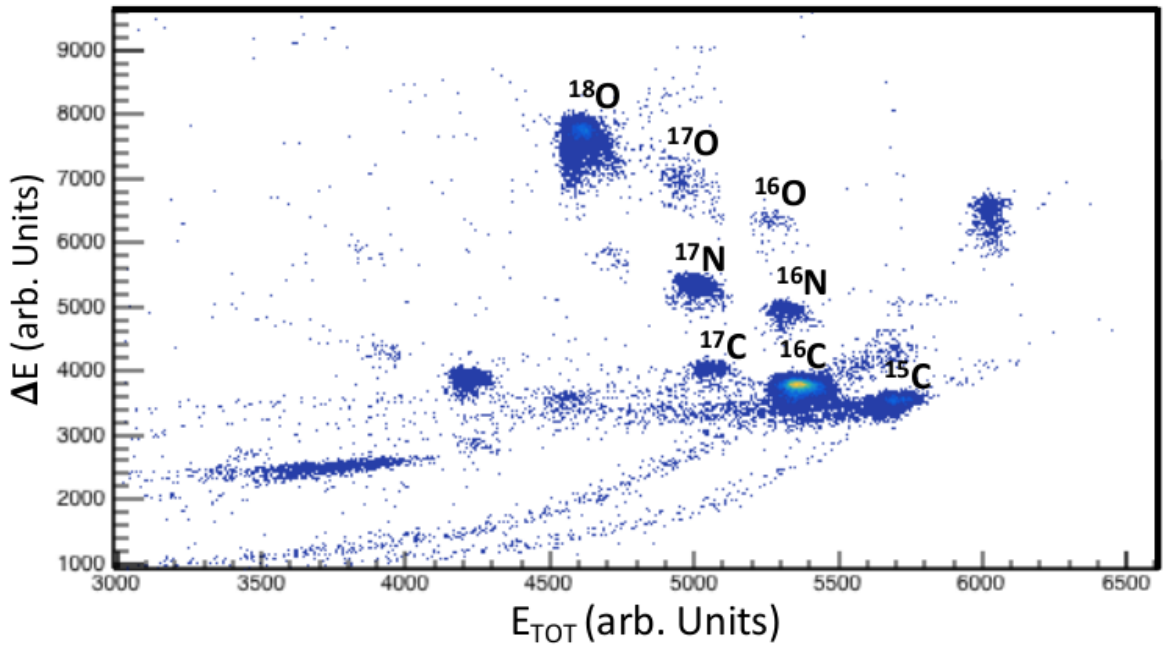

Figure 4.4. The ΔE vs. total energy measured by the silicon telescope located between RAISOR and the detector setup is plotted here. The most intense group is ^{16}C.

4.5, our detectors were arranged such that the incoming beam first encountered the silicon telescope, which was used periodically through the experiment to check the beam quality, but was removed from the beamline for the fusion measurements. When the silicon telescope was removed, the beam first passed through the Parallel-Plate Avalanche Counter (PPAC), which measures the arrival time of each particle and is explained in detail in section 4.4. After passing through the PPAC, the beam encountered the MUlti-Sampling Ionization Chamber (MUSIC). MUSIC is the detector where our fusion reactions occurred and the products were detected, as described in section 4.5. The Enge Split-Pole Spectrograph (SPS), described in section 4.6, was positioned downstream of MUSIC and was used for measurements of the beam energy at several different times during the experiment.

4.4. Parallel-Plate Avalanche Counter (PPAC)

The PPAC was used to measure each particle's time-of-flight, which is important for particle identification as illustrated by the middle plot of Fig. 4.3. The PPAC consists of a chamber containing a small volume of gas and two electrodes. The gas volume is separated

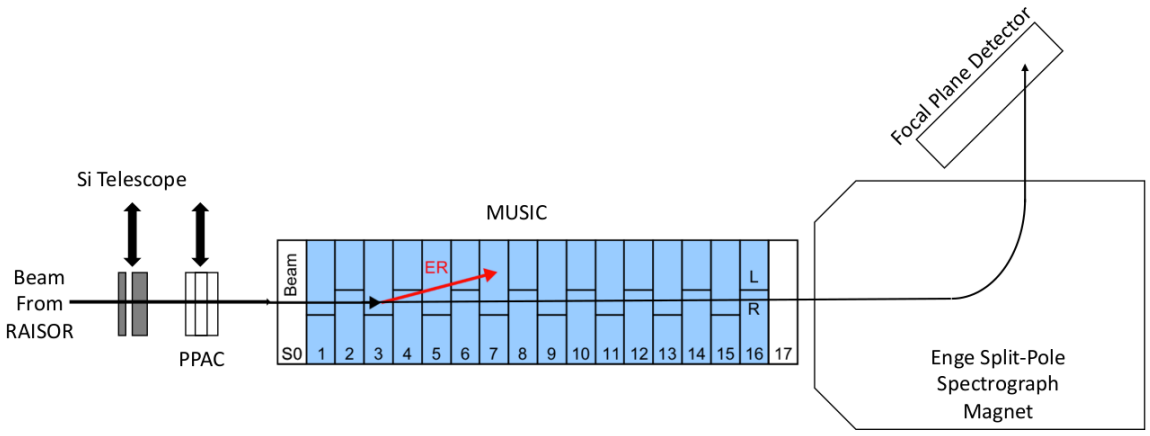

Figure 4.5. A schematic of the arrangement of detectors in the Split-Pole Spectrograph hall is shown here (not to scale). The beam first encountered the silicon telescope, which was removed from the beam path when experimental data were taken. When measuring fusion, the beam went though the PPAC, then into MUSIC. Both the silicon telescope and the PPAC could be removed from the beamline, indicated by the double-sided arrows. The SPS was used for beam energy measurements by momentum analyzing the beam, which was detected by the focal plane detector.

from the beam line vacuum by two thin windows, as shown in Fig. 4.6. Ions travel through the gas volume and ionize the gas between the two electrode foils as they pass. The electrons from the ionized gas are collected onto the anode (positive electrode), and this creates an electric signal that is read by the data acquisition system. This signal gives the time of arrival of individual ions. The time difference between the arrival at the PPAC and the LINAC RF signal was used as a measure of the ion's time-of-flight, which identifies the type of ion. A ^{16}C ion with 220 MeV of energy will only lose $\sim$ 1 MeV of energy as it passes through the PPAC, thus this detector can measure the time-of-flight of a particle while disturbing it very little.

The PPAC has a 0.8" diameter opening through which the ions pass. The entrance and exit windows have Mylar foils that are 0.2 mg/cm^2 thick stretched across them. These windows contain 3 Torr of isobutane gas, which is flowed continuously during the experiment. The electrodes between the windows are made of the same material, and the anode is biased with +480V and the cathode is grounded. The PPAC is mounted on a mobile feedthrough

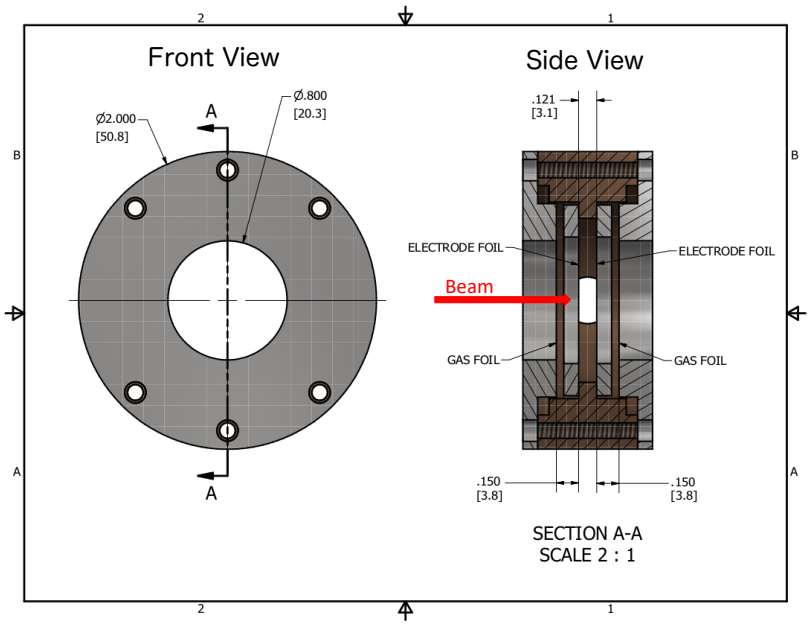

Figure 4.6. Schematic layout of the Parallel Plate Avalanche Counter (PPAC). All dimensions are in inches.

that can move the detector out of the beam path or place it back in, depending on whether the device is needed. Fig. 4.7 shows a photograph of two similar PPAC detectors, one of which was used in our experiment.

4.5. MUlti-Sampling Ionization Chamber (MUSIC)

MUSIC is an active target-detector, meaning that the detection medium also serves as the target for the radioactive ion beam. It was recently used for the first time to measure fusion reactions by Carnelli *et al.* (2015) [10]. It is located in the Split-Pole Spectrometer (SPS) hall to allow for energy calibration measurements using the SPS, which is described in the following section. MUSIC functions well with incident beam rates of up to about 10,000 particles per second, at which point the detector becomes overwhelmed by pileup. With count rates well below 10,000 pps, MUSIC has a 100% detection efficiency for incoming particles.

The MUSIC detector had two Ti windows, 22.1 mg/cm^2 thick, that were mounted at the entrance and exit of the detector to contain the active gas volume. For this experiment, some

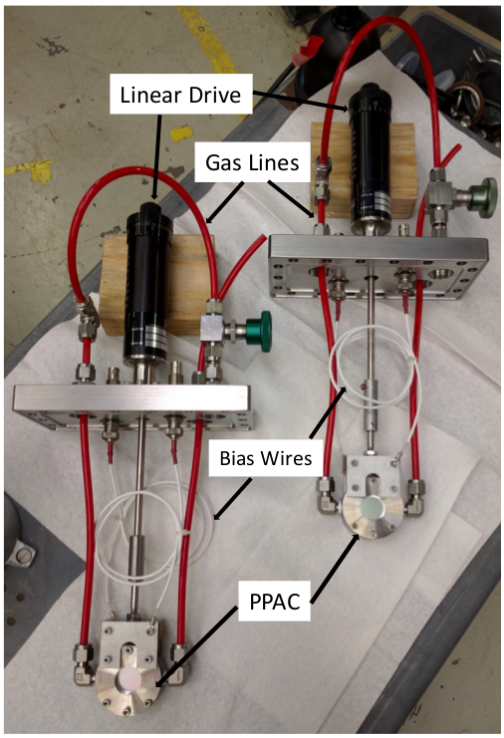

Figure 4.7. Photograph of two PPAC detectors, one of these was used upstream of the MUSIC detector.

data were taken with MUSIC filled with 450 Torr of methane (CH_4) gas, but the majority of the data were taken with 400 Torr of CH_4. For the ^{12}C target, methane of a natural isotopic abundance (99% ^{12}C; 1% ^{13}C) was used and flowed continuously throughout the experiment. For the ^{13}C target, 99.9% enriched $^{13}CH_4$ methane gas at a pressure of 400 Torr was used. The supply of this enriched methane was limited and therefore the gas was not flowed during the ^{16}C+^{13}C measurement.

An aluminum degrader was placed behind the entrance window of MUSIC to lower the energy of the ^{16}C beam. Figure 4.8 shows a photograph of the degrader installed behind the entrance window using one of the screws on the window mount. The energy of the ^{18}O primary beam was 243 MeV, and the energy of ^{16}C arriving at the detection area was around 220 MeV. A degrader thickness of 0.014" (0.36 mm) was chosen in order to lower the ^{16}C energy enough such that the ions would stop within the active volume of the detector. This was done to probe energies close to the Coulomb barrier. The ^{16}C ions lost about 158 MeV

as they passed through the PPAC, entrance window, and degrader combined. The ^{16}C ions then stopped in the last quarter of the active volume of the detector when it was filled with 400 Torr of methane gas.

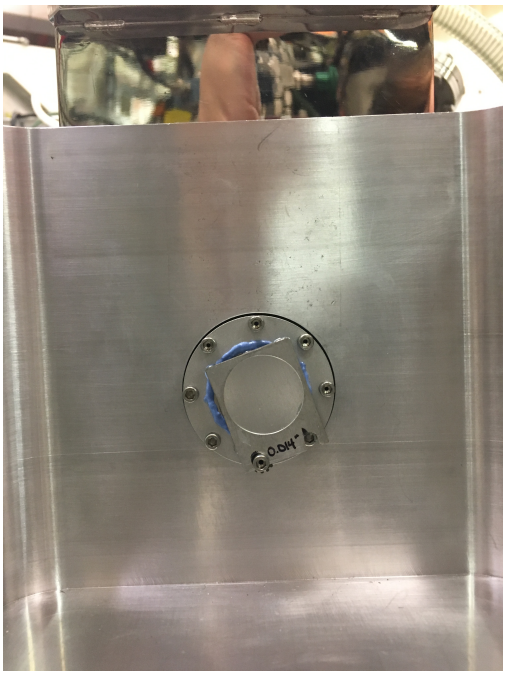

Figure 4.8. The aluminum degrader is mounted on an aluminum frame which is installed behind the music entrance window using one of the screws that holds the window in place. The blue substance is the epoxy used to mount the Titanium window to its aluminum frame.

The non-reacting beam particles lost energy in MUSIC via ionizing interactions with the methane gas. A uniform electric field guides the liberated electrons to the detector anodes. Figure 4.9 shows the configuration of the detector's electric field shaping elements as a cross section along the beam axis. The cathode at the bottom of the detector was biased at -450 V and the anode was grounded. The uniform electric field was supplied by a voltage divider that biased the 12 field-shaping plates and Frish grid such that they had equal potential differences between neighboring plates. The field shaping plates can be seen in the photograph in Fig. 4.10. They are rectangular plates with a rectangular shape cut out of the middle acting as rings of a certain potential determined by their biasing voltage. The Frish grid is made of thin wires mounted to a printed circuit board and is located just above

the final field shaping plate and below the anode. At the top of the detector, a printed circuit board with segmented metal plates mounted on it serves as the anode. The pattern of the anode segmentation is shown in Fig. 4.11. Each of these segments of the anode collected the charge deposited in their respective segments of the detector and were processed separately by the electronics. The signal on the cathode due to the positively charged ionized gas was also read out and recorded by the data acquisition system, as was the signal on the Frish grid.

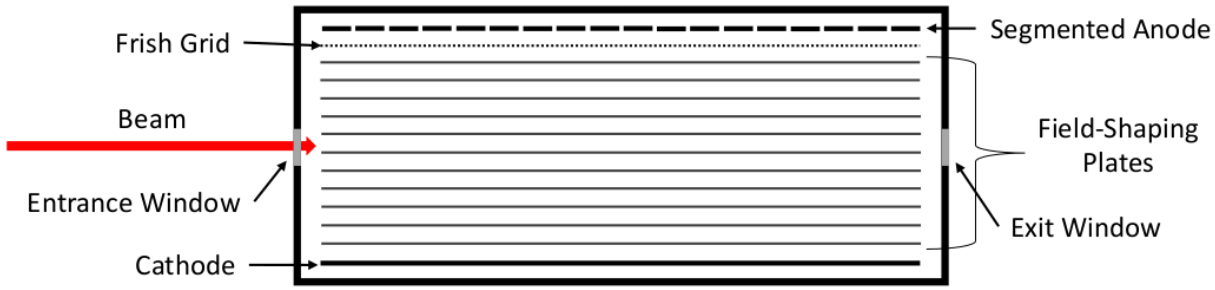

Figure 4.9. Cross section of the internal elements of MUSIC. Ions enter the detector through a window on the left. A voltage divider supplies a smooth electric field from the high negative bias on the cathode to the grounded anodes. The field shaping plates and the Frish grid are also biased by the voltage divider. As ions lose energy in the methane gas, the ionized electrons are collected by the anodes and the cathode detects the positively charged gas molecules.

The multi-sampling design of MUSIC allows for a rough measurement of a particle's trajectory through the detector. As shown in Fig. 4.11, the anode is segmented into 18 strips along the beam axis, each with a depth of 1.58 cm. The first and last strips, numbered 0 and 17, respectively, have a width of 9.0 cm and are not segmented. The middle 16 anode strips, shown in blue, have left and right side segments that are staggered in length. The long strips have length 5.0 cm and short strips have length 4.0 cm. Each anode segment is electrically isolated from the others, which allows one to determine if the particle is traveling along the beam axis or to the left or right of the center.

This experimental setup used analog electronics to amplify, shape, and read the signals from the detectors. All of the left segments of strips 1-16, were first amplified by a Mesytec

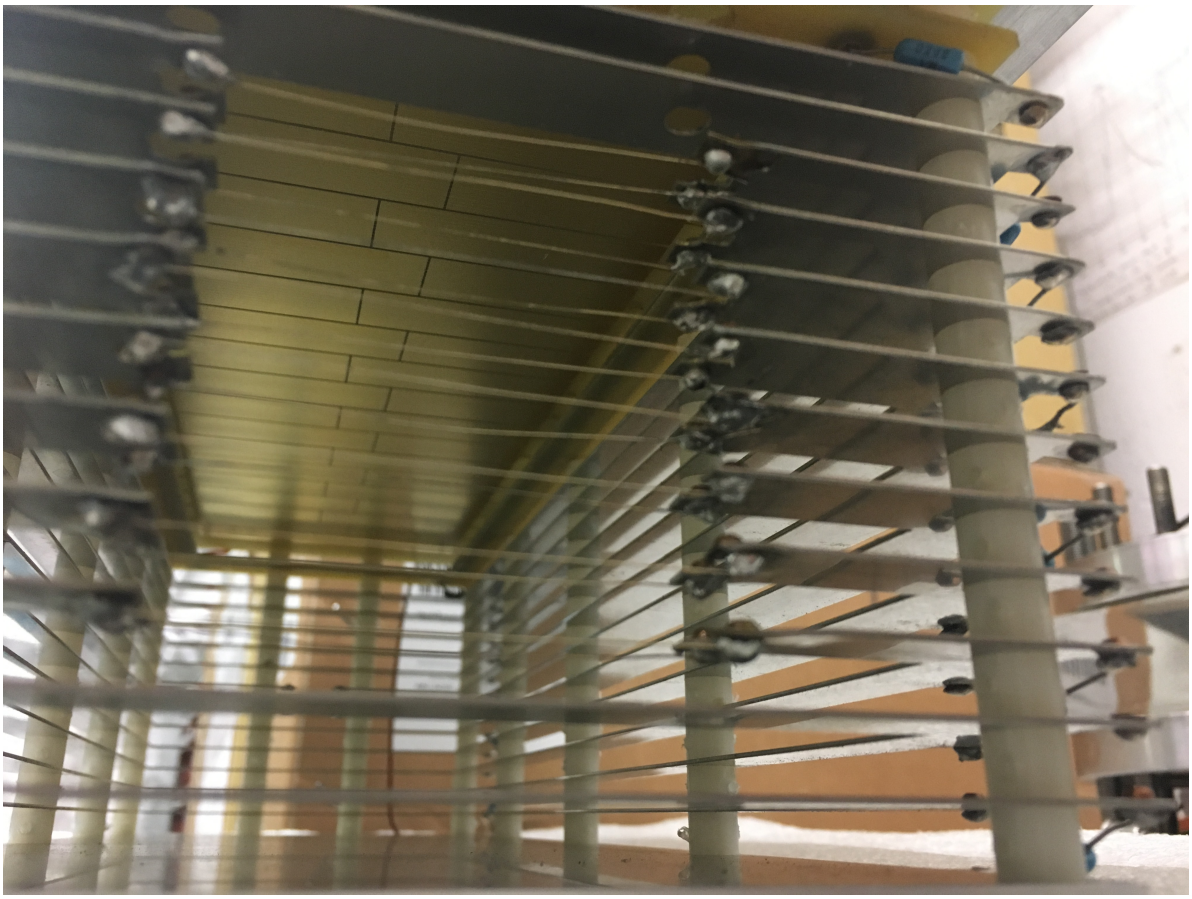

Figure 4.10. Photograph of MUSIC from the downstream direction. The segmented anodes are visible on the top of the detector. The field shaping rings provide a voltage gradient to guide the electrons toward the anodes.

MPR-16 charge-sensitive preamplifier module, which amplifies 16 signals at once. From the preamplifier, these signals were processed by a Mesytec MSCF-16-F shaping amplifier. The signals from the right segments of strips 1-16 were processed with similar modules. The signals from strip 0, strip 17, the Frish grid, and the cathode were each processed separately in similar modules. They were preamplified using Mesytec MPR-1 charge integrating preamplifiers and shaped using ORTEC 571 single-channel shaping amplifiers.

The RF signal from the LINAC and the signal from the PPAC electrode were input to separate Tennelec TC 455 Constant Fraction Discriminators (CFDs). The CFD trigger from the PPAC was then input as the start signal for a Time-to-Amplitude Converter (TAC). The CFD trigger for the RF signal was used as the TAC stop signal. The height of the signal

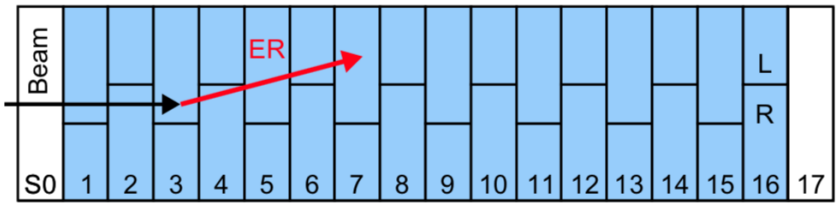

Figure 4.11. The anodes are segmented into 18 strips along the beam axis. The first and last strips (0 & 17) are solid strips and the middle 16 strips are segmented into left and right strips of alternating lengths. The beam is shown entering MUSIC by the black arrow, while the red arrow shows an example trajectory of an evaporation residue (ER). This image has been reproduced from Ref. [10].

output by the TAC was proportional to the amount of time that passed between the start and stop signals and is called the time-of-flight. The signals from the TAC, the MSCF-16-F's, and the ORTEC 571's were acquired by Phillips 7164H Analog-to-Digital Converters (ADCs) which were placed in a CMAC crate and controlled by a Weiner CC32 card. After its amplification, the cathode signal was split and passed into a Tennelec TC 455 CFD as well as the ADC. The CFD trigger output was used to trigger the CMAC control card, alerting the data acquisition to record an event.

4.5. Raw Data Acquired from MUSIC

It is necessary to identify the type of ion associated with each event in the detector to distinguish ^{16}C from other beam contaminants. The size of the signal in each strip of the MUSIC detector is proportional to the energy loss of a particle within the methane gas, and the amount of energy lost in a gas is proportional to the charge of an ion squared, as shown in Eq. 4.2. From the energy lost in the first strip of MUSIC (strip 0), the different nuclides can be differentiated. As mentioned in section 4.2, this quantity must be compared with either the total energy lost or the time-of-flight to provide particle identification. The time-of-flight was acquired using the time difference between the PPAC and LINAC RF. Thus, a plot of the energy lost in strip 0 of MUSIC versus the PPAC time-of-flight, allowed the identification of each incident ^{16}C ion on an event-by-event basis. As shown in Fig. 4.12, there are many different groups representing different ion species. In Fig. 4.4, it is evident that ^{16}C was the

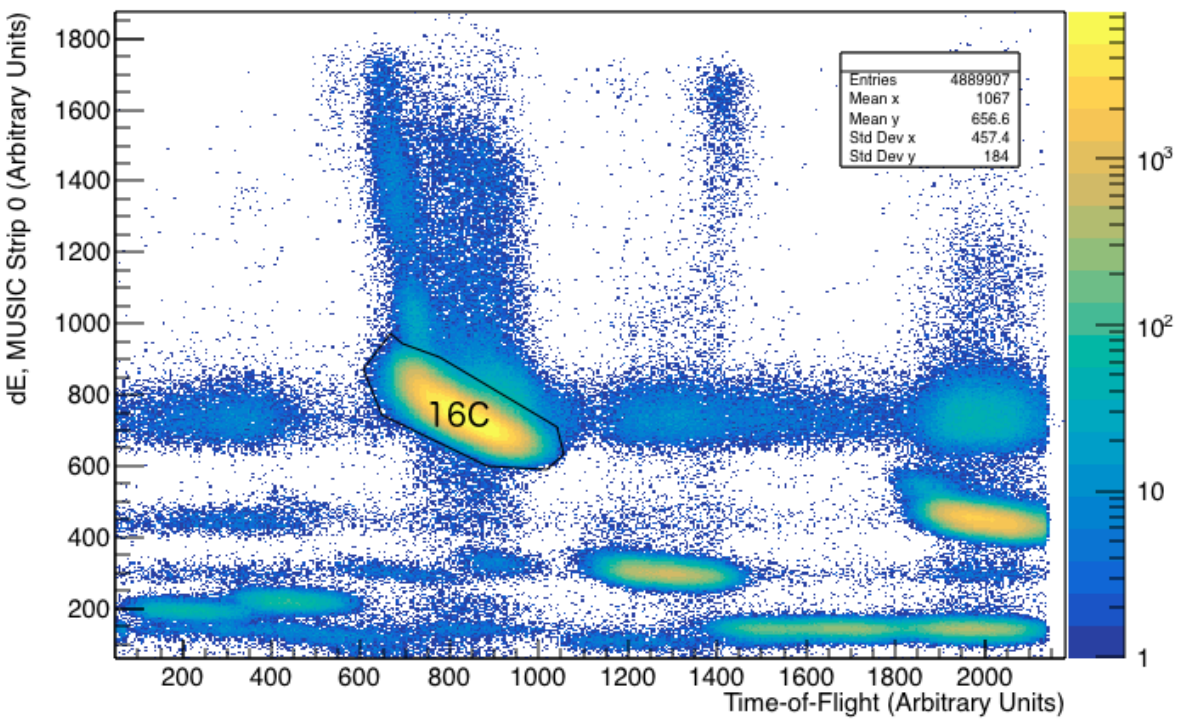

Figure 4.12. Particle identification plot with the energy deposited in the first strip of MUSIC (strip 0) plotted versus the time-of-flight measured by the PPAC. The graphical cut that is applied to the data to select ^{16}C particles is shown.

most intense isotope transported to the MUSIC detector. Energy loss calculations indicate that the oxygen and nitrogen ions are stopped in the aluminum degrader, so none of the groups in Fig. 4.12 include these. These facts indicate that the most intense group in Fig. 4.12 is ^{16}C.

As a particle travels through the active volume of MUSIC, it deposits energy in the gas by ionizing the gas. The ionized electrons, guided by the uniform electric field, are collected on the segment of the anode at the same depth and left or right position. The signals from each anode strip (left + right) plotted against the strip number are called "traces". A centered, non-reacting beam particle will travel down the length of the detector making signals in every other side of the left/right segmented strips as it goes. A representative trace from a centered ^{16}C ion stopping in strip 16 of the detector is shown in Fig. 4.13. The signals

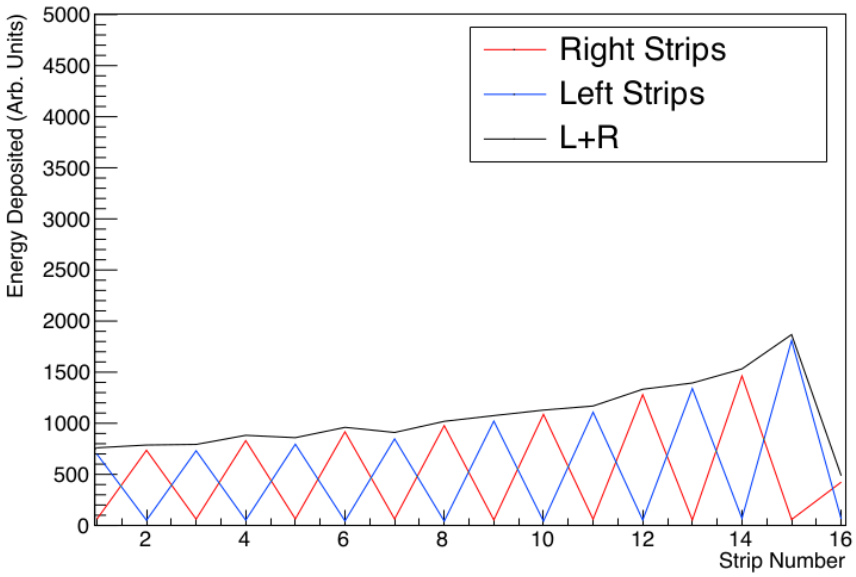

Figure 4.13. This is a beam-like trace in MUSIC where the ion traveled through the center of the detector and stopped in the 16th strip. The red line shows the signals that were seen in the right segment of each strip of the detector and the blue line shows the left-side signals. The black line is the sum of both right and left.

appearing in the left segment of each strip are shown in blue and the right in red. The sum of both is the trace, shown as a black line. When a fusion event occurs, the evaporation residual has an increased proton number and looses more energy in each strip causing it to stop earlier in the detector, according to Eq. 4.2. Because of this increase in proton number, a fusion trace looks like a beam particle until the fusion event happens. In the strip in which the fusion occurs, a sharp increase in energy loss is seen as the residual deposits all of its energy in a short range and stops. A representative fusion trace is shown in Fig. 4.14.

The characteristics of a fusion trace are similar to some elastic scattering events. A function of the left/right divided strips is to distinguish between these two possible event types. The summed left and right signals of an elastic scattering trace can be nearly identical to that of fusion, with the difference that the two separate scattered particles appear in the left and right sides of the detector in the same strip. Figure 4.15 shows such an elastic scattering event. The black line shows a summed trace that is similar to a typical fusion event. However, due to the left/right segmentation of strips 1-16, it is apparent that a particle

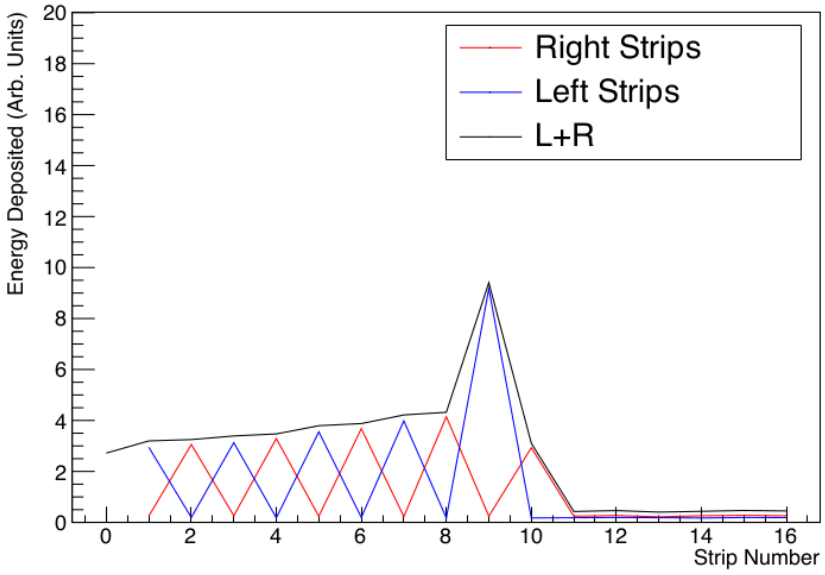

Figure 4.14. A representative fusion trace is shown for a fusion in strip 9. The trace is beam-like until strip 9, then there is an increase in the amount of energy deposited and the particle stops within two strips.

has scattered to the right of the detector at strip 9 and a second particle has continued down the middle of the detector. This is why MUSIC was designed to have anode segmentation in this way.

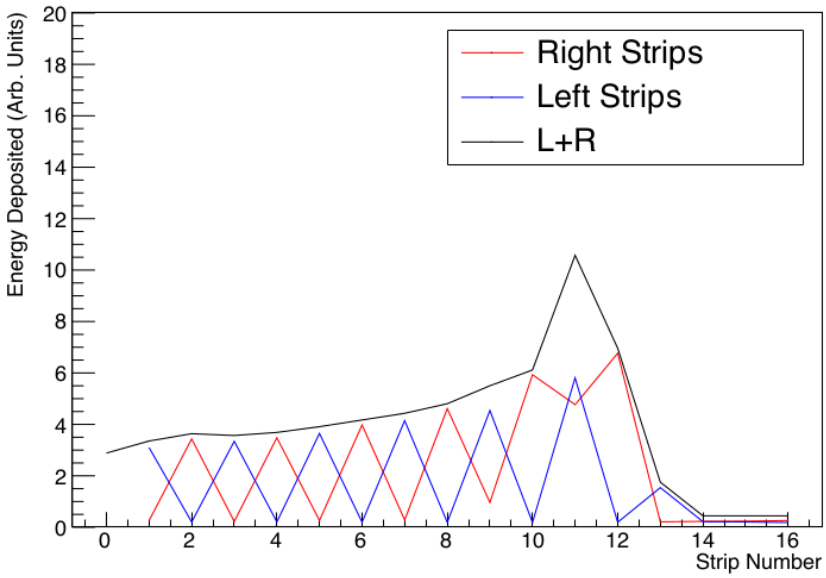

Figure 4.15. This trace is from an elastic scattering event. The trace appears beam-like through strip 8. At strips 9 and 11, a signal is appearing in both sides of the strip. This pattern can be explained by an elastically scattered particle on a rightward trajectory and another on a centered trajectory.

4.6. Enge Split-Pole Spectrograph (SPS)

The energy loss of heavy ions through matter is not well studied and therefore energy loss calculations using programs such as LISE++, see Ref. [36], should be verified by measuring the energy when possible. The SPS was used to determine the mean energy and energy spread of the ^{16}C beam when it exits the aluminum degrader, i.e. the ^{16}C energy when the beam enters the gas volume of MUSIC. To accomplish this, the downstream window of the MUSIC detector was removed, and therefore the detector was at vacuum. The ^{16}C ions therefore pass through the upstream PPAC, the Ti MUSIC entrance window, and the aluminum degrader before detection at the SPS focal plane.

The SPS is a magnet that separates and focuses different ion groups as they pass through magnetic field regions, as described in Ref. [37]. At the focal plane of the SPS, a charged-particle detector is used to distinguish these groups from one another by measuring their positions, or radii of curvature [38]. Using the magnetic rigidity from Eq. 4.1, the momentum

of the particles can be calculated. From there, the energy of the particle is simply

$$E = \frac{p^2}{2m}, \tag{4.3}$$

where p is the momentum of the particle and m is its mass. For our experiment, we utilized this setup to measure the energy of the ^{16}C beam. MUSIC was placed directly in front of the SPS for this purpose.

Figure 4.16 shows a basic diagram of an Enge SPS [39]. The beam enters the magnetic field region from the right and is bent in a circular trajectory. It encounters a field-free drift region, then passes through another magnetic field region and is further bent along a circular path. The beam's position and composition are then measured by the focal plane detector. Figure 4.17 shows a cross-sectional view of the focal plane detector, a position-sensitive PPAC, where the beam is incident from the top of the image. The detector functions much like the PPAC located upstream of MUSIC, except that there are 480 gold-plated tungsten wires that are placed between the cathode and anode foils of the detector. The wires closest to an incident particle collect electrons from the gas ionized by the particle, indicating where the ion has entered the detector, thus measuring position. The pressure foils surrounding the electrode foils hold 5 Torr of isobutane gas that is flowed. The two electrode foils are biased with +280 V and -280 V, respectively.

The position sensitive PPAC on the focal plane detector operates on a separate data acquisition system from the upstream PPAC and MUSIC detectors. The anode foil signal is amplified using fast amplifiers. It is then sent to a CFD to create the start signal for a CAMAC Time to Digital Converter (TDC). The signals from the position-sensing wires are sent through integrated delay line circuits with a fixed 2 ns delay per wire and provide the stop signal for this module. The amount of time that passes between the start and stop signals in the TDC is then used to determine which wires the signal came from, or the position of the particle along the focal plane.

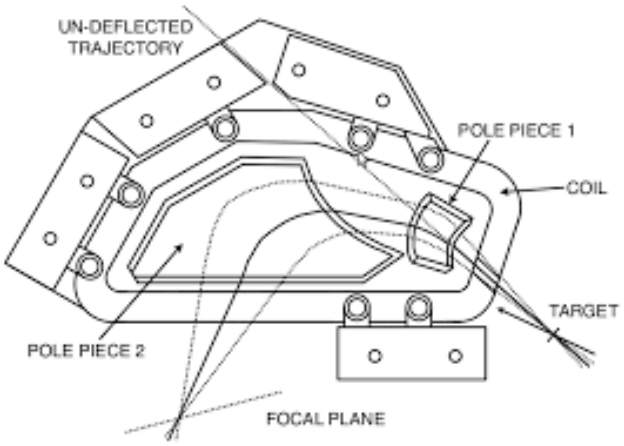

Figure 4.16. The Split-Pole Spectrograph (SPS) is shown here. The split-pole magnet bends ions according to their magnetic rigidity and a detector located at the focal plane measures where each species exits the magnet. This image is adapted from Ref. [40]

Figure 4.17. This is the cross-section of the position-sensitive PPAC located at the focal plane of the SPS. The beam is incident on the detector from the top of the image. This image is reproduced from Ref. [38].

To calibrate the SPS, a ^{228}Th source was placed upstream of the magnet and the emitted alpha particles were detected in the position-sensitive PPAC detector. The decay chain of ^{228}Th emits alpha particles of 7 different energies, 5 of which were detected in the focal plane detector. The energies corresponding to each peak, from left to right are 5.34 MeV, 5.42 MeV, 5.69 MeV, 6.05 MeV, and 6.29 MeV. With the magnetic field setting specified and the known energy, mass, and charge of the alpha particles, a conversion from the arbitrary units of channels in the focal plane detector position spectrum to the radius of curvature ρ was determined to be

$$\rho = \frac{51.465 + 0.010143 \times y}{100} m. \tag{4.4}$$

In this equation, y represents the value in channels of some position in the focal plane detector. The value of ρ is given in units of meters.

As shown in Eq. 4.1, the ratio of the momentum to the charge of an ion is equal to the magnetic field strength times the radius of curvature of the particle for a charged particle moving in a magnetic field. Thus, to determine the energy of ^{16}C, the SPS magnetic field was adjusted to focus the ^{16}C onto the focal plane detector. To identify carbon in the SPS, calculations of the energy lost by ^{16}C traveling through the MUSIC entrance window and degrader were used to predict the magnetic field that would curve those ions into the focal plane detector. From this starting value, the magnetic field setting was slowly adjusted until the ^{16}C beam was seen in the focal plane detector. Then, the position-sensitive PPAC was used to measure the magnetic rigidity of the ^{16}C beam. By using Eq. 4.1 and Eq. 4.3, and accounting for unit conversions, the relationship between the energy of the beam and the known quantities measured by the SPS focal plane detector is given by

$$E = 44937.759 \times \frac{(qB\rho)^2}{m} MeV. \tag{4.5}$$

The energy of the beam is given in MeV if q is specified in units of electron charge (e), B is given in Tesla, m is in units of MeV/c^2, and ρ is in meters, calculated by Eq. 4.4.

Chapter 5. Analysis

The goal of this experiment is to obtain total fusion cross sections at a range of energies for two systems of interest: ^{16}C+^{12}C and ^{16}C+^{13}C. The cross section as a function of energy, $\sigma(E)$, is given in units of cm^2 by the equation

$$\sigma(E) = \frac{N_f(E)}{N_i \times \frac{N_t}{cm^2}} \times \frac{1}{\epsilon}. \tag{5.1}$$

Here, $N_f(E)$ is the number of fusions found in a given energy range and N_i is the number of particles incident upon the target. The term $\frac{N_t}{cm^2}$ is found by multiplying the gas target's particle density (in units of $\frac{molecules}{cm^3}$) by the depth of the target for that energy bin. Finally, the cross section is corrected for the efficiency of fusion identification, ϵ. Thus, the determination of the cross section requires identifying which events are fusion and at which center-of-mass energy these fusions occurred. The number of fusion events is then normalized to the number of ^{16}C beam particles incident on the detector and the target's areal density. This chapter describes how these quantities were obtained in the analysis and presents how they were used to obtain the final cross sections.

5.1. Calibrating MUSIC Data

The identification of fusion events in MUSIC requires characterization of the shape of fusion traces recorded by the detector. All of the signals from the left segments of strips 1-16 are processed by a single multi-channel preamplifier and a signal-shaping electronics module. The right strip segments have similar modules processing their signals. It is well known that different channels in the same preamplifier can have different gains from one another. This fact means that the raw data have variations in signal amplitude from one channel to another. Fusion events occurring near the stopping point of the beam result in signals that are only slightly higher than the Bragg peak and are therefore difficult to distinguish. This is one reason why it is essential to calibrate for the strip-to-strip variations due to the electronics. Pulser calibrations show the different responses of each channel in

the electronics for the same signal input. These are important for identifying what value in the raw data corresponds to a zero input, since there is always a small offset from zero due to the operation of the processing electronics. Additionally, calibrations must be done with the detector when it is fully operational (i.e. with gas, biased, and signals from the beam) to account for effects that are introduced by inefficiencies in charge collection.

Over the course of the experiment, the electronics in MUSIC experiences some drift in gain that must be adjusted before calibrations are done. To account for this drift, three different calibrations were performed to align strip 0, the left segments of the anode, and the right segments of the anode. For each hour of data, a gaussian function was fit to all of the events in strip 0, in the strip 3 left segment (the long one), and the strip 4 right segment (the long one). The centroid of these fits was used to line up strip 0, all of the left strip segments, and all of the right strip segments, respectively, to the same centroid for the first hour of data. This was done using a multiplicative factor, f, according to the equation $\text{run}_1 = \text{f}_x \times \text{run}_x$.

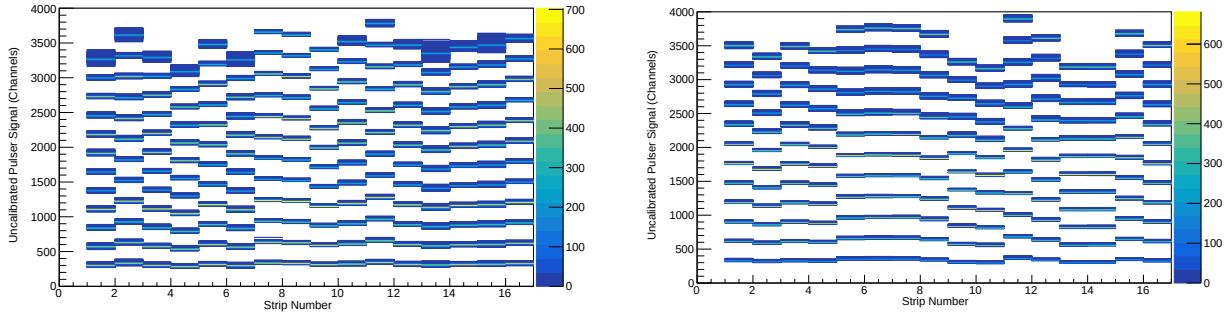

(a) (b)

Figure 5.1. The raw data collected from the pulser test of the detector electronics for strips 1-16 for the left (a) and right (b) segments. The input pulses range in voltage from 0.005V - 0.060V in steps of 0.005V.

Pulser calibration data were taken for the left and right segments of MUSIC strips 1-16 in May 2019, a few months after the experimental run in February 2019. An electronic pulse signal generator was input into the two Mesytec MPR-16 preamplifiers that process the left and right segments of MUSIC strips 1-16. The height of the electric pulse was adjusted to

12 different voltages, ranging from 0.005V to 0.060V in steps of 0.005V. Figure 5.1 shows the pulser data collected by the DAQ after it was input into the preamplifiers and further processed by the shaping amplifiers. Figure 5.1a shows the 16 channels used to process the left segments of strips 1-16 with the right segment pulser results in Fig. 5.1b. The y-axis shows the recorded signals and is plotted in arbitrary units, which are produced by the data acquisition system as it converts pulse height to a digital numerical value. For each electronics channel (i.e. strip segment), Gaussian functions were fit to the signals collected at each voltage. The centroid of the fit was taken to be the value, in arbitrary units, produced by that voltage input into that preamplifier channel. The true value of a zero-input is nonzero when the data acquisition converts it to arbitrary units. For each channel, to find the value in arbitrary units which corresponds to a zero-voltage input, a plot of the Gaussian centroids of the fits to all the pulser signal peaks versus the applied voltage is fit to a linear equation, as shown in Fig. 5.2. The y-intercept of the fit to this data identifies the zero point in arbitrary units. This pulser data characterizes how the electronics respond to signals of different voltage, but it is not sufficient to use only this as a characterization of the detector. For example, one cannot accurately use this voltage calibration to identify how much energy is deposited in each strip relative to the others. This is because the process of the energy loss in the gas and charge collection onto the anode strips is not 100% efficient and therefore a calibration must also be done using MUSIC in its full operating mode with beam.

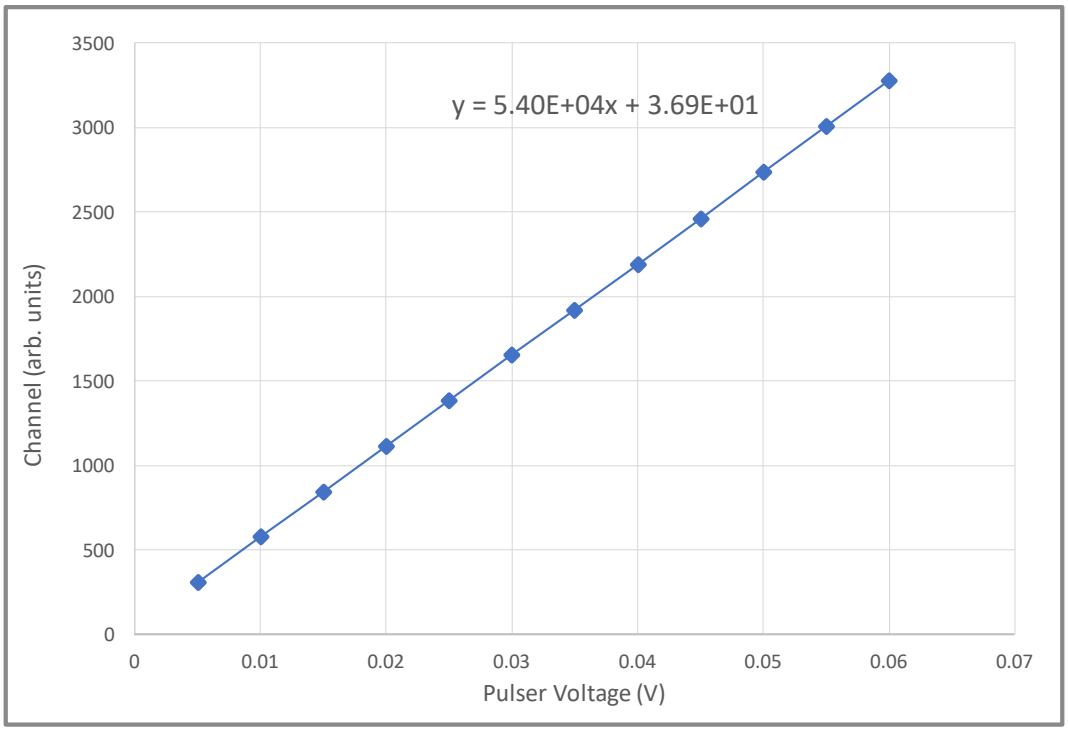

Figure 5.2. The signals from Fig. 5.1 for the left segment of strip 1 are plotted versus the applied pulser voltage. The equation for the linear fit to the data is displayed on the plot. The vertical error bars (statistical uncertanties) are smaller than the symbols representing the data points.

To calibrate the data using the full functional response of the detector when it is filled with gas and biased, each individual channel must be independently calibrated, including the short left or right segments of each strip. As the beam passes through the MUSIC window and degrader, significant angular straggling is introduced. Some particles are deflected far enough to the right or left that they are entirely detected by the strip segments on that side, while producing no signals on the other side, e.g. the event shown in Fig. 5.3. A subset of these events with similar shape and penetration depth in the detector was selected because this indicates that they have similar incoming energies and can be calibrated to an idealized event. Traces that stop in strip 14 were selected because this is the furthest depth into the detector that has a statistically significant number of deflected particles detected that have the same qualitative shapes. All of the traces meeting these criteria that only produce signals in the left segments of each strip are plotted together in Fig. 5.4a. Similarly, Fig.

5.4b shows the traces meeting the same requirements that only produce signals in the right segments of each strip. The value of the uncalibrated signal size in each strip was found by producing a histogram of the signal size in each strip, fitting it with a gaussian function, and taking the centroid.

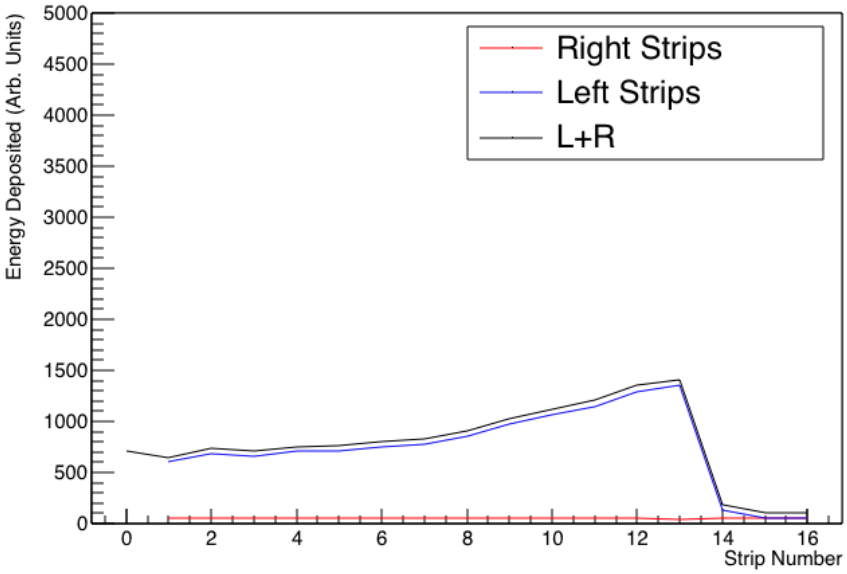

Figure 5.3. One of the traces used to normalize the left side of the detector.

The measured signal size is calibrated to energy deposited using an idealized beam particle's trace that was simulated with LISE++ (see Ref. [36]) using energy losses in layers of 400 Torr of methane gas corresponding to the depth of the strips in MUSIC, and is shown in Fig. 5.5. This trace was generated assuming that the energy of ^{16}C entering strip 0 of MUSIC is E_{lab} = 56.55 MeV, and the particle is traveling straight in the gas. This energy was selected because it produced a trace that was similar to those in Fig. 5.4, which stopped in strip 14 and had the same relative energy loss in strips 13 and 14. The difference in energy loss between an ion traveling in a straight line into the gas and an ion deflected at angles such as those of the ions in Fig. 5.4 is less than 2% and is therefore negligible.

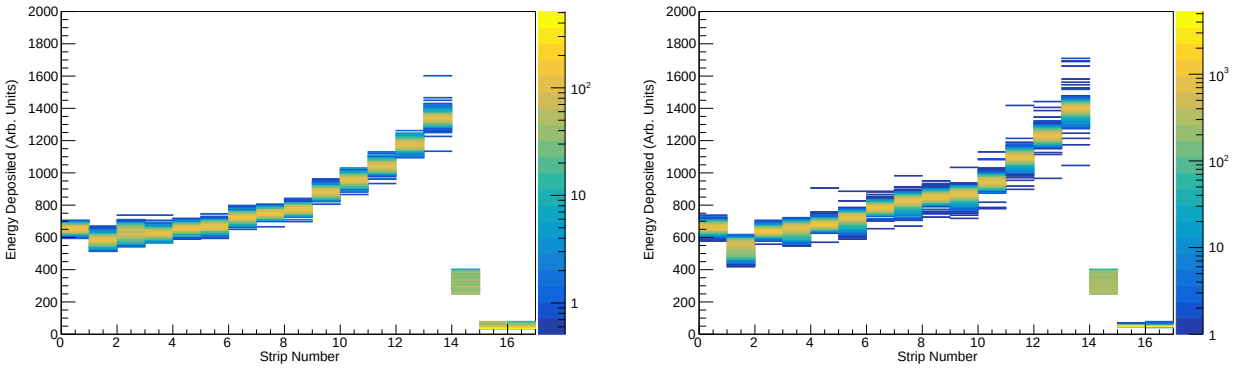

(a) (b)

Figure 5.4. Plot (a) shows a group of traces with similar shape, and therefore similar energy, that appears in the left strip segments only. The y-axis shows raw, uncalibrated energy deposited in the left segment of strips 1-16, with the strip number plotted on the x-axis. The uncalibrated values from strip 0 (not left/right segmented) are also plotted for these events. Plot (b) shows a similar plot for right-aligned events, where the y-axis is the raw signals of the right segments of each strip.

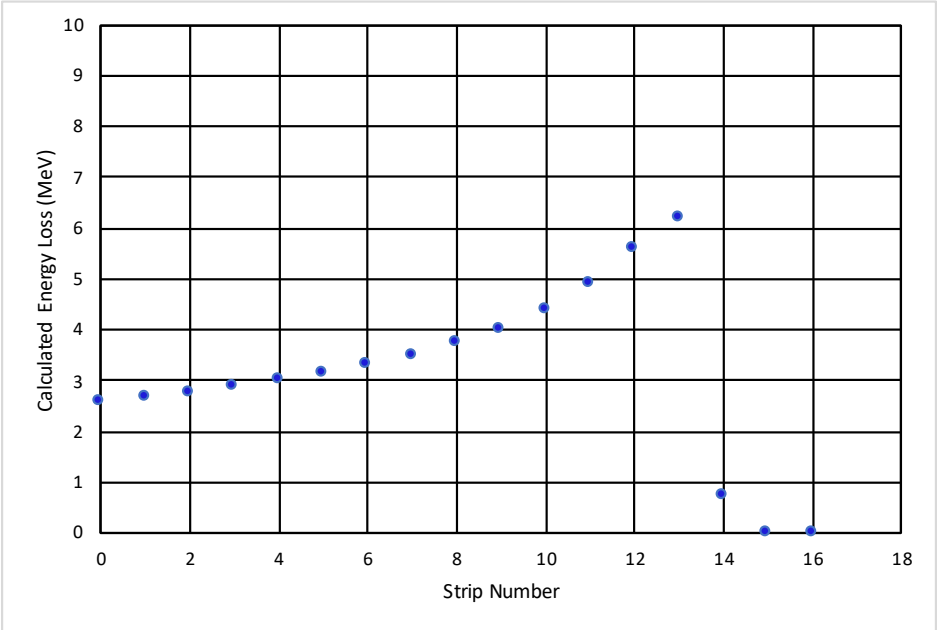

Figure 5.5. The LISE++ predicted energy loss of a single ^{16}C beam particle moving through layers of 400 Torr of CH_4 that are the same depth as a strip in MUSIC is plotted versus strip number. The particle enters strip 0 with energy 56.55 MeV. See the text for details.

The signal values in each strip are aligned with the simulated curve using the equation

$$y_{aligned} = \frac{y_s}{y_m - z_0} \times y_{unaligned}, \tag{5.2}$$

where y_s is the simulated energy loss predicted by LISE++, y_m is the mean of the gaussian fit to the y-axis values from Fig. 5.4, and z_0 is the zero offset determined using the pulser calibrations. The multiplicative factor, $\frac{y_s}{y_m - z_0}$, is uniquely determined for each segment of each strip, except strips 14-16. Because the signal is small or zero in these strips, the same calibration cannot be done. The multiplicative factor used for these strips is the average of the multiplicative factors for strips 1-13. There was no pulser data taken for strip 0 of the detector, so the same multiplicative factor applied to strips 14-16 is used to align it. The same events from Fig. 5.4 are shown in Fig. 5.6 with the calibration applied.

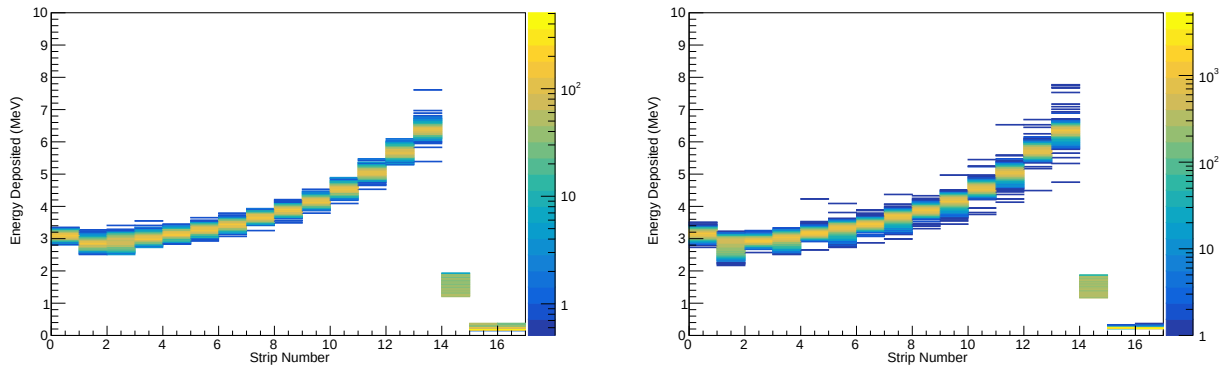

(a) (b)

Figure 5.6. The same events shown in Fig. 5.4 are presented here after normalization to the energy loss predicted by LISE++ in Fig 5.5. The events that are off axis to the left are shown in plot (a) and those to the right are in (b).

5.2. ^{16}C+^{13}C: Additional Calibration

Due to the limited supply and expense of enriched $^{13}CH_4$, once the volume of MUSIC was filled to 400 Torr pressure, all gas valves were shut and that same volume of gas was used for the duration of the ^{16}C+^{13}C data collection. A lowering of the gain was observed over time as the signal outputs drifted downward. Figure 5.7a shows the first hour of data

taken with the enriched methane compared with the final (46th) hour of data taken in Fig. 5.7b. The drift downward in energy deposited in strip 0 is about 25% over the course of this data collection. A similar drift was seen in all channels of the detector, indicating that this issue was not isolated to a single electronics channel. For comparison, with the natural methane flowing in the detector, the variation was under 3% over a similar amount of time and was most likely due to drift in the electronics. The y-axes are plotted on the same scale and the downward drift of the signal size is apparent. There are a few factors that could affect the detector in this way, including a change in pressure or gas degeneration, e.g. by oxygen contamination.

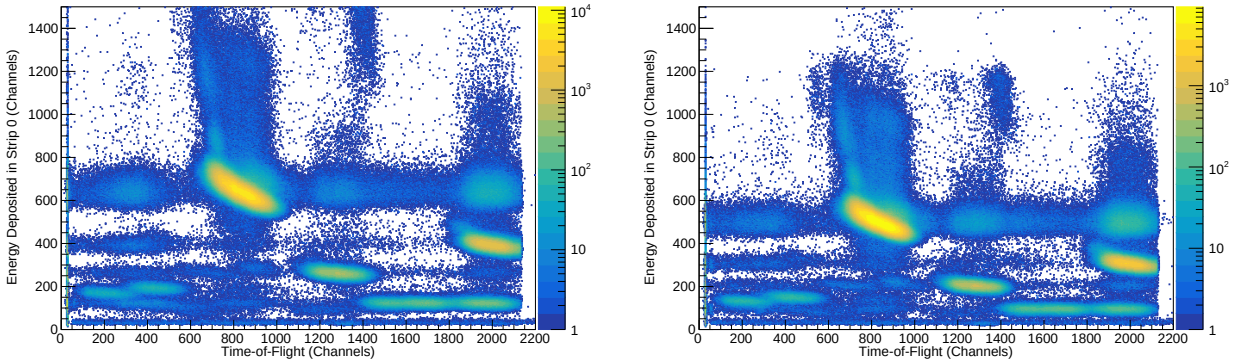

(a) (b)

Figure 5.7. Particle identification spectra with energy deposited in strip 0 plotted versus time-of-flight. The first (a) and last (b) experimental runs with the enriched methane are shown. The ^{16}C group is centered around channel 650 on the y-axis for the first run and around channel 500 for the last run.

To check if this drift was the result of a change in pressure, the stopping profiles of the beam for the first and last hours of data taken with $^{13}CH_4$ were compared. These stopping profiles are shown in Fig. 5.8. The mean strip number and spread of the distributions are in agreement between the two runs. Thus, the beam is reaching the same point in the detector through the 46 hours of data collection, which means the pressure did not change significantly enough to affect this. The downward drift in gain is thus likely caused by gas degeneration.

Due to its strong electronegativity, even a small amount of oxygen from outgassing or small leaks into the chamber from the atmosphere could have this effect.

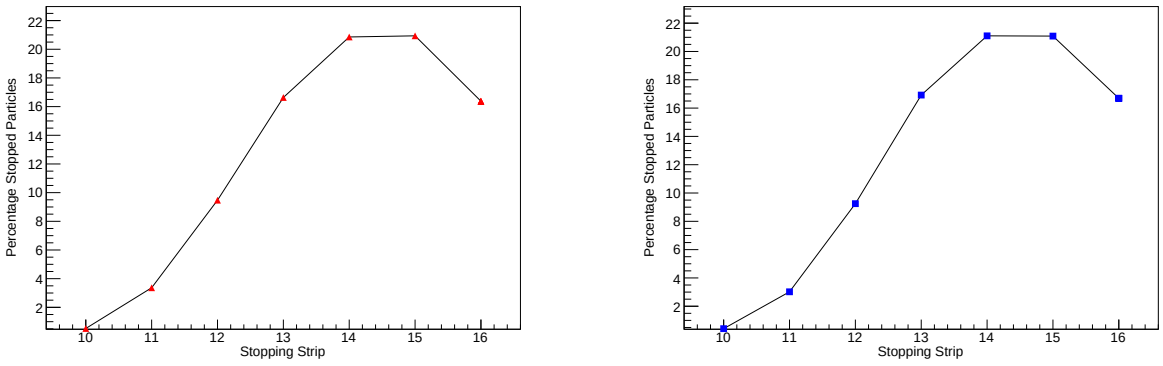

(a) (b)

Figure 5.8. The percent of particles stopped in each strip versus the strip number is plotted for the first (a) and last (b) runs with the enriched methane. A Gaussian fit to the first run has a mean value of 14.51 ± 0.04 with a standard deviation of 1.90 ± 0.05. For the last run, these values are 14.53 ± 0.05 and 1.88 ± 0.06, respectively. These mean values and spreads are in agreement.

Each hour of ^{16}C+^{13}C data was aligned to the first hour the same way the alignment is done in the rest of the data to account for electronics drift. Strip 0, the left anode segments, and the right segments are lined up using the mean of a Gaussian fit to strip zero, the third left segment and the fourth right segment for each hour. This is simply a more drastic alignment because of this severe drift downward in gain. After this alignment was performed for all of the ^{16}C+^{13}C data, the same calibrations described in section 5.2 were applied to the data.

5.3. Energy Calibration

It is necessary to determine the mean energy and spread in energy of the ^{16}C particles entering the active volume of MUSIC to identify the energy at which the fusion events occur. Over the course of this experiment, various energy measurements were taken and energy loss calculations were used to predict energy when measurements could not be made. The measurements and calculated energies are compiled in Table 5.1. This table is organized

by groups of measured quantities, followed by the quantities calculated using these measured values. The bottom row of each segment in the table, indicated by a double horizontal line, gives a prediction or measurement of the energy of the beam after the degrader in MUSIC (i.e. the energy of ^{16}C entering the gas volume of the detector). The rest of this section explains in detail how each of these numbers was obtained.

Table 5.1. Measured and calculated ^{16}C beam energies obtained using various methods.

	Beam Species	Date	Energy (MeV)	Uncertainty (MeV)	Degrader Material	Measurement Type
1	^{16}C	2018	180.90	0.03	entrance & exit windows	SPS
2	^{16}C	2018	219.8		none	LISE++, input: row 1
3	^{16}C	2018	63.7		PPAC, entrance window, degrader	LISE++, input: row 2
4	^{16}C	2018	61.5	0.1	PPAC, entrance window, degrader	SPS
5	^{16}C	2019	218.9		none	bending magnet scaling, row 2
6	^{16}C	2019	61.5		PPAC, entrance window, degrader	LISE++, input: row 6

Note: The uncertainty in the LISE++ calculations is on the order of 10%. See the text for more details.

A measurement of the energy of the ^{16}C beam after it passed through only the entrance and exit windows of MUSIC with no gas was taken in 2018 using the SPS. The mean value of a Gaussian fit to this data was 180.9 MeV (row 1 of Table 5.1). The primary purpose of this measurement was to determine what thickness of degrader to add to the detector. An Al degrader thickness of 0.014" (0.36mm) was chosen because energy-loss calculations with LISE++, using the measured energy 180.9 MeV as input, predicted that this degrader

thickness would cause the average beam particle to stop at strip 14 in the detector. These LISE++ energy-loss predictions were carried out in the following way. The energy loss in the two Ti windows of thickness 22.1 $\frac{mg}{cm^2}$ resulting in an energy of 180.9 MeV was calculated. Adding this energy loss to 180.9 MeV, the mean energy of the beam before it interacts with the experimental setup is calculated to be 219.8 MeV (row 2 of Table 5.1). Next, starting with a ^{16}C energy of 219.8 MeV, the energy loss in the PPAC, entrance window, and degrader was calculated. This yields a final energy of 63.7 MeV for the mean ^{16}C beam particle after the degrader as it enters the gas volume of MUSIC (row 3 of Table 5.1). Predicted energies found with LISE++ are known to be within 10% of measured values, thus the error on these calculations is under 10%.

To confirm that the actual energy loss in the PPAC, window, and degrader is close to the predicted value, another measurement was taken of the beam's energy using the SPS. For this measurement, the degrader was installed, and the MUSIC exit window removed. The energy measurement in the SPS was thus taken for beam that had passed through the PPAC, the MUSIC entrance window, and the degrader. The measured energy distribution of the ^{16}C beam at the entrance of the gas volume of MUSIC, as measured using the SPS, is shown in Fig. 5.9. A Gaussian fit to these data has a mean value of 61.5 MeV $\pm$ 0.1 MeV and a full-width at half maximum of 13.2 MeV (row 4 of Table 5.1). Comparing this 61.5 MeV value with the LISE++ predicted energy of 63.7 MeV, there is a difference of just 2.2MeV out of $\sim$ 150 MeV energy loss between them, about a 1.4% difference. These values are well within the expected accuracy for LISE++ predictions. The difference of 2.2 MeV is also small compared with the measured spread in energy of the beam. The Gaussian fit in Fig. 5.9 has a standard deviation of 5.4 MeV, and the range of energies probed by each strip ranges from 3 MeV in earlier strips to 5 MeV in later strips.

The focal plane detector in the SPS developed a gas leak between the December 2018 and February 2019 experimental campaigns. It was not possible to repair this before for the 2019 experiment, thus a measurement of the energy of the ^{16}C beam was unable to be made

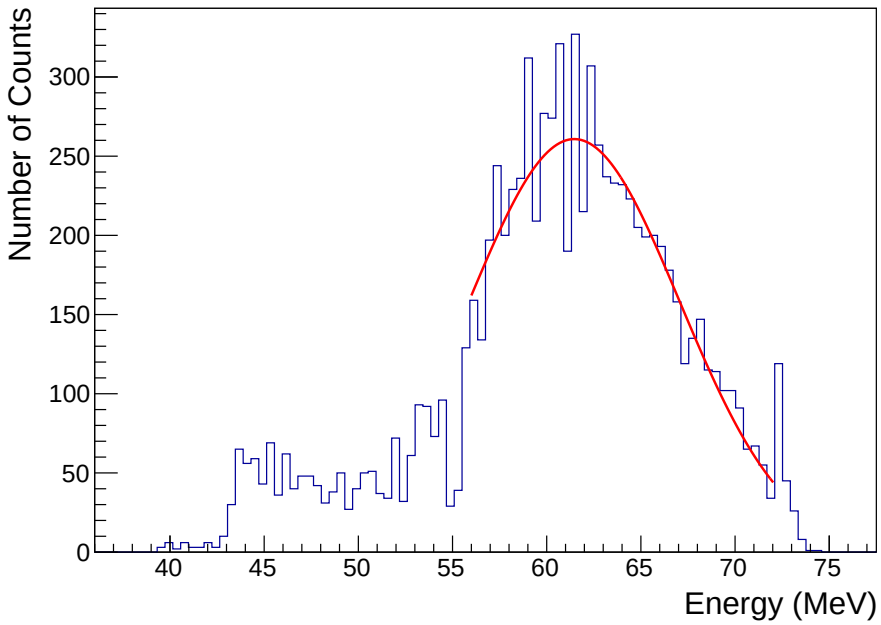

Figure 5.9. The energy distribution measured in December 2018 in the focal plane detector of the SPS. The dip in counts at 55 MeV is unphysical and results from the software that combines the low and high energy sides of the detector together in the plot with an offset. The gaussian fit to the data is shown as a red line with a mean value of 61.5 MeV and a standard deviation of 5.4 MeV. It has been fit to a restricted range to obtain a better fit that is not affected by the artificial gap or edge effects of the detector.

in 2019. Some elements in RAISOR and other beam tuning elements likely had slightly different settings between the 2018 and 2019 campaigns resulting in ^{16}C beams of slightly different energies. This effect can be seen by the fact that the range of the ^{16}C beam in the methane gas is different for each experimental campaign. Figure 5.10 shows the stopping profiles of the ^{16}C beam from December 2018, plot (a), and February 2019, plot (b). These plots show the percentage of the total beam particles that stop in each strip versus the strip number. In the 2019 data, the mean stopping location for ^{16}C within the detector is 0.8 strips closer to the entrance than the 2018 data, meaning that the energy of the beam was slightly lower in 2019.

These stopping distributions provide another approach to determining the energy of the beam after it exits the degrader using LISE++ and the range in gas, rather than energy loss in the PPAC, window and degrader. The mean value of a Gaussian fit to the plot in Fig.

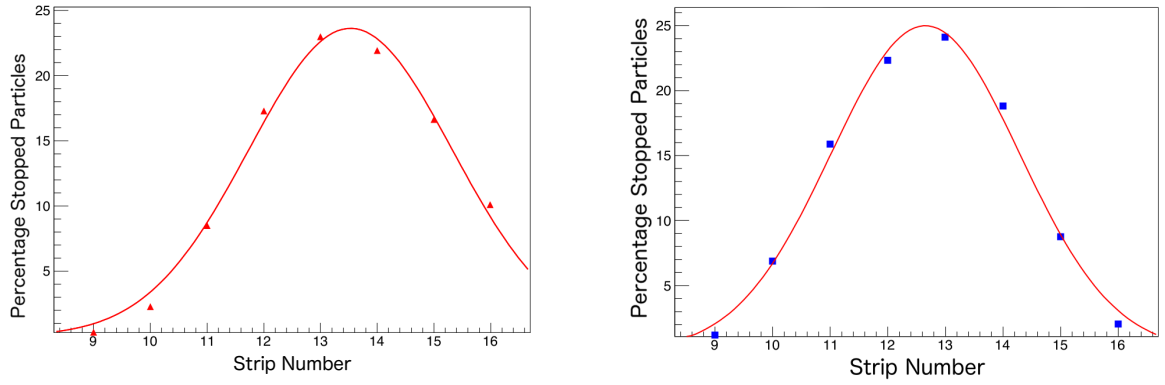

(a) (b)

Figure 5.10. Plot (a) shows the beam stopping profile from December 2018, with 450 Torr pressure in MUSIC. The percentage of all of the beam particles that are stopped in each strip is plotted versus strip number. The red curve is a gaussian fit to the data, with a mean value of strip 13.5 and $\sigma = 1.8$. Plot (b) is the beam stopping profile from February 2019, with 450 Torr pressure in MUSIC. The red curve is a gaussian fit to the data, with a mean value of strip 12.7 and $\sigma = 1.6$. Statistical error bars are included in both plots, but are smaller than the data point symbols.

5.10a is 13.5 strips, corresponding to a range of about 265mm in 450 Torr of methane. This is assumed to be the stopping position of a particle of mean beam energy. Using LISE++ to determine the energy of a particle with this range yields a value of 64.4 MeV. For comparison, the SRIM software predicts an energy of 68.8 MeV will have a similar range [41]. LISE++ is in closer agreement with the SPS measured energy of 61.5 MeV than SRIM, and only differs from measurement by 2-3 MeV. The calculated energies obtained from the measured range in the gas are compiled in Table 5.2. A similar result was found by Carnelli (2014), who did a series of ^{10,13,15}C beam energy measurements with the SPS [42]. In these measurements, the gas pressure in MUSIC was varied and the resulting beam energy measured. When the measurements were compared to LISE++ and SRIM calculations, the LISE++ calculations were more accurate for the ^{10}C and ^{13}C beams, and SRIM was more accurate for the ^{15}C beam.

As mentioned above, the pressure in MUSIC was 450 Torr in 2018. In 2019, most of the data were taken with 400 Torr of methane in MUSIC. Thus, for the sake of comparing the stopping distributions between 2018 and 2019, two hours of data were taken at a pressure

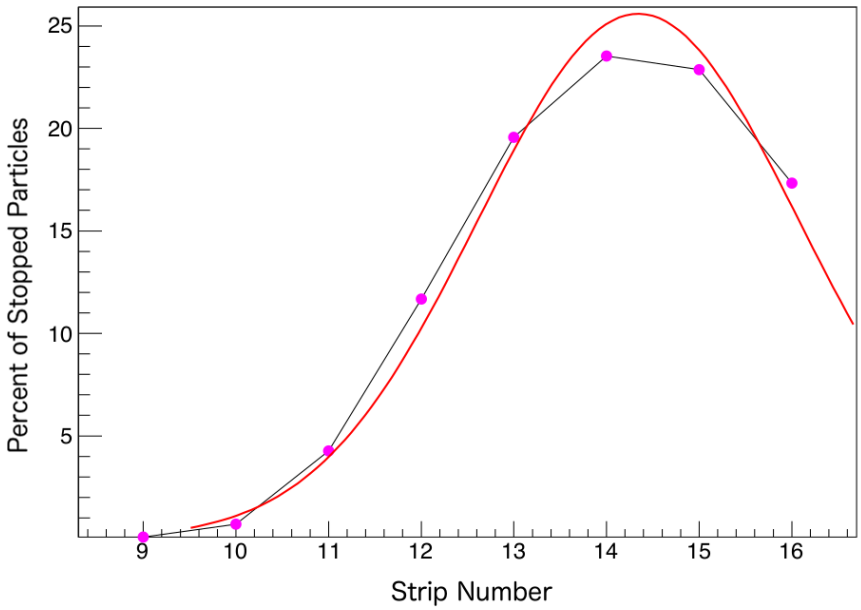

Figure 5.11. The beam stopping profile from February 2019, with 400 Torr of methane in MUSIC. The percent of all of the beam particles that are stopped in each strip is plotted versus strip number. The red curve is a gaussian fit to the data, with a mean value of strip 14.3 and $\sigma = 1.7$.

of 450 Torr in 2019. This is the data represented in Fig. 5.10b. The mean of a Gaussian fit to this plot shows that a beam particle of mean energy stops in strip 12.7 of the MUSIC detector. This corresponds to an energy of 62.1 MeV according to LISE++ and 66.6 MeV according to SRIM. Figure 5.11 shows the stopping distribution for the beam in 400 Torr of methane. Due to the reduced pressure, beam particles of mean energy travel about 1.5 strips deeper into the detector before stopping. Using LISE++ to predict the energy with the new range and 400 Torr of pressure yields a similar energy result for the same beam, as shown in Table 5.2. From the measured range at this pressure (400 Torr), the energies predicted by LISE++ and SRIM were 61.3 MeV and 65.8 MeV, respectively.

Another approach to comparing the beam energy in 2018 to 2019 involves looking at the setting of the magnet upstream of MUSIC which selects the beam based on its magnetic rigidity, according to Eq. 4.1 discussed in Section 4.2. The bending magnet used to deflect the ^{16}C beam towards MUSIC was set to 5643 G in 2018 and 5631 G in 2019, meaning a

Table 5.2. Calculated ^{16}C beam energies from the measured stopping range in methane.

Date	Calculation Tool	Pressure (Torr)	Energy (MeV)
2018	LISE++	450	64.4
2018	SRIM	450	68.8
2019	LISE++	450	62.1
2019	SRIM	450	66.6
2019	LISE++	400	61.3
2019	SRIM	400	65.8

Note: Calculations were performed using LISE++ and SRIM for three different hours of data, one taken in 2018, and two taken in 2019 at two different pressures in MUSIC.

change of 0.2% in the magnetic field between the two years. Using Eq. 4.1, a difference of 0.2% in the magnetic field is proportional to a difference of 0.4% in energy. Assuming that the 2018 beam energy before passing through any materials was 219.8 MeV, from Table 5.1 row 2, and scaling this energy according to the difference in magnetic field strength gives an energy of 218.9 MeV in 2019 (row 5, Table 5.1). Using the energy 218.9 MeV, LISE++ predicts the energy of ^{16}C after passing through the PPAC, entrance window, and degrader to be 61.5 MeV entering the detector (row 6, Table 5.1). This number is comparable to the values of 62.1 MeV and 61.3 MeV found using the stopping strips and LISE++ (rows 3 & 5 in Table 5.2).

In summary, from Tables 5.1 and 5.2, here are the conclusions drawn. From Table 5.1, row 4, the mean energy of the ^{16}C beam was accurately measured in 2018 with the SPS and determined via Gaussian fit to have a mean of 61.5 $\pm$ 0.1 MeV and a standard deviation of 5.4 $\pm$ 0.1 MeV . Comparing this energy with the analogous energy predictions for 2018 in Table 5.1 row 3 and the first two rows of Table 5.2 shows that LISE++ and SRIM predict slightly higher energies than the measured energy. Considering only the LISE++ predictions, the predictions are higher than the measured energy by 2 to 3 MeV. For 2019, there are three energies determined using LISE++. Table 5.1, row 6 predicts an energy of 61.5 MeV using magnetic scaling and LISE++ energy loss predictions. The predicted energies in Table 5.2 from the range in 450 Torr and 400 Torr methane are 62.1 MeV and 61.3 MeV, respectively.

Taking the average of these three 2019 predictions gives a predicted energy of 61.6 MeV. As stated earlier, the LISE++ predictions were shown to be 2 to 3 MeV higher than the actual energy for the 2018 experiment, thus the mean energy of the beam in 2019 is in the range 58.6 MeV to 59.6 MeV. We assume that the spread in energy of the 2018 and 2019 beams entering the MUSIC gas volume is the same because the width of the stopping distributions shown in Fig. 5.10 for both are similar. The width of the energy distribution measured in the SPS was 12.8 MeV full-width at half maximum, or a standard deviation of 5.4 MeV. Given that this energy spread is large compared to the uncertainties in the beam energy, we adopt a value of 59.1 MeV for the mean energy of ^{16}C entering the gas volume of MUSIC during the 2019 run. The systematic uncertainty in this energy is about $\pm$ 0.5 MeV, which is small compared with the spread in the beam energy.

5.4. Fusion Event Simulation using SRIM

For the correct identification of fusion events, it is essential to understand the MUSIC detector response to different types of events such as fusion, unreacted beam, and elastic scattering. The shape of traces from fusion events can vary greatly, depending on which evaporation residue is produced and the kinematics of the evaporated particles. As shown in Eq. 4.2 in Section 4.2, the energy loss of an ion in gas is proportional to its charge squared. The various possible evaporation residues produced by fusion have different atomic numbers. This means that the different elements will produce different stopping signals in the detector. However, the variation in emission angle and energy of the evaporated particles makes it difficult to distinguish between different residual nuclides with the current analysis because there is a smooth distribution of possible features of each fusion event. Carnelli, in his 2014 thesis, modeled the evaporation residues for the ^{15}C + ^{12}C fusion system using the code FLUKA, which is a tool for calculating particle interactions with matter, and found similar results - i.e. that individual nuclides could not be distinguished in his analysis [42].

In order to simulate fusion events, one must first predict the species of residual ions expected. The program LISE++ incorporates the code Projection Angular-momentum Cou-

pled Evaporation (PACE) into its suite of functionalities called PACE4 [36]. PACE4 is a fusion evaporation code using Monte-Carlo with angular momentum coupling to calculate fusion residue cross sections, as described in Ref. [43]. In this work, PACE4 was used to predict what evaporation residues are expected to result from the fusion systems studied. Tables 5.3 and 5.4 show the predicted evaporation residues, the percent of fusions resulting in each, and the predicted cross sections for ^{16}C incident upon ^{12}C at E_{lab} = 50 MeV and 25 MeV, respectively. These energies correspond to the energy of the ^{16}C beam in strip 1 of MUSIC at E_{lab} = 50 MeV and strip 9 at E_{lab} = 25 MeV. These tables were generated using 1,000,000 simulated events.

Using similar predictions, the ^{16}C + ^{13}C fusion system results in the same atomic species, (primarily Mg, Na, and Ne) though with more neutron-rich isotopes. For example, with incident energy E_{lab} = 50 MeV, the ^{16}C + ^{12}C system forms ^{26}Mg for 3.54% of the fusion reactions, while the ^{16}C + ^{13}C system produces it for 19.8% of fusion reactions. Comparing this with the production of ^{25}Mg, this shift toward more neutron-rich isotopes is evident: the fusions of the ^{12}C system produce this nuclide for 35% of reaction, while the ^{13}C system produces it for 22% of reactions. A similar trend is seen for fusions at E_{lab} = 25 MeV. Because the energy loss of these evaporation residues in gas is proportional to the charge squared, these differences in isotope distribution do not change how the fusion-finding analysis should be performed for the ^{16}C + ^{13}C fusion system.

A simulation of the energy loss in each strip of MUSIC was developed by Dr. Daniel Santiago-Gonzalez to generate predicted fusion traces [44]. This simulation produces plots of the predicted energy loss per strip for different fusion products and was used to help determine the ideal parameters for identifying fusion events in the data. For this discussion, we will use the ^{16}C + ^{12}C system, but this can be generalized to the ^{16}C + ^{13}C reaction as well. To initialize the simulation, the energy and species of the ion entering the detector is specified, as well as the strip in which to simulate fusion. The reaction point along the beam axis within the depth of the specified strip is randomized, and the energy loss of ^{16}C

Table 5.3. Evaporation residues predicted for ^{16}C incident on ^{12}C with E_{lab} = 50 MeV.

Z	N	Residual Nuclide	%	σ (mb)
12	16	^{28}Mg	0.03	0.362
12	15	^{27}Mg	0.10	1.22
12	14	^{26}Mg	3.54	42.2
11	15	^{26}Na	1.21	14.4
10	16	^{26}Ne	0.02	0.243
12	13	^{25}Mg	35	418
11	14	^{25}Na	9.55	114
10	15	^{25}Ne	0.10	1.17
12	12	^{24}Mg	0.17	2.01
11	13	^{24}Na	0.08	0.982
10	14	^{24}Ne	0.42	4.97
10	13	^{23}Ne	23.1	276
9	14	^{23}F	0.33	3.89
10	12	^{22}Ne	21.2	253
9	13	^{22}F	0.09	1.07
10	11	^{21}Ne	2.82	33.6
8	12	^{20}O	0.40	4.68
8	11	^{19}O	1.75	20.8
		TOTAL	100	1.19e+03

Note: For isotopes occurring less than 1% of the time, the percent occurrence is rounded to the hundredths decimal place. Isotopes occurring less than a one hundredth of a percent are omitted.

from the entrance window to that point is used to determine the 4-momentum of the beam. The 4-momentum of the ^{16}C beam and the stationary ^{12}C target are considered to be the initial total 4-momentum of the compound nucleus ^{28}Mg* in an excited state, with a total center-of-mass energy determined by conservation of 4-momentum.

Next, the compound nucleus undergoes a chain of particle evaporations specified by the user in the initialization file. The algorithm goes through each evaporation residue in the specified chain following conservation of 4-momentum to determine the energetics of each evaporation. At each step, the excitation energy of the evaporation residue is randomly selected from a range of values between half of the reaction Q value and the full Q value. In the center-of-mass frame, the kinetic energy of the system is shared between the two

Table 5.4. Evaporation residues predicted for ^{16}C incident on ^{12}C with E_{lab} = 25 MeV.

Z	N	Residual Nuclide	%	σ (mb)
12	15	^{27}Mg	1.83	16.2
11	16	^{27}Na	0.35	3.06
12	14	^{26}Mg	25.4	224
11	15	^{26}Na	4.09	36.2
12	13	^{25}Mg	37.2	329
11	14	^{25}Na	2.92	25.8
10	14	^{24}Ne	0.92	8.16
10	13	^{23}Ne	26.7	236
9	14	^{23}F	0.06	0.517
10	12	^{22}Ne	0.40	3.5
8	12	^{20}O	0.05	0.409
8	11	^{19}O	0.01	0.0442
		TOTAL	100	884

Note: For isotopes occurring less than 1% of the time, the percent occurrence is rounded to the hundredths decimal place. Isotopes occurring less than a one hundredth of a percent are omitted.

final particles. For simplicity, the emission angle of the evaporated particle is assumed to be isotropic and is randomly selected, ignoring potential angular distributions, and the emission of γ-rays is ignored. After each evaporation, if the excitation energy of the residual nucleus is above the separation energy of the next particle in the specified evaporation chain, the next particle in the chain is evaporated until no additional particle evaporations are energetically allowed.

The simulation creates a model of the active volume of MUSIC, segmented into the different volumes defined by the area of each anode strip or strip segment times the height of the active volume. The energy losses of the ^{16}C ion, the evaporated ions, and the residual ion are calculated using stopping-power tables generated using the SRIM software [41]. These tables indicate how much energy is lost per unit of distance (e.g. mm) for each possible evaporation residue based on the gas density, the ion species, and energy. From Table 5.3, the most common evaporation residues expected are ^{25}Mg, ^{23}Ne, and ^{22}Ne. Beginning from the compound nucleus, ^{28}Mg, there are two different chains of particle evaporation that can

create these residues. To obtain ^{25}Mg, three neutrons evaporate from the compound nucleus (see Fig. 5.12). To obtain ^{23}Ne or ^{22}Ne, an α is evaporated, followed by single or double neutron evaporation (See Fig. 5.13). The left image in both figures shows the simulated active volume of MUSIC and the simulated particle trajectories within the detector. The right images show the expected fusion traces generated by the energy losses of the ions in each segment of the detector. These traces are idealized because effects such as detector noise and zero offsets from the electronics are not included.

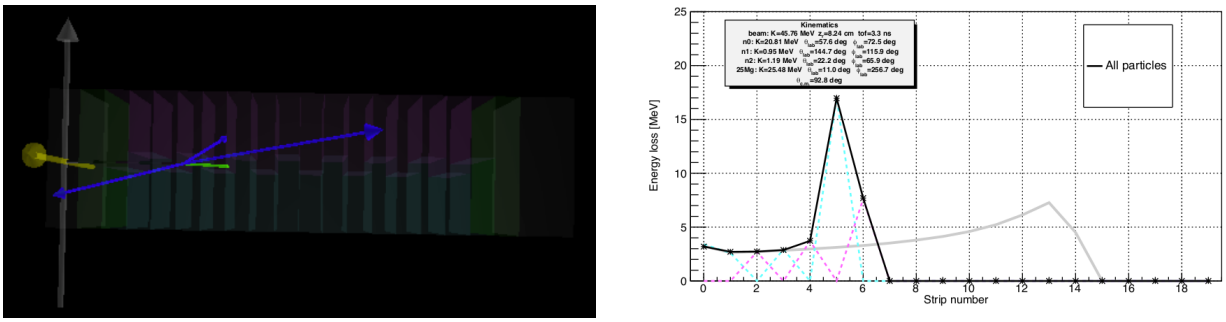

(a) (b)

Figure 5.12. Figure (a) shows the trajectories of the particles in the MUSIC detector for fusion occurring in strip 3. The centered, black arrow is ^{16}C, the blue arrows are evaporated neutrons, and the green arrow is the fusion residue ^{25}Mg. The plot in (b) shows the associated fusion trace, where the dashed blue line represents the energy deposited in the left segments of each strip and the dashed pink line is for the right segments. The black line shows the sum of the left and right signals and the gray line indicates the Bragg curve for an unreacted ^{16}C beam particle.

The general shape of a MUSIC fusion trace is identified by the transition from a beam-like ^{16}C signal to an evaporation residue, which has a shorter range in the detector due to its higher proton number and therefore charge (see Section 4.5). As depicted in Fig. 5.12a, the ^{16}C fuses with ^{12}C and three neutrons are evaporated, leaving the evaporation residue moving in the forward direction. The fusion trace in Fig. 5.12b shows that the strip after the fusion occurs has a significant increase in signal, corresponding to an increased energy deposited in the volume of the detector corresponding to that strip, which rises into a large peak. Because ions with greater charge lose more energy in a shorter range, the trace goes to zero within 2-5 strips. These characteristics are typical for chains of neutrons evaporating. The

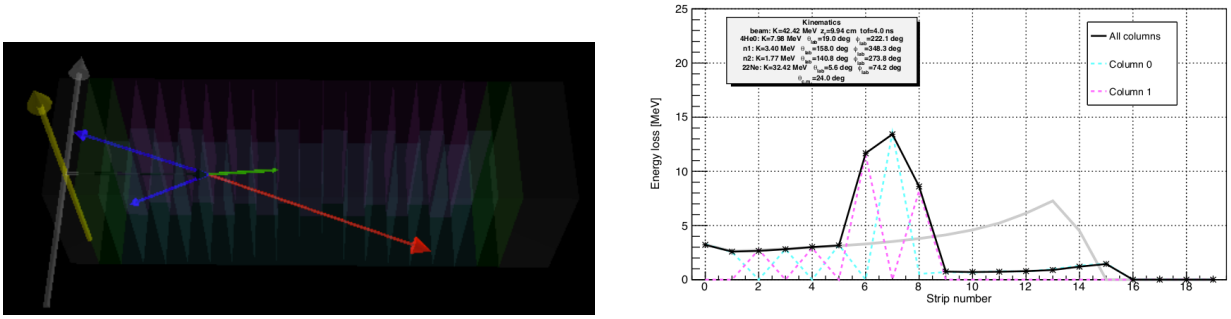

(a) (b)

Figure 5.13. These images represent a fusion event occurring in strip 5, resulting in ^{22}Ne. Figure (a) shows the ions traveling through the different layers of MUSIC. The black line is the ^{16}C before fusion, and the green line is the fusion residue, ^{22}Ne. The blue lines are evaporated neutrons and the red line is an evaporated α. This fusion event produces the trace in plot (b). The lines represent the same quantities as in Fig. 5.12. The α-decaying fusion events within a certain range of emission energies and angles show the α particle's energy loss in the trace.

specific shape of the fusion trace is significantly affected by the kinematics of the neutrons, or equivalently the kinematics of the residue. Thus, for each evaporation residue species, fusing at the same energies, there are a variety of shapes possible for each event. This makes it impossible to distinguish between different residue species using current analysis techniques.

As is evident from Fig. 5.13b, these characteristics are different for fusion events with α-evaporation. The trace in Fig. 5.13b does not go to zero once the evaporation residue stops in the gas, as the emitted α particle continues on depositing enough energy in each segment of MUSIC to be detected. Figure 5.14 shows a different α-evaporation trace, which has emitted an α particle in the opposite direction of the residue's direction of motion. Instead of showing a clear transition from the ^{16}C beam to the evaporation residue, there is a hump from this alpha. The fusion selection criteria must, thus, account for all events produced by fusion, despite the possible differences due to different evaporation channels.

The simulated curves considered thus far have been easily distinguishable from a beam particle because they have a large amount of energy going into the fusion event ($E_{C.M.} >$ 17 MeV). Considering events with $E_{C.M.} < 4$ MeV occurring in strip 12 of the detector and beyond, the fusion events become much more difficult to identify. The trace in Fig. 5.15a

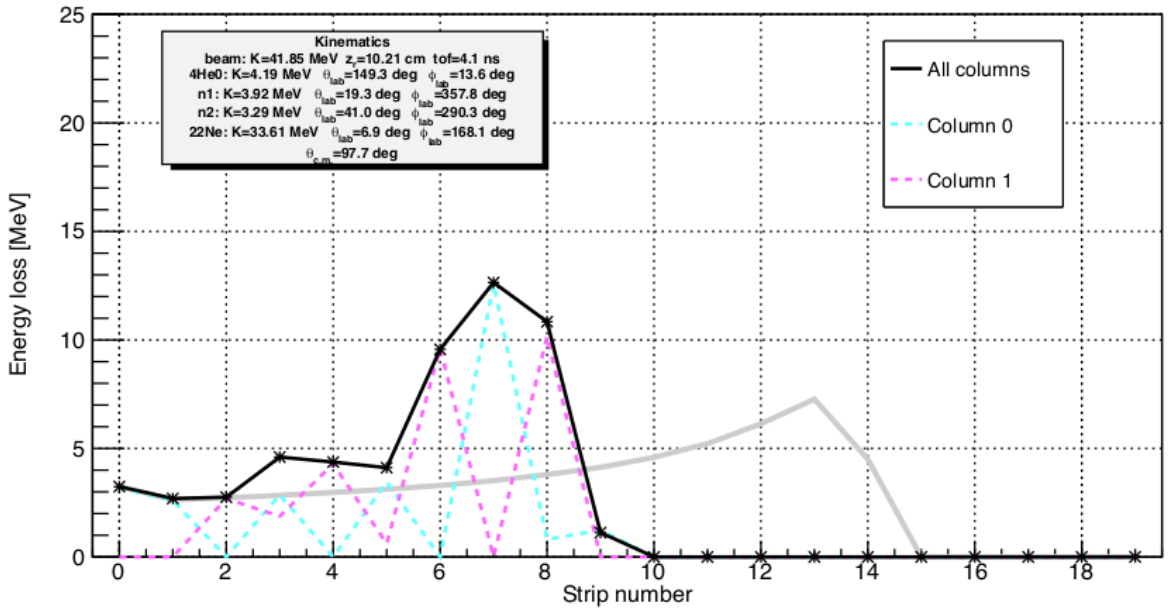

Figure 5.14. This fusion trace represents a fusion event occurring in strip 6 and resulting in the evaporation residue ^{22}Ne. The hump in strips 3 and 4 is the energy deposited by a backscattered alpha that stops in strip 3. This illustrates the variety of fusion traces expected in the data. The lines represent the same quantities as in Fig. 5.12.

results from a ^{26}Mg residue and has a peak that is clearly distinguished from the Bragg peak associated with ^{16}C stopping in the gas. Figure 5.15b shows a different fusion at a similar energy, resulting in a ^{25}Mg residue, which is indistinguishable from a beam particle. As a result, the efficiency of selecting fusion events decreases for large depths in MUSIC. How this efficiency changes with increasing strip number is examined in the next section.

5.5. Identifying Fusion Events for ^{16}C + ^{12,13}C

To distinguish fusion events from other signals in the detector, such as elastic scattering and beam like events, an algorithm was developed to check for certain qualities of each event to determine if it is fusion and where the fusion has occurred in the detector. Figure 5.16 outlines the steps of this algorithm. Each event is first loaded, then its energy deposited in strip zero and time-of-flight are required to fall in the ^{16}C gate. If it does, an energy calibration is performed, accounting for any drift in the electronics, which is present over time for all the data. The ^{13}C target data requires significant energy correction with time

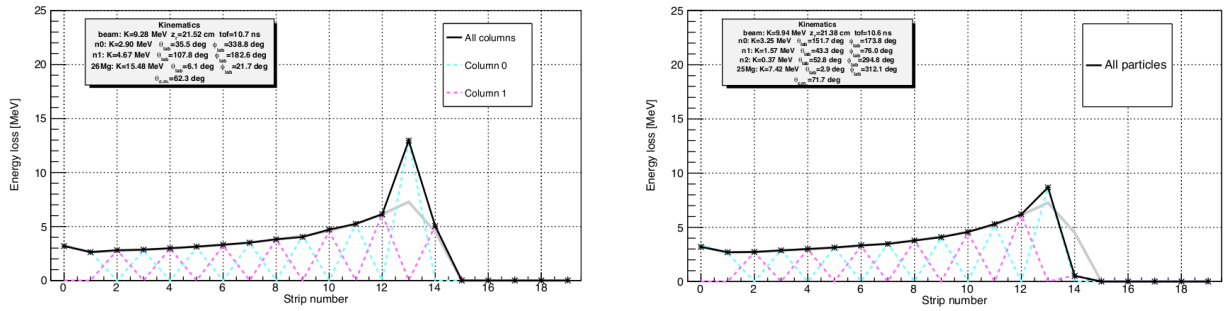

(a) (b)

Figure 5.15. Both of these plots show fusion traces for events fusing in strip 12, but with different evaporation residues. The fusion in plot (a) resulted in ^{26}Mg, while the fusion in plot (b) resulted in ^{25}Mg. The lines represent the same quantities as in Fig. 5.12.

because of the oxygen poisoning changing the apparent gain of the detector as described in Section 5.2. These calibrations are made relative to the LISE++ calculated energy loss of a beam-like particle, shown in Fig. 5.5.

The algorithm next loops through strips 2-14, restricted to these strips because it checks the two strips before and after the selected strip to confirm an event as fusion. Therefore, strips 0, 1, 3, and 4, and 12, 13, 15, and 16 are checked to determine potential fusions in strips 2 and 14, respectively, as described below. For each strip, four logical gates are checked. First, the trace must be centered up until the strip before the current fusion check strip. This is required for all events. Events that are centered in the previous strip but do not pass the rest of the fusion test are considered as incident particles for that strip. Determining the number of incident particles in the previous strip is required for the normalization of the cross section. The next three logical statements check the shape of the trace to determine if it is fusion-like (shown in the green boxes in Fig. 5.16). These logic statements are explained in detail below.

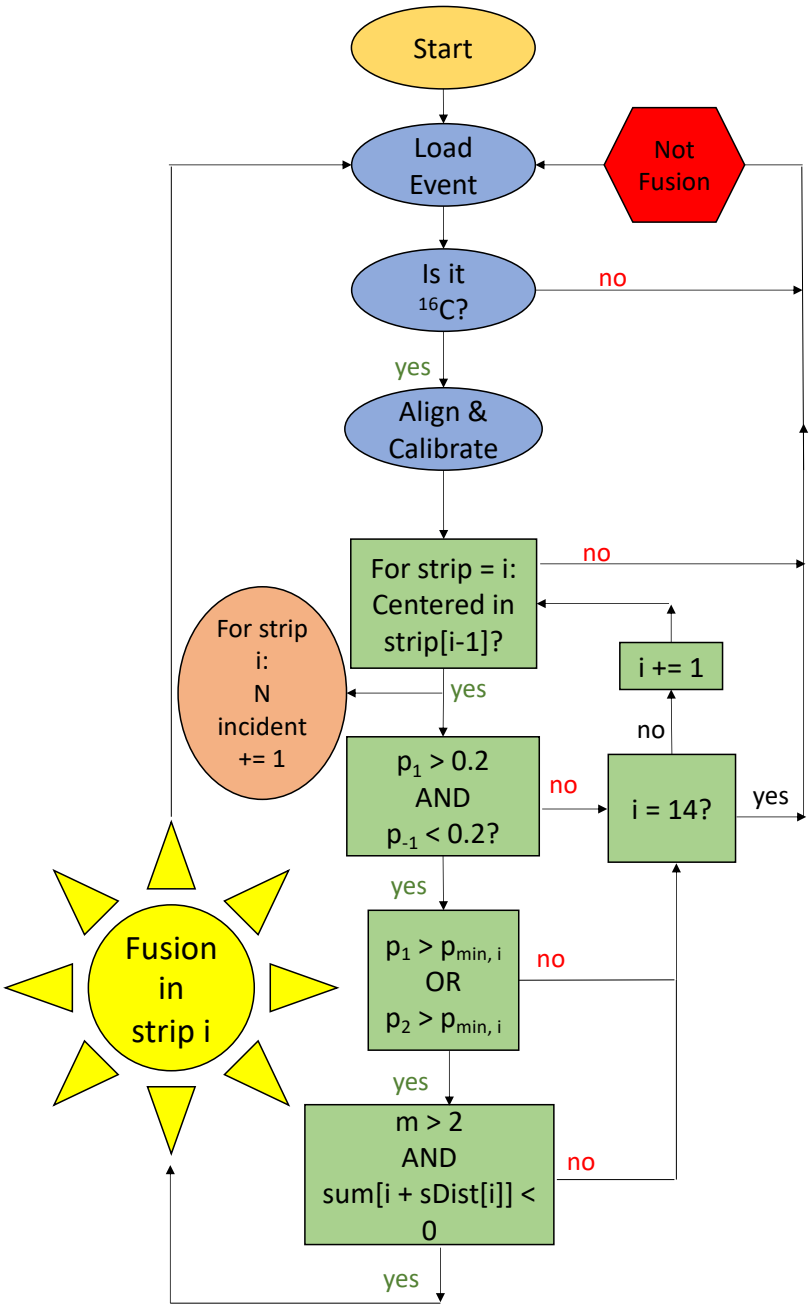

Figure 5.16. This flow chart demonstrates the steps that the analysis code takes to separate fusion events from all others. The parameters p_1, p_{-1}, p_2, p_{min}, m and $dist$ are defined in the text. For strip i, the number of incident particles is determined by the number of particles that is centered in strip i-1, thus every centered event is counted, as shown by the peach-colored oval. Later, if that event passes the rest of the logical statements (including the requirement that it be centered), it is counted as a fusion event.

To separate a larger fusion peak from the Bragg peak of an ion stopping in the gas, a test was developed that looks at the fractional change in signal/energy from one strip to the next. The fractional change was chosen rather than using an energy threshold because it is a parameter that does not depend on the spread in energy of the beam. As each strip is checked for fusion, the fractional change in signal/energy loss is calculated according to the equation

$$p_1 = \frac{(sum[i] - sum[i-1])}{sum[i-1]}. \tag{5.3}$$

Here, *sum* is an array of the signals in the left segments plus the signals in the right. It has 16 values which represent the trace of the event. The parameter i, which ranges from 1-16, selects for the value of sum corresponding to the current strip i, thus $sum[i-1]$ is the value of the previous strip. Similarly, the fractional change between the previous strip and the following strip is calculated according to the equation

$$p_2 = \frac{(sum[i+1] - sum[i-1])}{sum[i-1]}. \tag{5.4}$$

Both of these fractional changes are used to determine whether an event is fusion or not. A third fractional change is used to identify which strip the fusion has occurred in. This is the fractional change between the previous strip and the one before that

$$p_{-1} = \frac{(sum[i-1] - sum[i-2])}{sum[i-2]}. \tag{5.5}$$

The events shown in Figs. 5.17 and 5.18 offer a good illustration of how these parameters are used. Both of the fusion events in these figures are identified as fusion in strip 5. The difference between them is the location within the strip at which the fusion has occurred. The event in Fig. 5.17 has fused at the downstream end of strip 5, as evidenced by the relatively small increase from strip 4 to strip 5. Alternatively, Fig. 5.18 shows a large increase to almost the full peak height in strip 5, indicating a fusion early in strip 5. For

these events, the p_1 parameter is the percent change from strip 4 to 5 and p_{-1} is the percent change from strip 3 to 4. The analysis requires that p_1 be greater than 0.2, corresponding to a 20% increase, and p_{-1} be less than 0.2 for the fusion event to belong to strip 5. This distinguishes the event in Fig. 5.17 from a fusion in strip 6 and confirms that the fusion did not occur in strip 4. The requirement that $p_{-1} < 0.2$ and $p_1 > 0.2$ is applied to all strips in the detector and was chosen by visually inspecting the traces and determining how much of an increase appeared to define the beginning of a fusion peak. This value was kept low because another parameter, p_{min}, checks to make sure the fusion peak is large enough, as described below. Varying this requirement only changes the strip to which some fusions are attributed. This affects less than 10% of the fusion events when, for example, $p_{-1} < 0.4$ and $p_1 > 0.4$ is required for each particle.

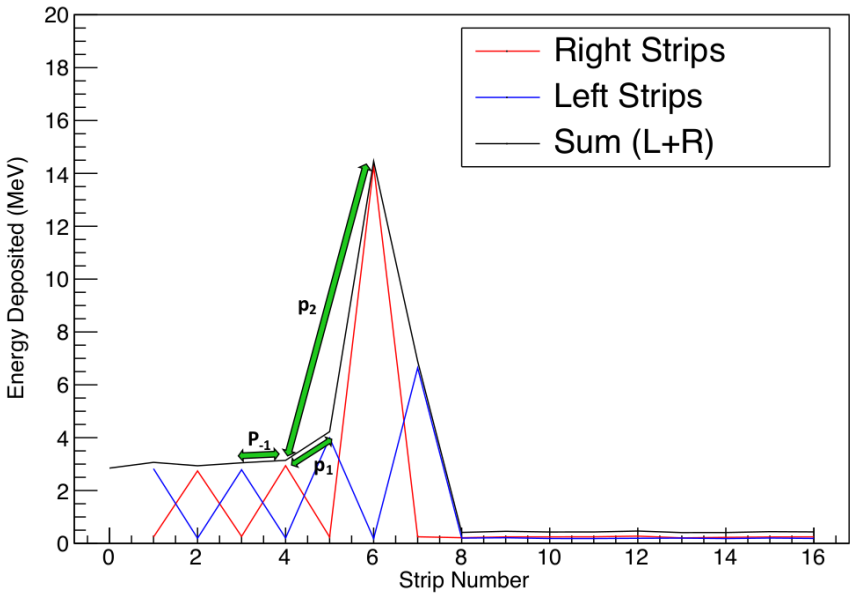

Figure 5.17. This trace is a fusion that has occurred deep in strip 5. It is an experimental trace from ^{16}C+^{12}C fusion. The marked parameters are defined in the text.

For each strip, a minimum fractional change (p_{min}) is determined, above which an event is considered to be fusion. Both p_1 and p_2 are checked to determine if they are larger than p_{min}. For a fusion in strip 5, the increase from strip 4 to the peak is required to be greater than $p_{min} = 0.5$, or a 50% increase. Because the event in Fig. 5.17 happens near the downstream

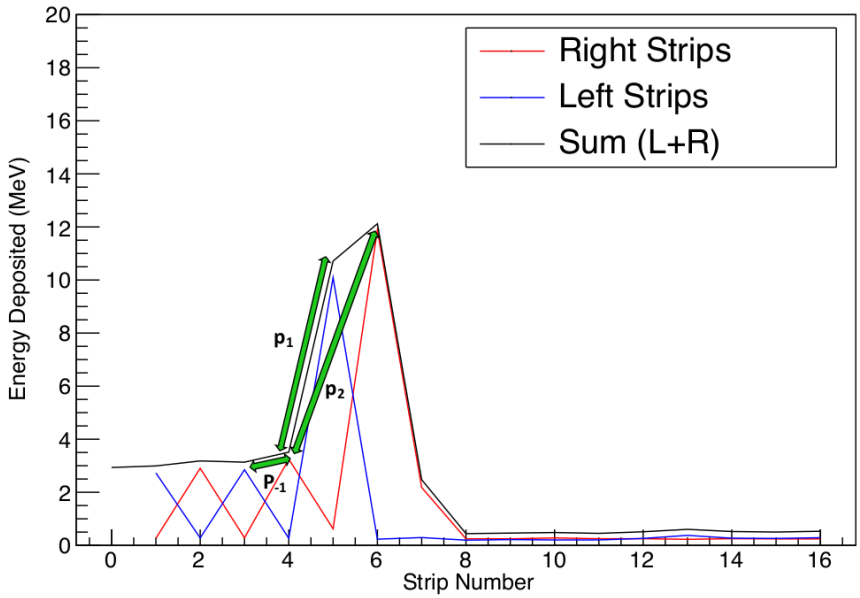

Figure 5.18. This trace shows a fusion that has occurred early in strip 5, where the evaporation residue has been deflected to the right by the kinematics of the evaporation process. It is an experimental trace from ^{16}C+^{12}C fusion. The marked parameters are defined in the text.

edge of strip 5, the increase from strip 4 to 5 and from strip 4 to 6 must both be checked for this value. Thus, to account for events like this, the analysis checks that either $p_1 > p_{min}$ OR $p_2 > p_{min}$.

With these requirements, the analysis successfully identifies a sharp increase in the data that is fusion-like, but additional requirements are necessary to distinguish fusion from elastic scattering, which can share this same feature. Figure 5.19 shows four events that are selected by the above requirements but are not fusion events. Plots (a), (b), and (c) are elastic scattering events with one particle clearly appearing off to one side in the detector, while the beam particle remains in the center or goes off to the other side. The final plot (d) is likely a beam particle that has been scattered to the side within the degrader, with particularly low energy. Two additional requirements are applied to the data to cut out events like these four. First, a parameter called multiplicity, m, is determined for all events. For each strip, if there is a non-zero signal in both the left and right segment, then the multiplicity is increased by 1. Thus, Fig. 5.19a is a $m = 2$ event and Fig. 5.19c is a $m = 4$ event. Most fusion events

have a multiplicity of 0 or 1, thus the analysis requires $m < 2$. This choice was informed by simulation because less than 5% of simulated fusion events had a multiplicity of 2, and none had a multiplicity $m > 2$. This requirement will cut out the events in plots (a)-(c) in Fig. 5.19, but it does not reject (d).

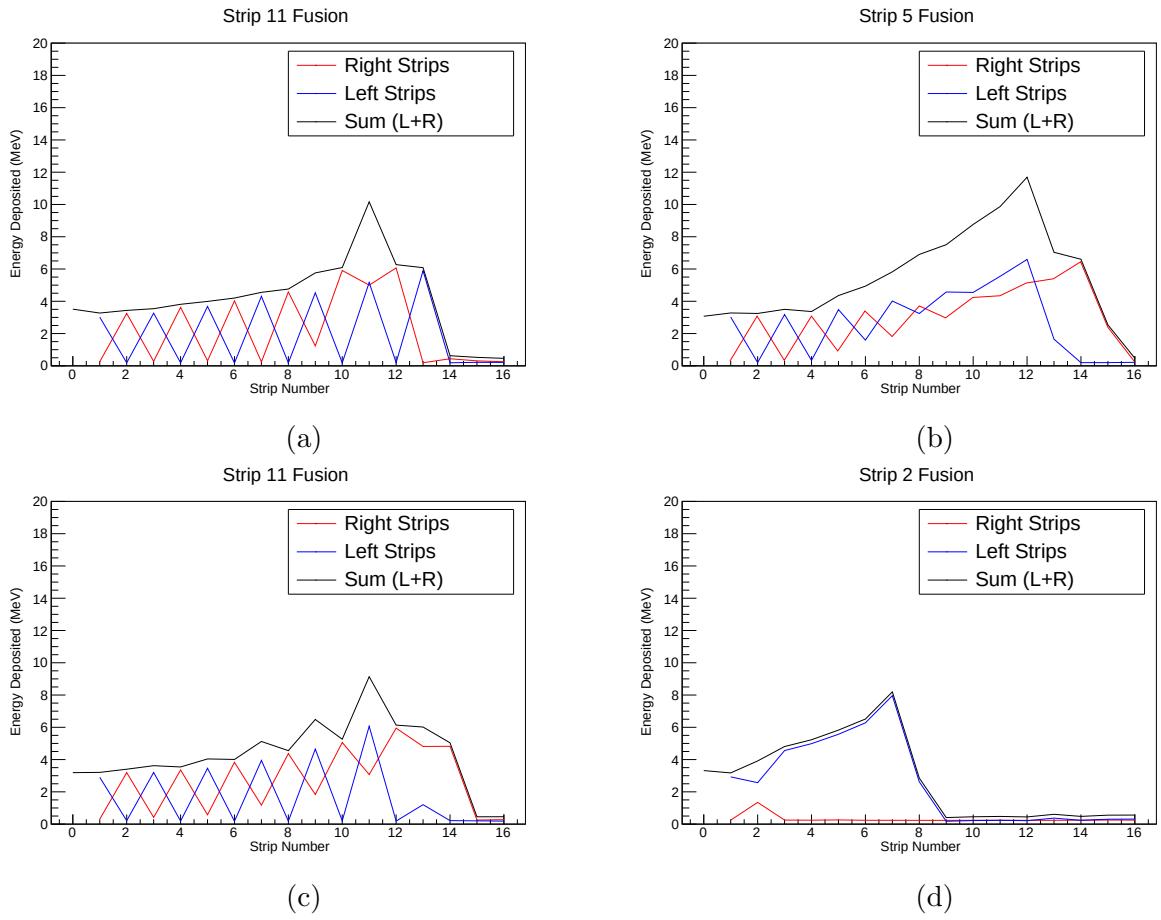

Figure 5.19. Non-fusion events selected by using only the percent change requirements to identify potential fusion events. Plots (a), (b), and (c) are elastic scattering events and plot (d) is likely a beam particle that has been angularly scattered within the degrader.

To reject the events like the one shown in Fig. 5.19d, the trace is required to go to zero within a certain distance of the fusion strip, a parameter called *sDist*. The center-of-mass energy of each fusion event and the kinematics of the evaporation events determine how far the evaporation residue will travel in the detector. Simulations show that fusion events occurring at higher energies (strips 1-5) produce a residue that will travel no more than 5 strips after fusion occurs. As the beam progresses deeper into the detector, the residues will

travel less far, even stopping within 1 strip at energies near the coulomb barrier. For each strip, the most generous stopping distance is assumed based on the stopping distances that the simulation produced, with less than 5% of the simulated traces going further than $sDist$. The analysis thus requires that the trace go to zero up to 5 strips or less after the fusion strip, depending on the depth of fusion in the detector. The number of fusions found for different $sDist$ parameter values was checked. When increasing $sDist$ by 1 for every strip, there was an effect of less than 5% on the cross section in most strips. In the deeper strips of the detector, this change led to the acceptance of many events that were not fusion such as elastic scattering that had a large effect on the cross section, greater than 10%.

The p_{min} parameter has a large impact on how many fusions are identified in the data and therefore requires careful consideration to select the range of appropriate values. The minimum fractional change parameter p_{min} is set individually for each strip due to the decreasing energy of fusion reactions as the beam slows down in the detector. To determine the best values for p_{min}, the analysis is performed multiple times with the parameter varied through a range of possible values to see how many fusion events are found for each value of p_{min}. Figure 5.20 shows the results of varying the p_{min} value for strip 4. For strips 1-5, the results look very similar to Fig. 5.20. As one might expect, at very high values of p_{min}, few fusions (or any events for that matter) will be found because fusion signals with smaller peaks are rejected. For very small values of p_{min}, many events will be falsely identified as fusion, such as elastic scattering. However, what we anticipate is a relatively broad range of p_{min} values that will reject scattering and other non-fusion events while returning nearly all the fusion events. In the data shown in Fig. 5.20, we see a clear transition at $p_{min} \sim 0.7$ where all improperly identified scattering events are eliminated and the number of fusions becomes almost constant with p_{min}.

To verify this, the same test was run on simulation data, assuming a ^{16}C incident energy of 59.1 MeV, and is shown in Fig. 5.21. The simulated events comprise 449 fusion events occurring in strip 4 that decay via neutron emission (results for events with α emission yield

similar results). From the simulations, it is apparent that the efficiency of fusion detection is poor at large values of p_{min}, as expected. The algorithm finds most of the fusion events at $p_{min} < 1.5$, where fusion finding efficiency is good. It should be noted that only fusion events are simulated, so we do not see a large increase in identified events from small p_{min} values from improperly identified scattering events.

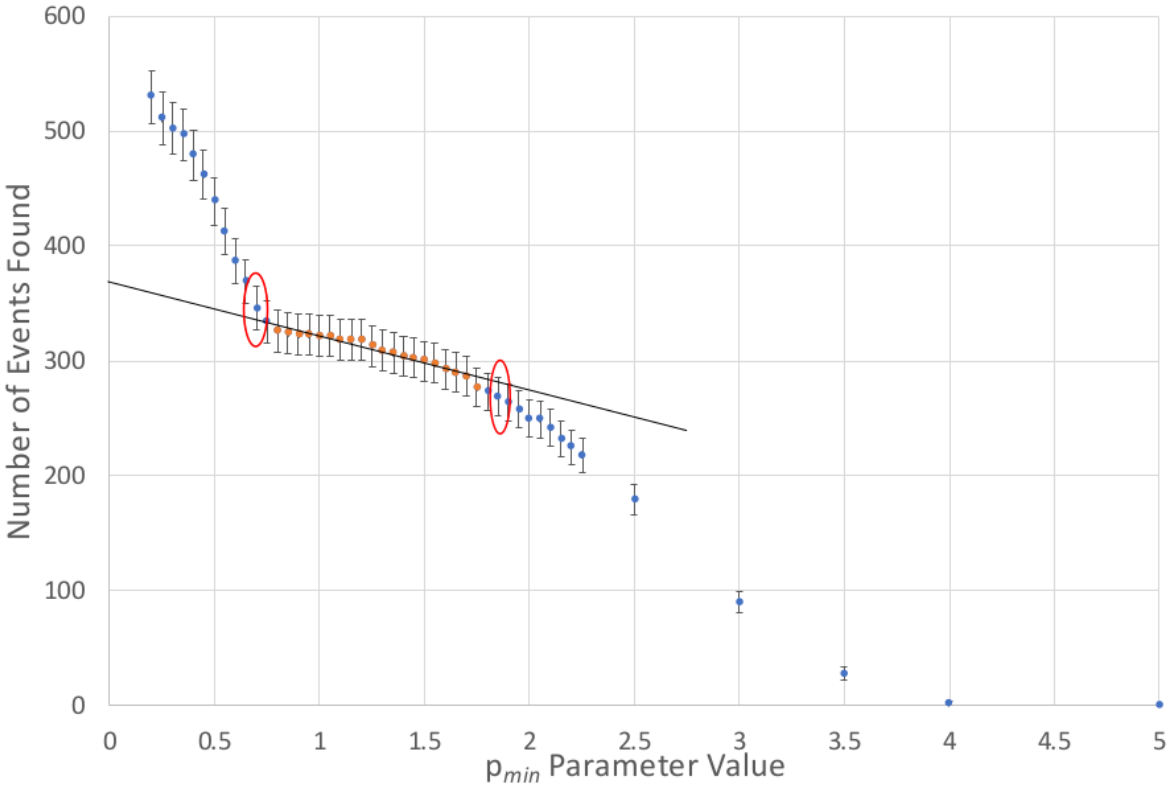

Figure 5.20. The number of fusions found in strip 4 in the data is plotted versus the value of the parameter p_{min} with statistical error bars. The other requirements made on these events were: the particle must be centered up to strip 3, $m < 2$, $p_{-1} < 0.2$, $p > 0.2$, and the trace must be zero by strip 10. The orange points show the range of p_{min} values that find roughly the same amount of fusions. The black line is a linear trend line that was fit to the orange data points. The maximum and minimum values of p_{min} (circled in red) were chosen to be the points with uncertainties consistent with the trend line.

The best value of p_{min} should have the highest efficiency possible (according to simulation), but be large enough that it is successfully cutting out non-fusion events. The region of lowest slope on the plot in Fig. 5.20 is at $p_{min} \approx 1.0$. This region of p_{min} selects for fusions only. The number of fusions in Fig. 5.20 does fall off as p_{min} is increased faster

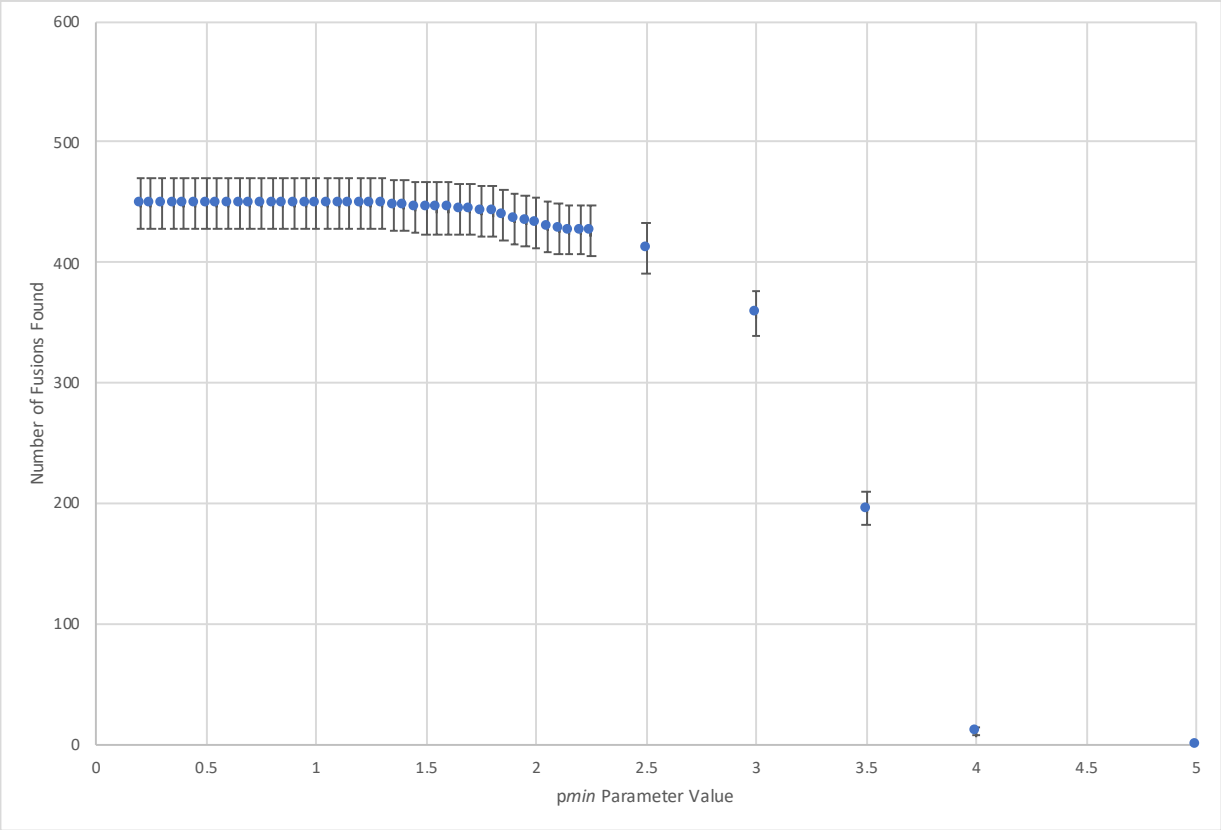

Figure 5.21. The number of fusions found in strip 4 for the simulated fusion events is plotted versus the value of the parameter p_{min} with statistical error bars. There are a total of 449 fusions that were simulated for strip 4. In addition to the value of p_{min} required for each fusion search, the algorithm required $m < 2$, $p_{-1} < 0.2$, $p > 0.2$, and $sDist = 5$ strips.

than predicted by the simulation, suggesting that there are effects in the detector that the simulation does not include. For example, one limitation is that the simulation assumes a monoenergetic beam, while the beam in the experimental data has a large energy spread. Lower energy incident particles could result in a lower efficiency with increasing p_{min} not predicted by simulations.

However, it is also possible that some of the observed decrease in fusion with p_{min} could be due to the elimination of some rare non-fusion events. To be conservative, a linear trend line, shown in Fig. 5.20, was fit to the number of fusions around $p_{min} \approx 1.0$ (orange data points) and used to determine the maximum and minimum number of fusions. On either extreme of the trend line, the first and last data points that are statistically consistent with

the trend line are taken to be the minimum and maximum values of p_{min} (circled in red). These values are used to find the systematic error in the cross section, by finding the cross section for this range of p_{min} values. The mean cross section is found by taking the middle value of the number of events between the maximum and minimum values of p_{min}.

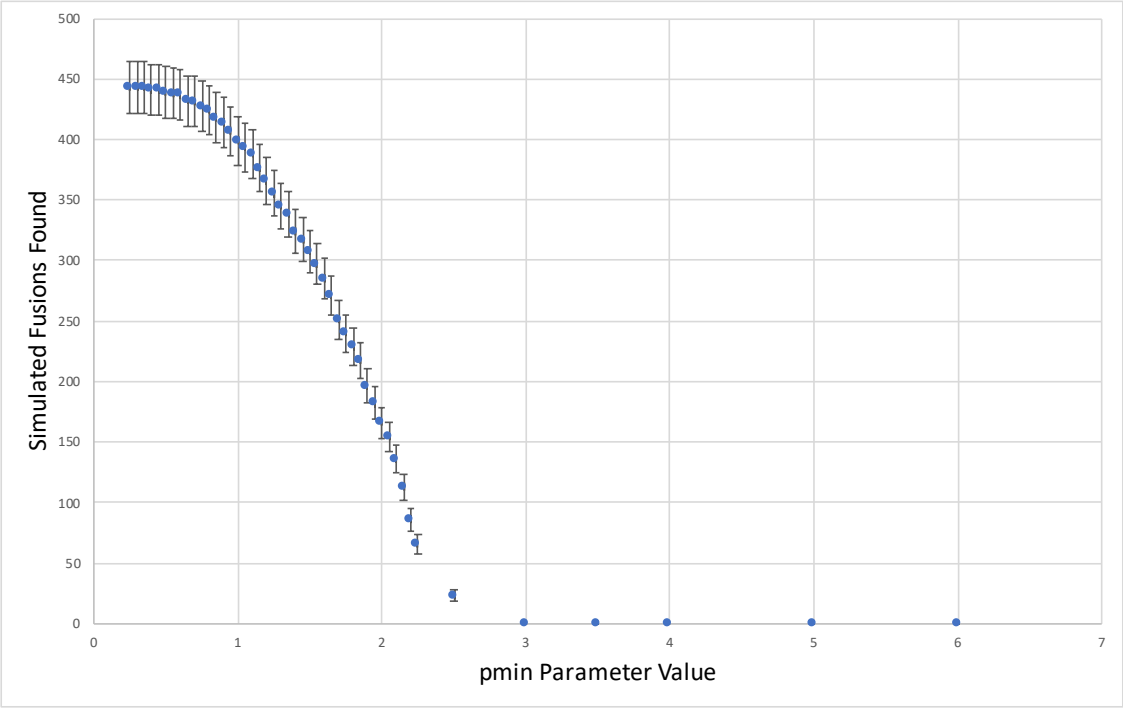

Figure 5.22. The number of simulated fusions found for each value of the p_{min} parameter is shown for strip 9. There are 444 total simulated events, which were simulated using a decay chain of neutron evaporations. Error bars are statistical.

In strips 1-6 of MUSIC, it is possible to select a p_{min} value that is nearly 100% efficient at identifying fusion in the simulation, and those values were selected for the analysis. However, deeper in the detector, fusion determination becomes less efficient due to the natural decrease in signal size of fusion with decreasing beam energy. The efficiencies for each value of p_{min} were determined for strip 9 using the simulated fusions found for each p_{min} value, and are shown in Fig. 5.22. The number of fusions found for each value of p_{min} was divided by the total number of simulated fusions, 444, giving the fractional efficiency. The number of fusions found in the data for each p_{min} value was corrected by dividing the number of fusions found at each p_{min} value by the fractional efficiency for the same value of p_{min}. Figure 5.23

shows the number of fusion events in strip 9 identified in the entire data set for different values of p_{min} before (orange points) and after (blue points) being corrected for the efficiency at each p_{min} value.

The plot in Fig. 5.23 was used to determine the number of fusions for the cross section calculation, as described in the following section. To determine this number, a subset of points (shown in grey) were selected by determining a the flattest region of the curve at the smallest value of p_{min} for which the number of fusions does not increase rapidly. A linear trend line was fit to these points. The data points with the most and least amount of fusions that are statistically consistent with the trend line (and near the grey points) were used to determine the upper and lower bound on the cross section. The points that are statistically consistent with the trend line at the highest p_{min} values are not used, since the efficiency is probably overcorrected in this region, as evidenced by the increase in number of fusions as the p_{min} value is increased. (We always expect a decrease in number of fusions with increasing p_{min}.) The average of the number of fusions from these two points was used to determine the value of N_f used to calculate the cross section. A similar method was used to determine the cross sections for strips 7-10.

5.6. Cross Section Calculation

Once the fusion events have been identified, the cross section is calculated strip-by-strip using the Eq. 5.1. The number of incident particles, N_i, is taken to be all ^{16}C events that are centered from strip 1 to the strip previous to the currently considered strip. The number of fusions, N_f, is the number fusions identified by the algorithm from the sample of centered incident events. The $\frac{N_t}{cm^2}$ term is found by multiplying the number of target atoms per cm^3 by the depth of the strip in MUSIC (1.6 cm). Finally, the efficiency, ϵ, is the efficiency determined by the simulations described in the previous section.

The cross section was calculated for strips 2-10 in the detector. The cross section was not calculated for strip 1 since there is insufficient information provided by strip 0 to successfully characterize the incident beam and selectively identify fusion. Strips 15-16 also have

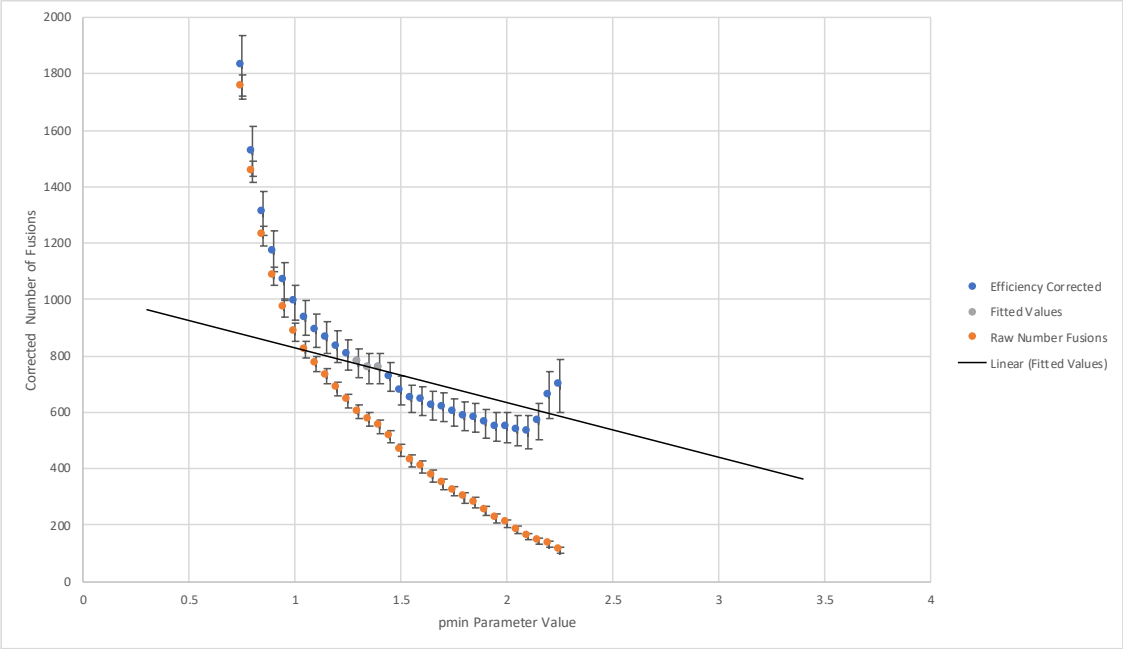

Figure 5.23. For strip 9, the raw number of fusions found for each value of p_{min} is shown as orange data points with statistical error bars. The efficiency corrected number of fusions is shown as blue points. The grey points show the points to which the linear trend line was fitted.

insufficient information from further into the detector to identify fusion. Strips 11-14 require more careful treatment than strips 2-10 to determine which events are fusion because a large fraction of the beam stops in these strips. Also, due to the spread in energy of the beam, the higher-energy beam particles contribute the bulk of the fusion events in these strips. To extract fusion cross sections at these lower energies (i.e. higher strip numbers), the number of fusions in these strips would have to be identified based on the incident particle energy on an event-by-event basis. Additional analysis of strips 11-14 is left for future work.

The program LISE++ was used to calculate how much energy was lost by the beam as it moved through the detector. The energy assigned to the cross section value of each strip is the energy at the middle of that strip for a particle with an incident energy of 59.1 MeV, which was determined to be the mean incident energy in Section 5.3. From LISE++ calculations, the mean energy loss in strip 2, due to the depth of the strip, is $E_{c.m.} = 1.24$ MeV ($\pm$ 3% of the beam energy), while strip 10 has a mean energy loss of $E_{c.m.} = 1.96$ MeV

(± 11% of the beam energy). The energy spread of the beam was measured with the SPS to be ± 9%. At higher energies, the energy width of the beam dominates and the cross section in each bin is averaged over this spread. At lower energies, the energy spread due to the strip width dominates and the cross section is averaged over that spread instead.

Chapter 6. Results and Discussion

6.1. Results

The cross sections are plotted versus energy in the center-of-mass frame for the ^{16}C + ^{12}C and ^{16}C + ^{13}C systems in Figs. 6.1 and 6.2, respectively. The cross sections of the two systems measured here are very similar. This is expected when comparing the nuclear shell structure of ^{12}C and ^{13}C (see Fig. 3.2 for reference). The nucleus of ^{12}C has 6 neutrons, which fill the 1s shell and have an occupancy of four in the 1p shell. The ^{13}C nucleus has one additional neutron that is added to the 1p shell and has an RMS radius only slightly (1.7%) larger than that of ^{12}C, less than would be expected when scaling by $r = r_0 A^{1/3}$ [45]. However, the models by Singh *et al.* [29] show an enhancement of the ^{16}C+^{13}C cross section over that of ^{16}C+^{12}C by $\sim 6\%$ in the energy range of $E_{c.m.}$ = 15-22 MeV. As shown in Fig. 6.3 systematic uncertainties in the data are too large to determine if the enhancement of the ^{16}C+^{13}C cross section is observed. In the section 6.2, some approaches to potentially reduce these systematic uncertainties are discussed.

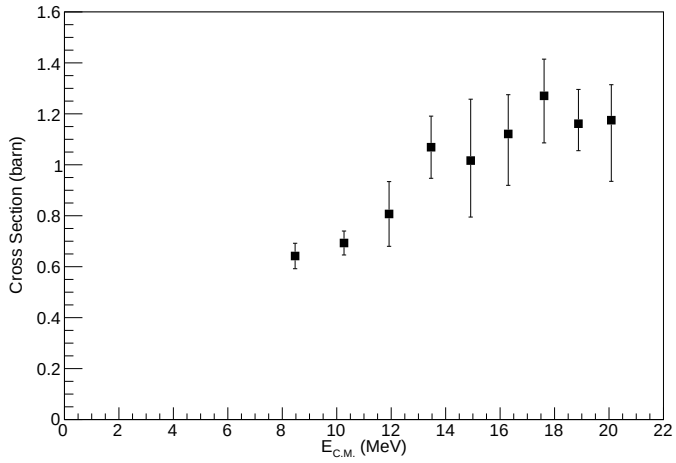

Figure 6.1. ^{16}C + ^{12}C fusion cross section plotted versus energy in the center-of-mass. The error bars are systematic uncertainties found by varying the p_{min} parameter and calculating its effects on the cross section. These systematic uncertainties dominate over the statistical uncertainty. The range of energies probed by each data point is discussed in the text.

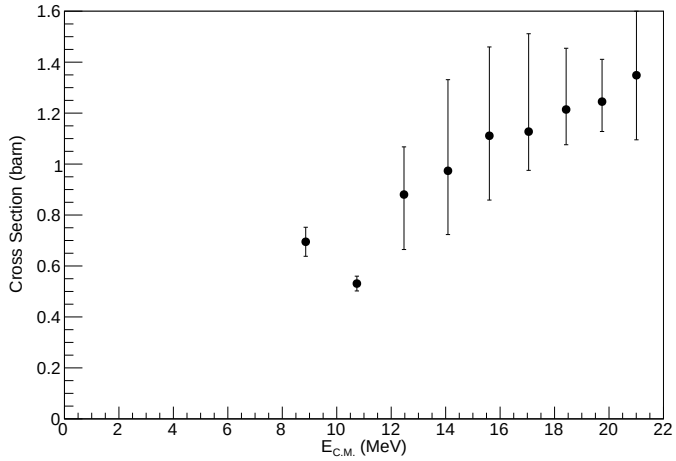

Figure 6.2. ^{16}C + ^{13}C fusion cross section plotted versus energy in the center of mass. The error bars are systematic uncertainties found by varying the p_{min} parameter and calculating its effects on the cross section. These systematic uncertainties dominate over the statistical uncertainty. The range of energies probed by each data point is discussed in the text.

The measured fusion cross sections for ^{16}C + ^{12}C and ^{16}C + ^{13}C are plotted along with predicted cross sections in Figs. 6.4 and 6.5, respectively. The predicted cross section from Beard *et al.* (described in Section 3.2) is shown with the ^{16}C + ^{12}C system, but was not calculated for the ^{16}C + ^{13}C system in their work [18]. The predictions by Singh *et al.*, shown on both plots, were made using the theoretical framework of the selective resonant tunneling model, assuming a complex square-well nuclear potential. Both cross sections in Figs. 6.4 and 6.5 show good agreement with the theoretical predictions.

Figure 6.6 shows the measured cross sections from this work with the cross sections measured by Carnelli *et al.* (2015) for the ^{15}C + ^{12}C system [10]. The ^{15}C + ^{12}C cross section is generally larger than the two ^{16}C cross sections measured in this work. As mentioned earlier in section 3.2, the RMS radius of ^{16}C inferred from high energy cross section measurements is larger than that of ^{15}C, according to Refs. [25] and [26]. Additionally, Fig. 3.3, shows that the RHFB model predicts that the neutron density of ^{16}C is larger than that of ^{15}C to large radii (7 fm), however the ^{15}C wave function is enhanced at even larger radii. This begs the question of why these results show that the ^{15}C + ^{12}C cross section is enhanced over that of

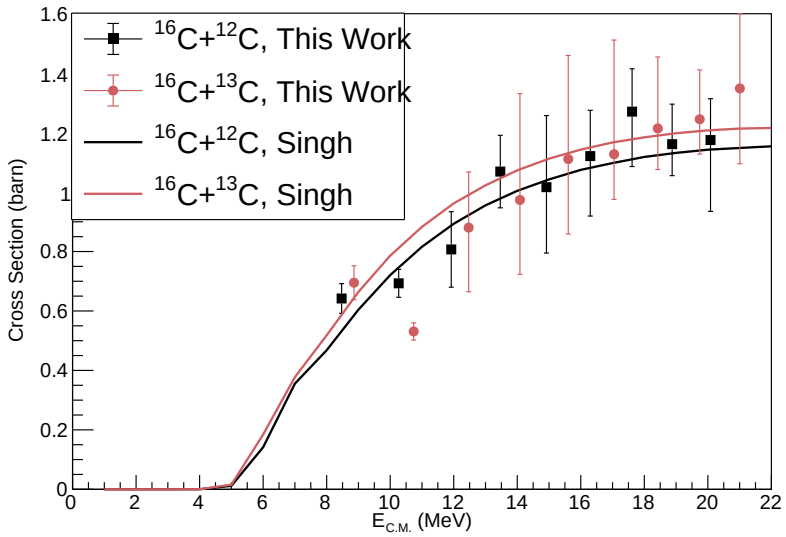

Figure 6.3. The ^{16}C + ^{12}C (black squares) and ^{16}C + ^{13}C (pink circles) fusion cross sections are plotted versus energy in the center of mass. The error bars are systematic uncertainties found by varying the p_{min} parameter and calculating its effects on the cross section. These systematic uncertainties dominate over statistical uncertainty. The theoretical models of these systems from Sing *et. al.* (2019) are plotted as well for comparison [29].

^{16}C + ^{12}C at these lower energies near the Coulomb barrier. The ^{15}C wavefunction tail may give rise to an enhanced cross section in ^{15}C through neutron transfer. Alternatively, pairing effects due to the paired neutrons in the sd shell of ^{16}C may reduce the ^{16}C cross section.

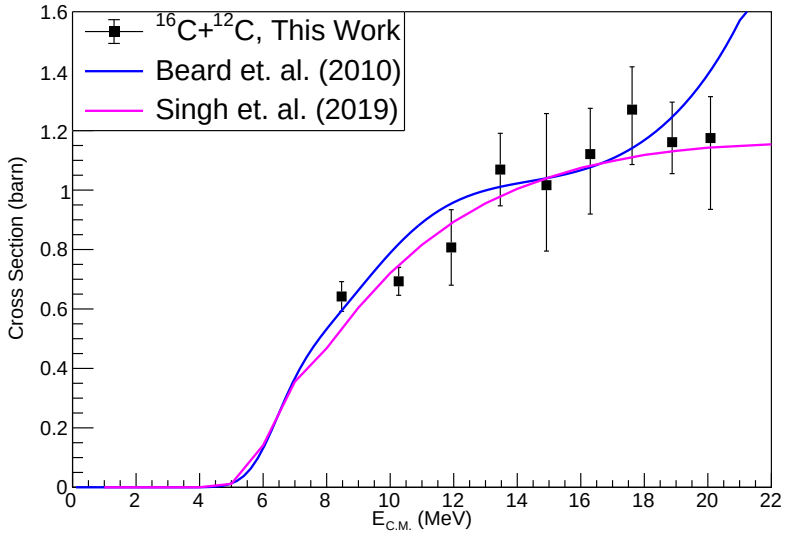

Figure 6.4. The measured ^{16}C + ^{12}C fusion cross section is plotted versus center-of-mass energy using black squares, with total error bars shown. The blue curve is the theoretically predicted ^{16}C + ^{12}C cross section from Beard *et al.* (2010) [18], and the magenta curve is the predicted cross section found by Singh *et al.* (2019) [29].

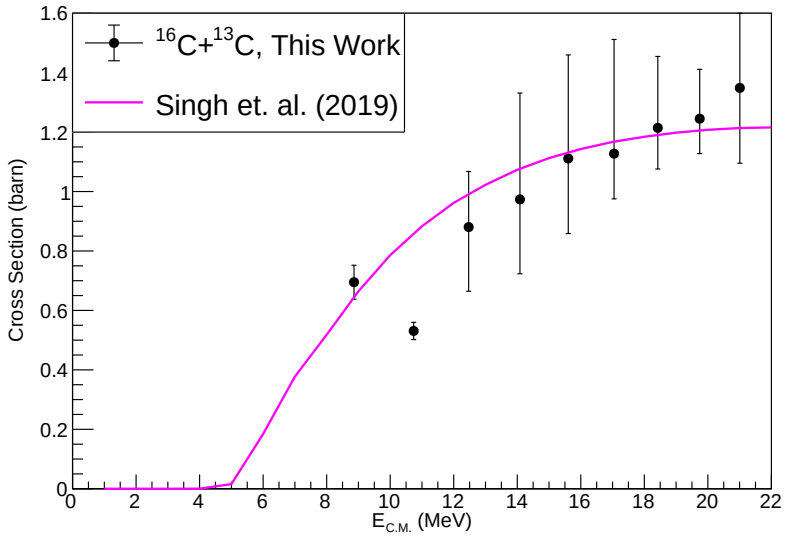

Figure 6.5. The measured ^{16}C + ^{13}C fusion cross section is plotted versus center-of-mass energy with black circles and total error bars shown. The magenta curve is the theoretically predicted ^{16}C + ^{13}C cross section from Singh *et al.* (2019) [29].

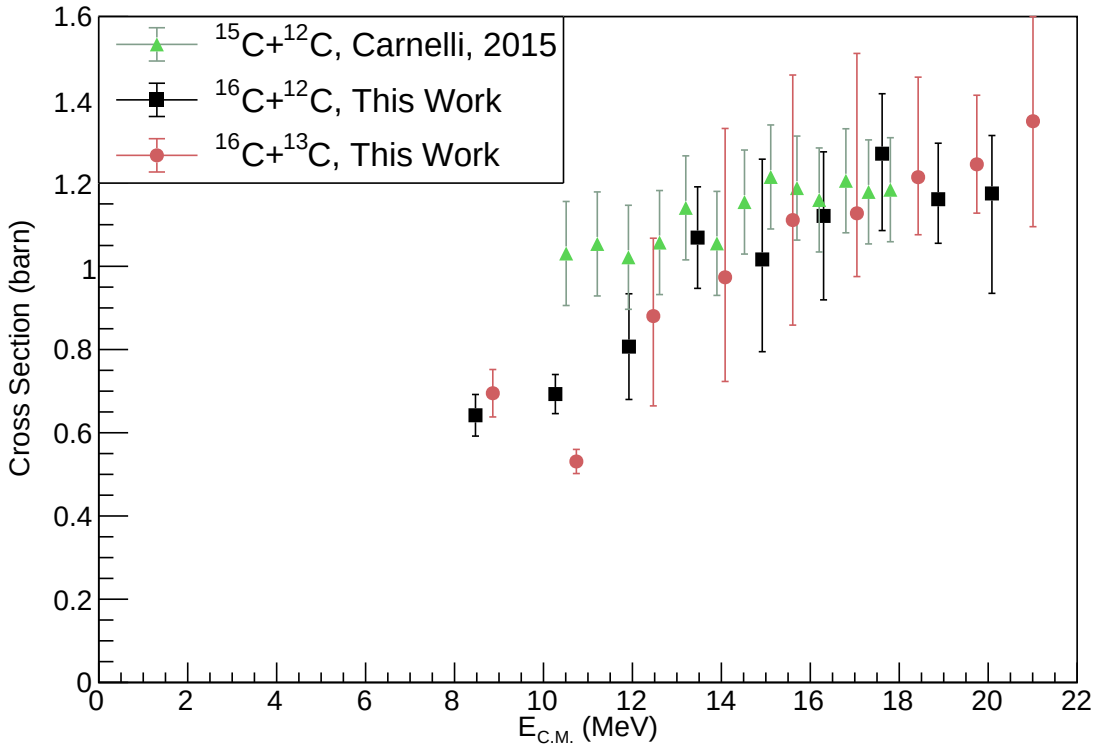

Figure 6.6. The measured ^{16}C + ^{12}C and ^{16}C + ^{13}C fusion cross sections are plotted with black squares and pink circles, respectively. They are plotted with the ^{15}C + ^{12}C cross section measured by Carnelli *et al.* (2015) in green triangles [10]. All data points have their total error bars shown.

6.2. Future Work

Decreasing the systematic uncertainties in these cross sections and determining the cross section at lower energy would offer a better constraint on fusion models. These improvements might be achieved for the existing detector by using a detailed simulation that uses Monte-Carlo determined distributions of incoming beam energies and angles. This simulation should also incorporate elastic scattering events in addition to fusion. Basing the energy losses in the simulation on the LISE++ energy-loss tables would also prove more accurate for the case of our ^{16}C beam.

To lower the systematic uncertainty, the efficiency corrections using the simulation data need to be improved. Incorporating a range of incident energies and angles in the simulation

would produce a more realistic distribution of fusions that should better reflect the data. With this better agreement between the data and simulations, the change in efficiency for each p_{min} value will more accurately reflect the efficiency of fusion finding in the data. This will require a more careful treatment of the average energy per strip because this quantity is currently determined using SRIM, which tends to under-predict energy losses [42].

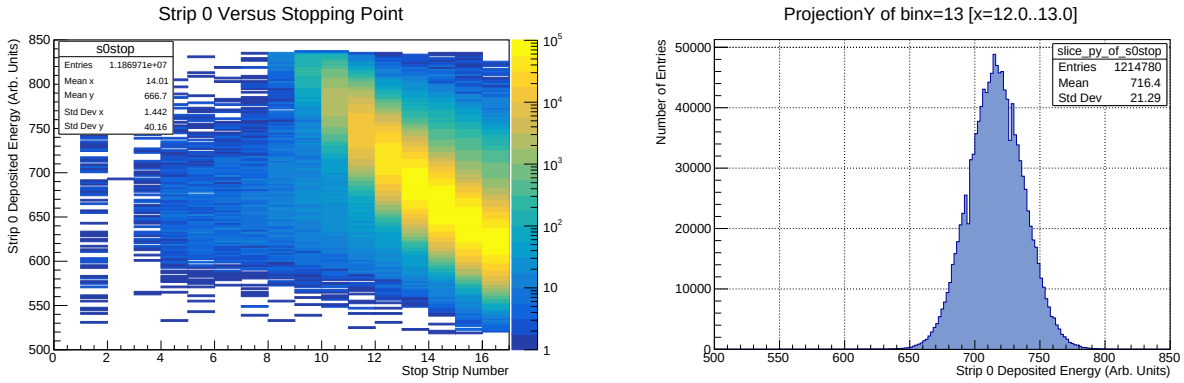

(a) (b)

Figure 6.7. Plot (a) shows the uncalibrated energy deposited in strip 0 plotted versus the strip in which each particle stops in the detector. Plot (b) shows a projection onto the y-axis of the events stopping in strip 12.

A more careful treatment of the average energy per strip and the determination of the cross section at lower energy can both be achieved by understanding the range we expect each event to have in the detector. On an event-by-event basis, a prediction can be made for this range. This lowers the reliance of the analysis on the inaccurate energy loss calculations by LISE++ or SRIM. If an accurate prediction of the range of each particle can be made, then the difference between the range and the fusion depth in the detector will inform what approximate energy the particle has with a LISE++ calculation that only deals with shorter ranges in the gas, and therefore should diverge less from the actual energy. Preliminary work has been done to incorporate this range prediction in the analysis.

To determine the expected range of each particle, a function that relates the energy deposited in strip 0 to the stopping point of an unreacted beam particle was fitted to the data. Figure 6.7a shows a plot of energy deposited in strip 0 versus stopping strip number.

The stopping strip is determined to be the last strip in which there is a non-zero signal. For each strip, the mean value of the energy deposited in strip 0 is determined by the centroid of a gaussian function fit to the 1D projection of each strip number in Fig. 6.7a onto the y-axis. This 1D projection is shown for strip 12 in Fig. 6.7b. Since most particles stop in strips 9-16, these strips were used to determine a relationship between energy deposited in strip 0 and range. Figure 6.8 shows the stopping strip number plotted versus the mean strip 0 value. A best fit to this plot was determined to be

$$Strip = e^{10.71-0.016\times E_0} + 31.13 - 0.027 \times E_0, \tag{6.1}$$

which is used to predict the range in the detector by inputing the uncalibrated value of energy deposited in strip 0.

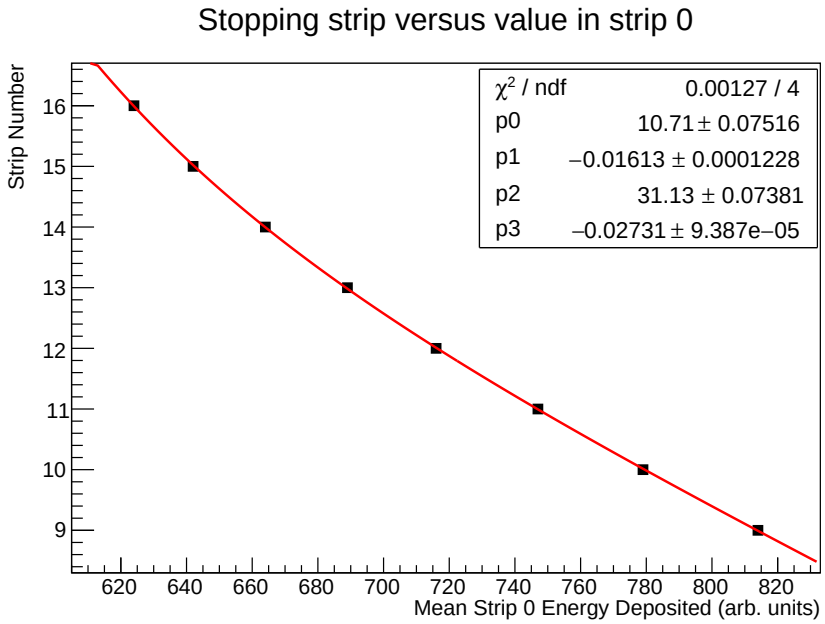

Figure 6.8. For the last strips in MUSIC, the strip number is plotted versus the mean energy deposited in strip 0 for all of the particles stopping in each strip. The red line is the best fit to these data, described by Eq. 6.1.

To determine the goodness of this fit, it is necessary to know how accurate the stopping strip predictions are. The plots in Fig. 6.9 show the stopping strip distributions that are

determined from the data and those predicted by LISE++ based on the energy deposited in strip zero. The distributions are fairly similar and some of the discrepancies can be attributed to the spatial resolution of the actual stopping point in the detector.

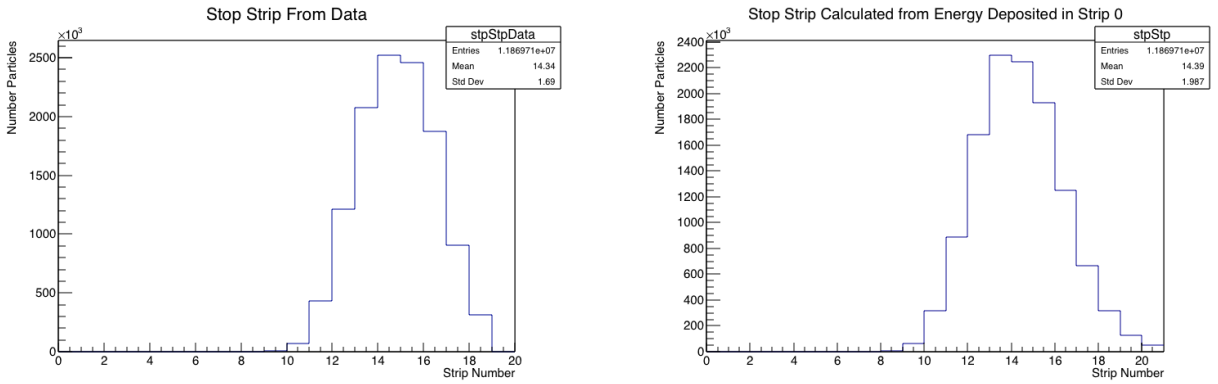

(a) (b)

Figure 6.9. A Comparison of the distribution of stopping ranges for particles in the data (a) with the predicted stopping locations of the particles based on their energy deposit in strip 0 (b).

To compare event-by-event, Fig. 6.10a shows the predicted strip versus the actual stopping strip for each event. This is well centered on the $y = x - 0.5$ line, which is offset by 0.5 to center the line on the center of each bin, because the x-axis bins have a size of 1. Figure 6.10b shows the difference between the predicted strip and the actual strip. This distribution is nearly centered on zero (centroid = 0.015) and has a full-width-half-max of 1.72 strips. This indicates that the prediction is fairly good.

The energy loss of ^{16}C in methane gas has not been studied experimentally. Thus, to turn the range of an ion into its energy, the use of energy loss calculation software becomes necessary. The predicted range of each ion from Eq. 6.1 can be used to find the energy of that ion at some point in the detector. To get a relationship between range and energy, the LISE++ physical calculator was used to predict what the range of ^{16}C is for different energies in 400 Torr of methane. By fitting this relationship, the predicted range in the detector can be used to determine the energy at which a fusion event has occurred. For example, if a fusion has occurred in strip 4, but the beam particle would have a range of

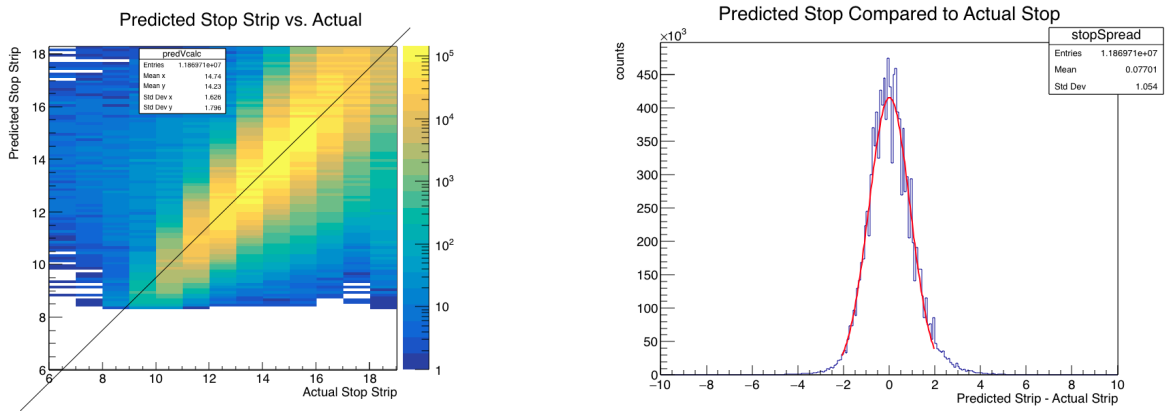

(a) (b)

Figure 6.10. Plot (a) shows the predicted stop strip versus the actual stop strip for all events in MUSIC. The $y = x - 0.5$ line is used to show the events whose range matches prediction. The subtracted 0.5 is half the width of a bin and is included to shift the line to the center of the bins for a more intuitive understanding of the data. Plot (b) is a histogram of the predicted strip minus the actual strip. The red line shows a gaussian fit to the data with a centroid at 0.015 and $\sigma = 0.90$.

13 strips had it not undergone fusion, then the length of 9 strips is the remaining range of the particle at the time of fusion and can be used to find the energy of the fusion. This is done using LISE++ to identify the particle energy associated with the particle's remaining range. This simultaneously removes the question of what incident energy the particle had and accounts for the spread in beam energy.

Figure 6.11 shows the energy of the ion on the y-axis and its predicted range plotted on the x-axis. Both axes are plotted in log scale. The data follow a fairly linear relationship above 10 MeV, suggesting that a fit in this energy range would be well described as $R \propto E^b$. Where R is the range in gas and E is the kinetic energy of the particle. However, corrections to this fit are needed to accurately describe the dependence of range on energy at low energies. In his textbook, (Ref. [46]) Leo describes the fit to a similar plot for range vs. energy loss of protons in aluminum. From an integration of the Bethe stopping power formula, we see that $R \propto E^2$ is the correct relationship in general; however, Leo's fit to the data is much better using $R \propto E^{1.75}$. For the current data, neither of these values for b produce a good fit, so that parameter is varied to find the best fit. There is also a constant parameter mentioned

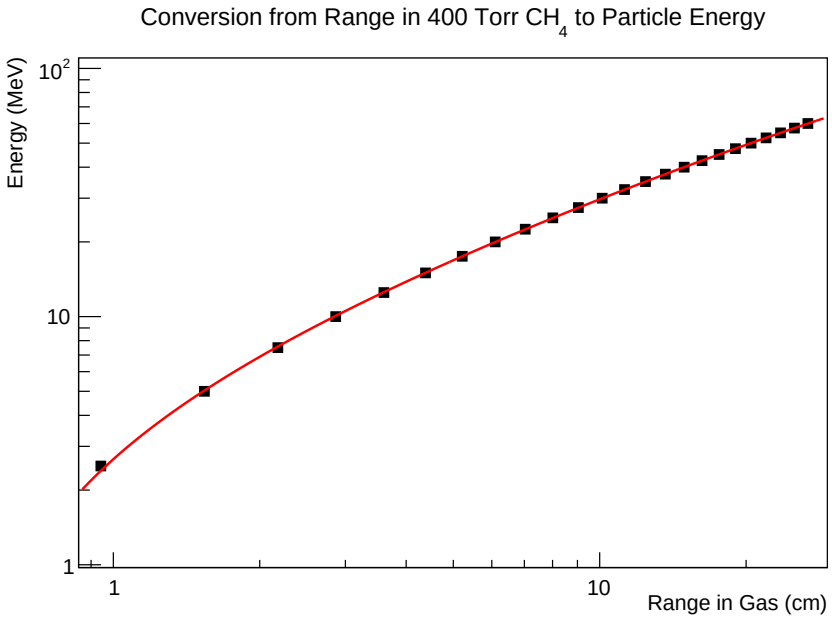

Figure 6.11. For a range of energies expected to be present in MUSIC, the energy is plotted versus the predicted range in the gas given by LISE++.

in Leo that needs to be included to account for low energy behavior. The fit to this system significantly improves at low energy when a linear term is included in the energy fit as well. Thus, the fit to Fig. 6.11 that is best for this curve is given by

$$E = 10.4 \times R^{0.867} - 3.41 - 4.38 \times R, \tag{6.2}$$

where R is the range in gas, in cm, and E is given in units of MeV.

Using the predicted range of each particle to determine its energy also gives a more specific prediction of the size of the fusion signal. A particle that has a short range will have a smaller fusion signal size, while the opposite is the case for a particle with long range for fusion in the same strip. A similar analysis to the one described in this dissertation has been performed using particle range to determine the expected fusion signal size and to bin the events for the calculation of the cross section. These results have been promising, but require a more rigorous treatment of efficiencies that has not yet been performed. This could be implemented in future work with this data, but is outside the scope of this thesis.

6.3. Suggestions for Future Experiments

This work can naturally be extended to study other carbon-carbon fusion systems using the same facility and detector. To our knowledge, no odd-odd carbon fusion systems have been measured to this day. With the RAISOR beam line upgrade at Argonne National Laboratory, the capability to produce an intense ^{15}C beam has improved greatly since the study by Carnelli *et al.* (2015). It would therefore not require much experimental time to make a measurement of the ^{15}C + ^{13}C fusion cross section with MUSIC. In the beam composition spectrum from this experiment, shown in Fig. 4.4, some ^{17}C was visible. Optimizing for a ^{17}C beam and performing a similar experiment would be one step closer toward measuring the most neutron-rich carbon fusion systems.

The half-life of radioactive ^{14}C is 5700 years. If an enriched sample of $^{14}CH_4$ could be obtained and sealed off in a designated MUSIC detector, it would offer a new combination of systems to study including ^{15,16,17}C + ^{14}C. This would require some re-engineering of MUSIC to obtain an excellent vacuum seal so that air does not seep in and cause contamination of the gas.

In this work, we have measured the total fusion cross sections of the most neutron-rich carbon fusion systems to date. These results are consistent with expectations that pairing effects in ^{16}C will lower the fusion cross section compared with ^{15}C, which has one weakly bound neutron in the sd-shell. The measured ^{16}C + ^{12}C and ^{16}C + ^{13}C agree well with theory, within systematic uncertainty. Efforts to reduce this systematic uncertainty in order to put tighter constraints on theory have been suggested, but require the development of new, detailed simulations that are out of the scope of this work.

Bibliography

[1] E. M. Burbidge, G. R. Burbidge, William A. Fowler, and F. Hoyle. Synthesis of the elements in stars. *Rev. of Mod. Phys.*, 29:547, 1957.

[2] H Palme, K Lodders, and A Jones. Solar system abundances of the elements. *Planets, Asteriods, Comets and The Solar System, Volume 2 of Treatise on Geochemistry (Second Edition). Edited by Andrew M. Davis. Elsevier, 2014., p. 15-36*, 2, 2014.

[3] Benjamin P Abbott, Rich Abbott, TD Abbott, Fausto Acernese, Kendall Ackley, Carl Adams, Thomas Adams, Paolo Addesso, RX Adhikari, VB Adya, et al. Gw170817: observation of gravitational waves from a binary neutron star inspiral. *Physical Review Letters*, 119(16):161101, 2017.

[4] MR Drout, AL Piro, BJ Shappee, CD Kilpatrick, JD Simon, C Contreras, DA Coulter, RJ Foley, MR Siebert, N Morrell, et al. Light curves of the neutron star merger gw170817/sss17a: Implications for r-process nucleosynthesis. *Science*, 358(6370):1570–1574, 2017.

[5] Daniel Kasen, Brian Metzger, Jennifer Barnes, Eliot Quataert, and Enrico Ramirez-Ruiz. Origin of the heavy elements in binary neutron-star mergers from a gravitational-wave event. *Nature*, 551(7678):80, 2017.

[6] Zach Meisel, Alex Deibel, Laurens Keek, Peter Shternin, and Justin Elfritz. Nuclear physics of the outer layers of accreting neutron stars. *Journal of Physics G: Nuclear and Particle Physics*, 45(9):093001, jul 2018.

[7] Jim J Kolata, Amy Roberts, AM Howard, Dan Shapira, J Felix Liang, Carl J Gross, RL Varner, Z Kohley, Anthony N Villano, H Amro, et al. Fusion of 124, 132 sn with 40, 48 ca. *Physical Review C*, 85(5):054603, 2012.

[8] Sunil Kalkal, S Mandal, N Madhavan, E Prasad, Shashi Verma, A Jhingan, Rohit Sandal, S Nath, J Gehlot, BR Behera, et al. Channel coupling effects on the fusion excitation functions for si 28+ zr 90, 94 in sub-and near-barrier regions. *Physical Review C*, 81(4):044610, 2010.

[9] M. Alcorta, K. E. Rehm, B. B. Back, S. Bedoor, P. F. Bertone, C. M. Deibel, B. DiGiovine, H. Esbensen, J. P. Greene, C. R. Hoffman, C. L. Jiang, J. C. Lighthall, S. T. Marley, R. C. Pardo, M. Paul, A. M. Rogers, C. Ugalde, and A. H. Wuosmaa. Fusion reactions with the one-neutron halo nucleus ^{15}C. *Phys. Rev. Lett.*, 106:172701, Apr 2011.

[10] Patricio Francisco Florencio Carnelli, S Almaraz-Calderon, KE Rehm, M Albers, M Alcorta, PF Bertone, B Digiovine, H Esbensen, J Fernández Niello, D Henderson, et al. Multi-sampling ionization chamber (music) for measurements of fusion reactions with radioactive beams. *Nuclear Instruments and Methods in Physics Research Section A: Accelerators, Spectrometers, Detectors and Associated Equipment*, 799:197–202, 2015.

[11] Juhan Frank, Andrew King, and Derek Raine. *Accretion power in astrophysics*. Cambridge university press, 2002.

[12] P. Marenfeld. Accretion disk (image 1). `https://www.nsf.gov/news/mmg/mmg_disp.jsp?med_id=66143`. Accessed: 2019-09-30.

[13] Anuj Parikh, Jordi José, Fermin Moreno, and Christian Iliadis. The effects of variations in nuclear processes on type i x-ray burst nucleosynthesis. *The Astrophysical Journal Supplement Series*, 178(1):110, 2008.

[14] RH Cyburt, AM Amthor, A Heger, E Johnson, L Keek, Z Meisel, H Schatz, and K Smith. Dependence of x-ray burst models on nuclear reaction rates. *The Astrophysical Journal*, 830(2):55, 2016.

[15] Hendrik Schatz, A Aprahamian, V Barnard, L Bildsten, A Cumming, M Ouellette, T Rauscher, F-K Thielemann, and M Wiescher. End point of the rp process on accreting neutron stars. *Physical Review Letters*, 86(16):3471, 2001.

[16] L Keek, E Kuulkers, A Cumming, EF Brown, M Suzuki, et al. First superburst from a classical low-mass x-ray binary transient. *Astronomy & Astrophysics*, 479(1):177–188, 2008.

[17] Sanjib Gupta, Edward F Brown, Hendrik Schatz, Peter Möller, and Karl-Ludwig Kratz. Heating in the accreted neutron star ocean: implications for superburst ignition. *The Astrophysical Journal*, 662(2):1188, 2007.

[18] M Beard, AV Afanasjev, LC Chamon, LR Gasques, M Wiescher, and DG Yakovlev. Astrophysical s factors for fusion reactions involving c, o, ne, and mg isotopes. *Atomic data and nuclear data tables*, 96(5):541–566, 2010.

[19] Samuel S. M. Wong. *Introductory Nuclear Physics - 2nd Edition*. John Wiley & Sons, Inc., New York, NY, 1998.

[20] Stephen G Steadman and Mark J Rhoades-Brown. Sub-barrier fusion reactions. *Annual Review of Nuclear and Particle Science*, 36(1):649–681, 1986.

[21] BB Back, H Esbensen, CL Jiang, and KE Rehm. Recent developments in heavy-ion fusion reactions. *Reviews of Modern Physics*, 86(1):317, 2014.

[22] Xiao Li Lu, Bao Yuan Sun, and Wen Hui Long. Description of carbon isotopes within relativistic hartree-fock-bogoliubov theory. *Phys. Rev. C*, 87:034311, Mar 2013.

[23] N. Imai, H. J. Ong, N. Aoi, H. Sakurai, K. Demichi, H. Kawasaki, H. Baba, Zs. Dombrádi, Z. Elekes, N. Fukuda, Zs. Fülöp, A. Gelberg, T. Gomi, H. Hasegawa, K. Ishikawa, H. Iwasaki, E. Kaneko, S. Kanno, T. Kishida, Y. Kondo, T. Kubo, K. Kurita, S. Michimasa, T. Minemura, M. Miura, T. Motobayashi, T. Nakamura, M. No-

tani, T. K. Onishi, A. Saito, S. Shimoura, T. Sugimoto, M. K. Suzuki, E. Takeshita, S. Takeuchi, M. Tamaki, K. Yamada, K. Yoneda, H. Watanabe, and M. Ishihara. Anomalously hindered $e2$ strength $b(e2; 2_1^+ \rightarrow 0^+)$ in ^{16}C. *Phys. Rev. Lett.*, 92:062501, Feb 2004.

[24] A. H. Wuosmaa, B. B. Back, S. Baker, B. A. Brown, C. M. Deibel, P. Fallon, C. R. Hoffman, B. P. Kay, H. Y. Lee, J. C. Lighthall, A. O. Macchiavelli, S. T. Marley, R. C. Pardo, K. E. Rehm, J. P. Schiffer, D. V. Shetty, and M. Wiedeking. $^{15}\mathbf{C}(d,p)^{16}\mathbf{C}$ reaction and exotic behavior in $^{16}\mathbf{C}$. *Phys. Rev. Lett.*, 105:132501, Sep 2010.

[25] A. Ozawa, T. Suzuki, and I. Tanihata. Nuclear size and related topics. *Nuclear Physics A*, 693(1):32 – 62, 2001. Radioactive Nuclear Beams.

[26] Suhel Ahmad, A. A. Usmani, and Z. A. Khan. Matter radii of light proton-rich and neutron-rich nuclear isotopes. *Phys. Rev. C*, 96:064602, Dec 2017.

[27] Claus E Rolfs, William S Rodney, and William S Rodney. *Cauldrons in the cosmos: Nuclear astrophysics*. University of Chicago press, 1988.

[28] LR Gasques, AV Afanasjev, M Beard, J Lubian, T Neff, M Wiescher, and DG Yakovlev. Sao paulo potential as a tool for calculating s factors of fusion reactions in dense stellar matter. *Physical Review C*, 76(4):045802, 2007.

[29] Vinay Singh, Debasis Atta, Md A Khan, and DN Basu. Astrophysical s-factor for deep sub-barrier fusion reactions of light nuclei. *Nuclear Physics A*, 986:98–106, 2019.

[30] DG Kovar, DF Geesaman, TH Braid, Y Eisen, W Henning, TR Ophel, M Paul, KE Rehm, SJ Sanders, P Sperr, et al. Systematics of carbon-and oxygen-induced fusion on nuclei with $12 \leq$ a ≤ 19. *Physical Review C*, 20(4):1305, 1979.

[31] H Esbensen, X Tang, and CL Jiang. Effects of mutual excitations in the fusion of carbon isotopes. *Physical Review C*, 84(6):064613, 2011.

[32] DG Yakovlev, M Beard, LR Gasques, and M Wiescher. Simple analytic model for astrophysical s factors. *Physical Review C*, 82(4):044609, 2010.

[33] B Harss, RC Pardo, KE Rehm, F Borasi, JP Greene, RVF Janssens, CL Jiang, J Nolen, M Paul, JP Schiffer, et al. Production of radioactive ion beams using the in-flight technique. *Review of Scientific Instruments*, 71(2):380–387, 2000.

[34] Physics Division Argonne National Laboratory. Atlas beam-line layout including airis.

[35] Physics Division Argonne National Laboratory. Airis design parameters.

[36] O.B. Tarasov and D. Bazin. Lise++: Radioactive beam production with in-flight separators. *NIM B*, 266:4657–4664, 2008.

[37] Harald A Enge. Magnetic spectrographs for nuclear reaction studies. *Nuclear Instruments and Methods*, 162(1-3):161–180, 1979.

[38] KE Rehm and FLH Wolfs. A focal plane detector for reactions with medium weight projectiles. *Nuclear Instruments and Methods in Physics Research Section A: Accelerators, Spectrometers, Detectors and Associated Equipment*, 273(1):262–272, 1988.

[39] Harald A Enge. Magnetic spectrographs for nuclear reaction studies. *Nuclear Instruments and Methods*, 162(1-3):161–180, 1979.

[40] Catherine M. Deibel. *The ^{26m}Al(p,gamma)^{27}Si Reaction Rate in ONe Novae.* PhD thesis, Yale University, 2008.

[41] James F Ziegler, Matthias D Ziegler, and Jochen P Biersack. Srim–the stopping and range of ions in matter (2010). *Nuclear Instruments and Methods in Physics Research Section B: Beam Interactions with Materials and Atoms*, 268(11-12):1818–1823, 2010.

[42] Patricio Carnelli. *Medición de secciones eficaces de fusión entre isótopos de carbono utilizando un blanco activo.* PhD thesis, Universidad Nacional de General San Martín, 2014.

[43] A. Gavron. Statistical model calculations in heavy ion reactions. *Physical Review C*, 21(1):230–236, 1980.

[44] Daniel Santiago. Music simulator. `https://gitlab.phy.anl.gov/dasago/music-simulator`. Accessed: 2019-09-29.

[45] R. R. Johnson, T. Masterson, B. Bassalleck, W. Gyles, T. Marks, K. L. Erdman, A. W. Thomas, D. R. Gill, E. Rost, J. J. Kraushaar, J. Alster, C. Sabev, J. Arvieux, and M. Krell. Neutron radii determinations from the ratio of π^- elastic scattering from ^{12,13}C and ^{16,18}O. *Phys. Rev. Lett.*, 43:844–847, Sep 1979.

[46] W. R. Leo. *Techniques for Nuclear and Particle Physics Experiments*. Physics textbook. Springer-Verlag, New York, 1987.

Vita

Ashley Ann Disbrow Hood was born in Trenton, NJ and raised along the Delaware river in Ewing, NJ and Yardley, PA. In 2010, she graduated high school from The Pennington School in Pennington, NJ. She earned her Bachelor of Science degree in Physics, with a concentration in Astrophysics, from Carnegie Mellon University in Pittsburgh, PA in 2014. Ashley began graduate school at Louisiana State University in the Department of Physics and Astronomy in the fall of 2014, where she became intrigued by the nuclear astrophysics group. She was drawn to the group because of the opportunity to carry out an entire experiment from conception to final analysis, as well as the opportunity to travel. During her time working with this group, she has worked on various detector development projects, including the SECAR focal plane system, and conducted many experiments at various radioactive ion beam facilities around the country. She has been the PI of two experimental campaigns conducted at Florida State University, participated in experiments at the NSCL at Michigan State University, and participated in multiple experiments using the ATLAS facility at Argonne National Laboratory, including her dissertation experiment. Ashley will graduate with her Ph.D. in Physics from Louisiana State University in December 2019. She will be a post-doctoral research associate at the Texas A&M University Cyclotron Institute beginning in January 2020.